**Title**

Meiotic chromosome organization: structure and function of the chromosome axis

**Author**

Rosenberg, Scott

**Publication Date**

2017

UNIVERSITY OF CALIFORNIA, SAN DIEGO

# Meiotic chromosome organization: structure and function of the chromosome axis

A dissertation submitted in partial satisfaction of the
requirements for the degree Doctor of Philosophy

in

Chemistry

by

Scott Chan Rosenberg

Committee in charge:

Professor Kevin Corbett, Chair
Professor Judy Kim, Co-Chair
Professor Robert Continetti
Professor Arshad Desai
Professor Partho Ghosh
Professor Navtej Toor

2017

This Dissertation of Scott Rosenberg is approved, and it is acceptable in quality and form for publication on microfilm and electronically

Co-chair

Chair

University of California, San Diego

2017

# Dedication

This thesis is dedicated to my parents and sister.

# Table of Contents

# List of Figures

# List of Tables

# Acknowledgements

I would like to acknowledge the outstanding training and support I have received from my mentor Professor Kevin Corbett. Kevin was always an available and enthusiastic advisor, and set an excellent example of the hard work and dedication required to lead a successful research group. Graduate school can be a demanding and rigorous environment, but working alongside the members of the Corbett lab has made it an immensely enjoyable and rewarding experience. I am grateful for everything I have learned from Dr. Corbett, and his efforts in helping me develop as a scientist.

Chapter 0 (Introduction), in full, is a reprint of the material as it appears in The multifaceted roles of the HORMA domain in cellular signaling. J Cell Biol. 2015 Nov 23;211(4):745-55. doi: 10.1083/jcb.201509076. Review. PubMed PMID: 26598612; PubMed Central PMCID: PMC4657174. Rosenberg SC, Corbett KD. The dissertation author is the primary author for this paper.

Chapter1, in full, is a repreint of the material as it appears in The chromosome axis controls meiotic events through a hierarchical assembly of HORMA domain proteins. Dev Cell. 2014 Nov 24;31(4):487-502. doi: 10.1016/j.devcel.2014.09.013. Epub 2014 Nov 6. PubMed PMID: 25446517; PubMed Central PMCID: PMC4254552. Kim Y, Rosenberg SC, Kugel CL, Kostow N, Rog O, Davydov V, Su TY, Dernburg AF, Corbett KD. The dissertation author is the primary co-author for this paper.

# Vita

| | |
|---|---|
| 2011 | Bachelor of Science, University of California, Santa Cruz |
| 2017 | Doctor of Philosophy, University of California, San Diego |

# Publications

Ye Q., Kim DH, Dereli I., Rosenberg S.C., Hagemann G., Herzog F., Toth A., Cleveland D., Corbett K.D. (in press) The AAA+ ATPase TRIP13 remodels HORMA domains through N-terminal engagement and unfolding. *EMBO J.*

Rosenberg S.C., Corbett K.D. (2015) The multifaceted roles of the HORMA domain in cellular signaling. *J Cell Biol.* 211(4):745-55.

Ye Q., Rosenberg S.C., Moeller A., Speir J.A., Su T.Y., Corbett K.D. (2015) TRIP13 is a protein-remodeling AAA+ ATPase that catalyzes MAD2 conformation switching. *eLife* **4**:07367.

Kim Y.*, Rosenberg S.C.*, Kugel C.L., Kostow N., Rog O., Dernburg A.F., Corbett K.D. (2014) The chromosome axis controls meiotic events through a hierarchical assembly of HORMA domain proteins. *Developmental Cell* **31**(4):487-502. ***(*co-first author)***

# Abstract of the Dissertation

Structure and Function of the Chromosome Axis: Organizing Meiotic Chromosomes

by

Scott Chan Rosenberg

Doctor of Philosophy in Chemistry

University of California, San Diego, 2017

Professor Kevin Corbett, Chair
Professor Judy Kim, Co-Chair

Chromosome segregation during meiosis is a two-step process, where homologous chromosomes segregate in the first meiotic division, and sister chromosomes segregate away in the second, thereby reducing ploidy by half. Homolog segregation in the first meiotic division requires that cells utilize a unique homologous recombination pathway to generate specific physical linkages between homologs in the form of chiasmata. Meiotic recombination involves the introduction of double-stranded breaks (DSBs) to the DNA, which are resected and used in a homology search to identify and associate with the homolog. The mechanisms that ensure accurate chromosome segregation during meiosis are important for maintaining genome stability, and errors in these processes have been shown to lead to miscarriages and developmental diseases like down syndrome.

One of the key adaptations eukaryotic cells have evolved to enable this specialized homologous recombination pathway is a protein assembly called the chromosome axis. The chromosome axis, also known as the axial element (AE), is a highly conserved scaffold that assembles between sister chromosomes. The AE physically organizes the chromatin into a linear array of loops, and also provides a platform for recruitment of the recombination machinery and eventual assembly of the synaptonemal complex. Chromosome axis components are highly conserved in different organisms, and include cohesin complexes, meiotic HORMA domain proteins, and foundation axial element proteins. We find the four HORMA domain proteins from *C. elegans* organize into a hierarchical complex through binding of highly conserved motifs in their C-terminal tails. We show that the different levels of this hierarchy play distinct roles in regulating chromatin organization and the homologous recombination pathway. This work provides a foundation for understanding both initial recruitment and self-assembly of meiotic HORMADs throughout eukaryotes. We also find that the mammalian foundation AE proteins SYCP2 and SYCP3 self-assemble into higher order filaments, establishing a model for their roles in organizing meiotic chromosomes. Finally, we use next-generation sequencing to examine the organization of meiotic chromosomes in highly synchronized spermatocytes in two meiotic prophase stages, identifying both commonalities with somatic cells and distinct features of meiotic chromosome organization. Overall, this work advances our understanding of meiotic chromosome axis architecture and function across eukaryotes.

# Introduction: The multi-faceted roles of the HORMA domain in cellular signaling

## Summary

The HORMA domain is a multifunctional protein-protein interaction module found in diverse eukaryotic signaling pathways including the spindle assembly checkpoint, numerous DNA recombination/repair pathways, and the initiation of autophagy. In all of these pathways, HORMA domain proteins occupy key signaling junctures, and function through the controlled assembly and disassembly of signaling complexes using a stereotypical “safety belt” peptide interaction mechanism. A recent explosion of structural and functional work has shed new light on these proteins, illustrating how strikingly similar structural mechanisms give rise to radically different functional outcomes in each family of HORMA domain proteins.

The HORMA domain was first identified through sequence similarity between three functionally unrelated proteins in *S. cerevisiae*: Hop1, Rev7, and Mad2 (Aravind and Koonin 1998). Hop1 is a member of a conserved family of proteins termed HORMADs, which bind chromosomes in early meiosis and control many aspects of meiotic recombination and chromosome segregation (Vader and Musacchio, 2014; Muniyappa et al., 2014). The multifunctional Rev7 protein (also called Mad2B or Mad2L2; here we will use Rev7 throughout) is a subunit of the translesion DNA polymerase ζ (Makarova and Burgers, 2015; Sale, 2013), participates in mitotic cell-cycle control (Pfleger et al., 2001; Listovsky and Sale, 2013), and controls recombination pathway choice in DNA double-strand break repair (Boersma et al., 2015; Xu et al., 2015). Mad2 is an essential mediator of the spindle assembly checkpoint (SAC), and is the best-characterized HORMA domain protein both structurally and functionally (Mapelli and Musacchio, 2007; Luo and Yu, 2008). Another HORMA domain protein, p31$^{\mathrm{comet}}$

(also called MAD2L1BP), also participates in SAC signaling through its interactions with Mad2 and Pch2/TRIP13, a conserved regulator of HORMA domain proteins (Xia et al., 2004; Yang et al., 2007; Tipton et al., 2012; Eytan et al., 2014; Wang et al., 2014; Ye et al., 2015). Recently, two autophagy-signaling proteins, Atg13 and Atg101, were also shown to possess HORMA domains (Jao et al., 2013; Suzuki et al., 2015a; Hegedűs et al., 2014). In all of these different pathways, the role of the HORMA domain is highly conserved, acting as a signal-responsive adaptor mediating protein-protein interactions through a structurally unique mechanism. In this review, we will outline the general structure and interaction mechanisms of the HORMA domain, then discuss how these properties uniquely contribute to signaling in each family. Along the way, we will attempt to draw parallels between different HORMA domain protein families, using lessons from well-understood systems like Mad2 to inform our understanding of the others.

## 0.1 Conserved structural features of the HORMA domain

As of this writing, the Protein Data Bank (http://www.pdb.org) lists 28 NMR and x-ray crystal structures of HORMA domain proteins (**Table S0.1**) that together reveal both common structural features and family-specific variations within the HORMA domain (**Figure 0.1**). The ~200 amino acid HORMA domain consists of two functionally-distinct regions: the core, comprising the first ~150 amino acids, and the C-terminal “safety belt” region. The core (colored gray in **Figure 0.1, S0.1**) comprises three α-helices (αA, αB, and αC) packed against a three-stranded β-sheet (β4, β5, and β6), usually with an additional pair of β-strands (the β2-β3 hairpin) on the “back” of the α-helices (**Figure**

**S0.1**). The structure of the HORMA domain core is stabilized by a buried hydrogen bond network involving an arginine on αA and a glutamate on β4; these are the only two residues conserved among all HORMA domain proteins (**Figure S0.2**) (Aravind and Koonin, 1998). The C-terminal "safety belt" region (colored light blue in **Figure 0.1, S0.1**) can pack against the HORMA domain core in two very different conformations to produce so-called "open" or "closed" states. In the "open" state, the safety belt folds into two β-strands (β7 and β8) that extend one side of the core β-sheet. In the more commonly-observed "closed" state, the safety belt wraps entirely around the domain and forms two new β-strands (β8' and β8") against the opposite side of the HORMA domain core. This change enables a short peptide from a binding partner to interact with the HORMA domain core; the bound peptide is then embraced by the safety belt as it wraps around the domain (**Figure 0.1, S0.1**). Because of the topological linkage of the HORMA domain with its binding partner, complex assembly or disassembly likely requires either: (1) that the partner protein bind in the process of an open-to-closed conformational conversion of the HORMA domain, or (2) that the safety belt transiently disengage from the HORMA domain core to allow partner binding. Mad2 is the only HORMA domain protein known to convert between open and closed states, and Mad2 conformational conversion is intimately linked with partner protein binding and checkpoint signaling (see below). Rev7 and the meiotic HORMADs are known to bind partner proteins in a manner equivalent to Mad2, but have only been observed in the closed conformation, so the structural mechanisms behind complex assembly and disassembly in these proteins remains unknown.

Mad2, Rev7, and the meiotic HORMADs each bind multiple different partner proteins through the above-described mechanism. Mad2-binding proteins contain similar

"Mad2-interacting motifs" (MIMs) that fit a consensus sequence of: K/RψψxϕxxxP, where "K/R" is a lysine or arginine; "ψ" is an aliphatic residue, usually leucine, isoleucine, or methionine; φ is a hydrophobic residue (aliphatic or aromatic); and "P" is proline (**Figure S0.3A**) (Luo et al., 2002; Sironi et al., 2002; Hanafusa et al., 2010). The polar K/R side-chain usually forms hydrogen-bonds with safety belt residues, and the first two aliphatic side-chains are mostly buried by the safety belt as it wraps around the MIM sequence. The downstream aliphatic residue and the proline, whose location varies in different Mad2 binding partners, are usually observed with their side-chains buried in a hydrophobic cleft between αB and β6 (**Figure S0.3B**). Rev7 has a similar consensus binding sequence of xψψxPxxxpP, where the lower-case "p" represents a less well-conserved proline residue (**Figure S0.3C**). As in Mad2, the conserved aliphatic residues are buried by the safety belt, and both conserved proline side-chains pack between αB and β6 (**Figure S0.3D**). The meiotic HORMAD proteins bind short "closure motifs" in their own disordered C-terminal tails to mediate self-assembly (Kim et al., 2014). The best-characterized HORMAD closure motifs are from *C. elegans* and possess a pair of conserved residues (tyrosine-glycine) that, like the aliphatic residues in Mad2/Rev7, are mostly buried by the safety belt wrapping over the closure motif **(Figure S0.3E-H**) (Kim et al., 2014). Closure motifs from mammalian HORMADs have also been identified (Kim et al., 2014), but comparing these sequences to those from *C. elegans* reveals no shared consensus sequence for closure motifs across different eukaryotic families.

Another common feature of the HORMA domain is dimerization, through a common interface involving helix αC and the β2-β3 hairpin (**Figure 0.2B-C, 0.5A**). Dimerization is usually observed between open and closed HORMA domains, and plays distinct roles in different HORMA domain families. In autophagy signaling, the formation of a dimer between Atg13 and Atg101 may simply mediate these proteins' association as part of an autophagy-initiation signaling complex (**Figure 0.5A**) (Suzuki et al., 2015a). In the spindle assembly checkpoint, however, the formation of Mad2:Mad2 homodimers and Mad2:p31(comet) heterodimers (**Figure 0.2B-C**) is critical for signaling, playing a key role in the conversion of Mad2 between its open and closed states (Mapelli and Musacchio, 2007; Luo and Yu, 2008). There are strong indications that Rev7 can dimerize in at least one of its functional contexts (Hara et al., 2009), though the exact role of dimerization in this family is unknown (see below). The only HORMA domain protein family lacking direct evidence for dimerization is the meiotic HORMADs.

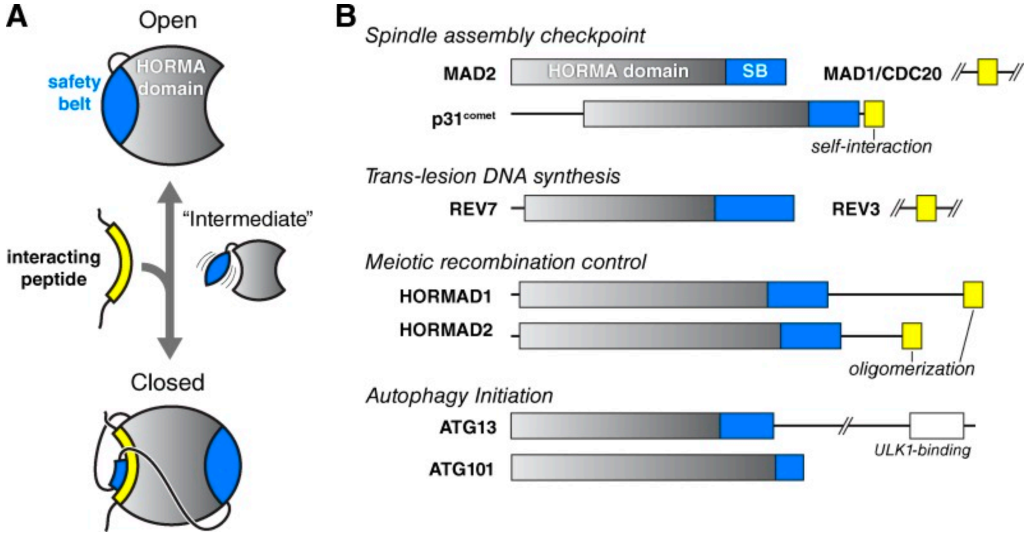

**Figure 0.1 Architecture and roles of HORMA domain proteins**

(A) Schematic illustrating how conformational changes in the HORMA domain safety belt (blue) are coupled to the binding of interacting peptides (yellow). In the open state, the safety belt occupies the peptide-interaction site. The hypothetical intermediate state would enable an interacting peptide to bind, and subsequently become locked into position once the safety belt binds the opposite side of the domain. Both the safety belt and the interacting peptide associate with the HORMA domain core through β-sheet interactions. (B) Domain diagram of human HORMA domain proteins. Proteins containing verified interacting peptides for each protein are shown in yellow. p31$^{comet}$ interacts *in cis* with its own C-terminal peptide, while the meiotic HORMADs' C-terminal "closure motifs" are thought to interact *in trans* to generate oligomeric assemblies. See **Figure S1** for structures and detailed secondary-structure diagrams of each family.

## 0.2 Mad2 and p31$^{comet}$ in the Spindle Assembly Checkpoint

To ensure accurate chromosome segregation in mitosis, eukaryotic cells monitor kinetochore-microtubule attachment through the spindle assembly checkpoint (SAC) (Musacchio and Salmon, 2007; Pines, 2011; Lara-Gonzalez et al., 2012; London and Biggins, 2014). In the SAC, unattached kinetochores catalyze the assembly of a soluble mitotic checkpoint complex (MCC) that inhibits an E3 ubiquitin ligase, the Anaphase-Promoting Complex/Cyclosome (APC/C). After all kinetochores become attached to microtubules, assembly of new MCC ceases and existing MCC is disassembled or degraded. The APC/C, directed by its co-activator Cdc20, then promotes the degradation of a defined set of cell-cycle proteins to mediate anaphase onset.

Mad2's functions in the SAC are intimately linked to the balance between the signaling-inactive open state and the active closed state, and the factors that promote conversion between these two states (**Figure 0.2**). In prometaphase, unattached kinetochores recruit Mad1, bound through a MIM to closed Mad2 (called C-Mad2) (Sironi et al., 2002). This Mad1:C-Mad2 complex is thought to stimulate the conversion of open Mad2 (O-Mad2) to the signaling-active closed state and its assembly into the MCC. This stimulation is accomplished by the recruitment of soluble O-Mad2 to the kinetochore-bound Mad1:C-Mad2 complex, to form a C-Mad2:O-Mad2 dimer (**Figure 0.2B, D**) (Shah et al., 2004; Howell et al., 2004; De Antoni et al., 2005; Mapelli et al., 2007). Dimerization subtly alters the structure of the O-Mad2 core and may lower the activation energy required to adopt a partially-unfolded "intermediate" (I-Mad2) state (Hara et al., 2015). I-Mad2 is thought to then bind a MIM in Cdc20 and re-fold into the C-Mad2 conformation (De Antoni et al., 2005). The resulting C-Mad2:Cdc20 complex then binds BubR1 and Bub3 to form the full MCC (Sudakin et al., 2001).

Once kinetochores are stably attached to microtubules, the Mad1:C-Mad2 complex is removed, halting assembly of new MCC (Howell et al., 2001; Lara-Gonzalez et al., 2012). The cell now faces a new problem: how to disassemble existing MCC to inactivate the SAC and allow anaphase onset? Recently, a mechanism for SAC inactivation through direct MCC disassembly has been described, involving p31$^{comet}$ and the AAA+ ATPase TRIP13. p31$^{comet}$ is a structurally-unique HORMA domain protein with a stable closed-like conformation (**Figure S0.1C**), and forms a heterodimer specifically with C-Mad2 (**Figure 0.2C**) (Yang et al., 2007; Habu et al., 2002; Mapelli et al., 2006). Disruption of p31$^{comet}$ in mammalian cells results in prolonged metaphase, supporting a role in SAC inactivation (Habu et al., 2002; Xia et al., 2004; Hagan et al., 2011), and experiments in cell extracts have suggested that p31$^{comet}$ functions by disassembling the MCC (Westhorpe et al., 2011; Reddy et al., 2007). Recently, p31$^{comet}$ was found to interact with TRIP13, a hexameric AAA+ ATPase related to a large family of protein complex remodelers/unfoldases (Ye et al., 2015; Tipton et al., 2012; Wang et al., 2014). The two proteins together were shown to directly disassemble the MCC in an ATP-dependent manner (Teichner et al., 2011; Eytan et al., 2014). Later work showed that TRIP13 directly converts C-Mad2 to O-Mad2, likely through transient unfolding of the Mad2 safety belt region (Ye et al., 2015). In the context of the MCC, conversion of Cdc20-bound C-Mad2 to the open state likely enables Cdc20 dissociation and MCC disassembly. It is important to note that MCC assembly and disassembly occur together throughout prometaphase, with disassembly dominating only after the SAC is satisfied (Kraft et al., 2003; Vink et al., 2006; Westhorpe et al., 2011). Whether and how MCC disassembly by p31$^{comet}$ and TRIP13 is regulated during the cell cycle is an important open question; recent findings in mammals and *Xenopus* suggest that this regulation may be achieved at least partially through phosphorylation of p31$^{comet}$ to modulate its affinity for Mad2 (Date et al., 2014; Mo et al., 2015).

While MCC disassembly is a key activity of p31$^{comet}$ and TRIP13, these proteins may have additional roles that are not yet well-understood. Recently, *C. elegans* p31$^{comet}$ (CMT-1) and TRIP13 (PCH-2) were found to be required for SAC activation when spindle assembly is disrupted (Nelson…Bhalla (2015) *JCB in press*). This paradoxical finding suggests that in some organisms, p31$^{comet}$ and TRIP13 may maintain the soluble pool of Mad2 in a state conducive to SAC activation. Finally, both p31$^{comet}$ and TRIP13 localize to unattached kinetochores in many organisms (Habu et al., 2002; Hagan et al., 2011; Tipton et al., 2012; Wang et al., 2014; Eytan et al., 2014) (Nelson…Bhalla (2015) *JCB in press*). This localization depends on Mad2, suggesting that p31$^{comet}$ directly recognizes kinetochore-bound Mad1:C-Mad2, but the roles of kinetochore-localized p31$^{comet}$ and TRIP13 remain largely mysterious.

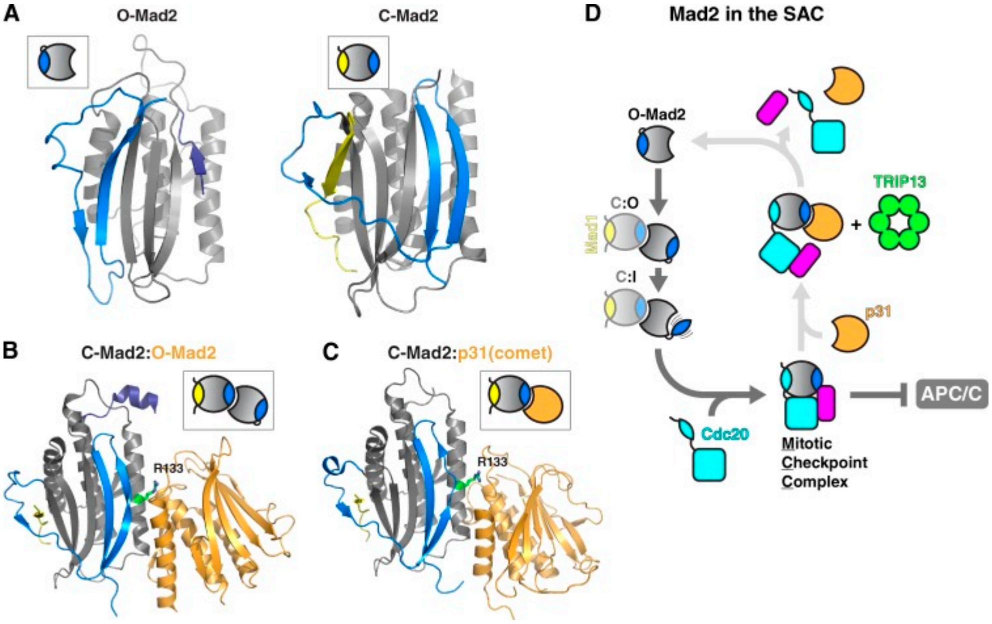

**Figure 0.2 Structure and function of Mad2 and p31(comet) in the spindle assembly checkpoint.**

(A) Structures of Mad2 in the unliganded open state (O-Mad2; right; from PDB ID 1DUJ (Luo et al., 2000)), and the Cdc20-bound closed state (C-Mad2; left; from PDB ID 4AEZ (Chao et al., 2012)), with structural elements colored as in **Figure 1**. (B) Structure of the *H. sapiens* C-MAD2:O-MAD2 dimer (PDB ID 2V64, (Mapelli et al., 2007)). C-MAD2 is colored as in **Figure 1**, and O-MAD2 is colored orange. Arginine 133 (R133), which is critical for dimerization (Sironi et al., 2001), is highlighted in green. (F) Structure of the *H. sapiens* MAD2:p31$^{comet}$ dimer (PDB ID 2QYF (Yang et al., 2007)). C-MAD2 is colored as in **Figure 1**, and p31$^{comet}$ is colored orange. (D) Spindle assembly checkpoint (SAC) activation by conversion of O-Mad2 to closed, Cdc20-bound Mad2 in the MCC. O-Mad2 is recruited to kinetochores by Mad1:Mad2, generating a C:O dimer. O-Mad2 is converted to the proposed intermediate state (I-Mad2) ,promoting Cdc20 binding and MCC assembly. Once the SAC signal has ceased, p31$^{comet}$ (orange) acts as an adaptor for TRIP13 (green)-mediated MCC disassembly, allowing APC/C activation. This mechanism of SAC inactivation is not conserved in budding yeast: *S. cerevisiae* lacks p31$^{comet}$, and its TRIP13 ortholog Pch2 functions only in the disassembly of HORMADs on meiotic chromosomes (see **Figure 3**).

## 0.3 Meiotic HORMADs: meiotic chromosome organization and recombination

In meiosis, cells must reduce their ploidy by half to generate gametes in preparation for sexual reproduction. Ploidy reduction requires that homologous chromosomes become physically linked by reciprocal DNA recombination events, called crossovers, in meiotic prophase. Crossover formation is controlled by a specialized structure called the chromosome axis, of which the meiotic HORMADs are a key component. In early meiotic prophase, meiotic HORMADs localize along the entire length of chromosomes, and promote DNA double-strand break (DSB) formation by the Spo11 endonuclease (Mao-Draayer et al., 1996; Woltering et al., 2000; Shin et al., 2010; Goodyer et al., 2008). After DNA breakage, meiotic HORMADs suppress recombination with the sister chromatid, thereby promoting recombination with the homolog to generate crossovers (**Figure 0.3**). This “homolog bias” of meiotic recombination stands in stark contrast to homologous recombination in mitotic cells, where repair via the sister is strongly favored (Humphryes and Hochwagen, 2014). Later in meiotic prophase, assembly of the specialized synaptonemal complex along each pair of homologs is, in most organisms, coordinated with the removal of meiotic HORMADs from chromosomes (Börner et al., 2008; Wojtasz et al., 2009; Lambing et al., 2015). Meiotic HORMAD removal is thought to shut down further DNA breakage by Spo11 and also alleviate the block to sister chromosome-mediated repair (**Figure 0.3**) (Kauppi et al., 2013; Thacker et al., 2014; Wojtasz et al., 2009). The complex signaling networks governing these activities, and the roles of meiotic HORMADs in these networks, have been nicely summarized in several recent reviews (MacQueen and Hochwagen, 2011; Subramanian and Hochwagen, 2014; Humphryes and Hochwagen, 2014).

Fungi have a single meiotic HORMAD (Hop1), while mammals and plants have two (HORMAD1/2 and ASY1/2), and the nematode *C. elegans* has four (HIM-3, HTP-1/2/3) (Hollingsworth and Johnson, 1993; Wojtasz et al., 2009; Caryl et al., 2000; Couteau and Zetka, 2005; Goodyer et al., 2008).While meiotic  HORMADs from fungi and plants contain additional domains that likely bind DNA or other proteins (Hollingsworth et al., 1990; Kironmai et al., 1998; Aravind and Iyer, 2002), most proteins in this family possess only an N-terminal HORMA domain and a disordered C-terminal tail (**Figure 0.1B, S0.1E**). Recent work with the expanded meiotic HORMAD family in *C. elegans* showed that these proteins contain “closure motifs” in their tails (one each in HIM-3, HTP-1, and HTP-2; and six in HTP-3), and form a hierarchical complex through specific HORMA domain-closure motif interactions (Kim et al., 2014) (**Figure 0.3**). These interactions are necessary for axis localization of HIM-3, HTP-1, and HTP-2, and as such are required for synaptonemal complex assembly and crossover formation (Kim et al., 2014). Further, this mode of interaction is conserved: mammalian HORMAD1 and HORMAD2 contain closure motifs in their C-termini that bind to the HORMA domain of HORMAD1 *in vitro* (Kim et al., 2014), and highly conserved motifs at the C-termini of both fungal and plant meiotic HORMADs (not shown) suggest that these proteins may also assemble in a similar manner.

Recent work has provided some insight into the mechanisms for initial recruitment of HORMADs to the chromosome axis. Mass spectrometry of meiotic HORMAD complexes in *C. elegans* suggests a direct interaction between HTP-3 and cohesin complexes; as HTP-3’s HORMA domain does not bind closure motifs in other meiotic HORMADs, it may bind a sequence within the cohesin complex to nucleate assembly on chromosomes (Kim et al., 2014). In other organisms, meiotic HORMAD recruitment requires a second chromosome axis component, which may in turn bind cohesin (Sakuno and Watanabe, 2015): *S. cerevisiae* Hop1 requires Red1 for chromosome localization (Smith and Roeder, 1997; Woltering et al., 2000), and similar dependencies on chromosome axis proteins – potentially orthologous to *S. cerevisiae* Red1 – have been reported for meiotic HORMADs from both plants and mammals (Fukuda et al., 2010; Ferdous et al., 2012; Wang et al., 2011). Thus, an attractive, though as yet unproven, model for meiotic HORMAD localization is that their HORMA domains bind closure motif sequences within cohesin or cohesin-binding axis proteins to mediate initial recruitment, followed by head-to-tail assembly of larger complexes on chromosomes (**Figure 0.3**). The extent of meiotic HORMAD self-association along chromosome axes *in vivo*, and crucially how the resulting assemblies promote and control meiotic DSB formation and inter-homolog recombination, are not yet well-understood.

As mentioned above, assembly of the synaptonemal complex is coordinated with the removal of meiotic HORMADs from chromosomes in many organisms. In a striking parallel with Mad2, meiotic HORMADs depend on TRIP13 (Pch2 in *S. cerevisiae*) for this removal. *S. cerevisiae* Pch2 was first identified as a protein that mediates the removal of Hop1 from chromosomes upon SC assembly, and both mammalian TRIP13 and plant PCH2 also share this function (San-Segundo and Roeder, 1999; Börner et al., 2008; Chen et al., 2014; Wojtasz et al., 2009; Lambing et al., 2015). The recent finding that mammalian TRIP13 can disassemble MAD2-containing complexes, likely through direct manipulation of the safety belt, strongly suggests that meiotic HORMAD removal from chromosomes involves a similar disassembly mechanism (Ye et al., 2015). While meiotic HORMADs have not been shown to possess a defined open state, transient unfolding of their safety belt region by TRIP13 would nonetheless disrupt closure motif binding and mediate complex disassembly and removal from the chromosome axis (**Figure 0.3**). How recognition of meiotic HORMADs by Pch2/TRIP13 is coordinated with SC assembly remains unknown: *S. cerevisiae* Pch2 directly interacts with Hop1 *in vitro* and can remove Hop1 from DNA (Chen et al., 2014), and *A. thaliana* PCH2 was recently shown to co-purify with the meiotic HORMAD ASY1 (Lambing et al., 2015). As TRIP13 recognition of Mad2 requires that it form a dimer with p31$^{comet}$ (Ye et al., 2015), it is intriguing to wonder whether meiotic HORMAD recognition requires either homo-dimerization or binding to an as-yet unidentified adapter protein.

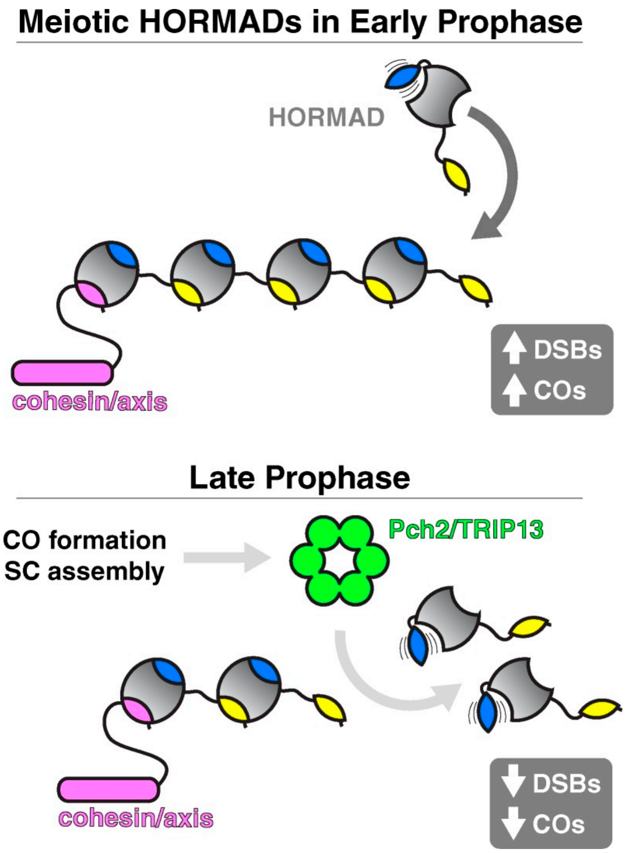

**Figure 0.3 Biological roles of the meiotic HORMADs**

Model for meiotic HORMAD assembly/disassembly at the meiotic chromosome axis. In early meiotic prophase (top), HORMADs are likely recruited to chromosomes through closure motifs in cohesin/SC proteins (pink), then self-assemble through HORMA-closure motif interactions. On chromosomes, HORMADs promote DSB and CO formation through largely-unknown mechanisms. Coinciding with the maturation of COs and SC assembly in late prophase (bottom), HORMADs are removed from the chromosomes in a TRIP13-dependent manner, down-regulating further DSB and CO formation.

## 0.4 Rev7: A polymerase adaptor with a secret life (or two)

All cells possess specialized pathways to synthesize DNA past damaged bases using a mechanism known as translesion synthesis (TLS). In eukaryotes, TLS involves the coordinated action of DNA polymerases that can insert bases opposite a lesion (“inserter” polymerase) and then continue synthesis past the lesion (“extender” polymerase) (Prakash et al., 2005; Waters et al., 2009; Sale, 2013). The major “extender” polymerase in eukaryotes is Pol ζ, which consists of the catalytic Rev3 subunit and the HORMA-domain protein Rev7 (Makarova and Burgers, 2015). Rev7 is required for full activity of Pol ζ (Nelson et al., 1996a) and links Pol ζ to Rev1, an “inserter” polymerase that also coordinates the activity of Pol ζ with other inserter polymerases (Nelson et al., 1996b; 2000; Haracska et al., 2001; Ross et al., 2005) (**Figure 0.4A**). Thus, Rev7 plays a central organizing role in TLS through its interactions with Rev3 and Rev1 (**Figure 0.4B**).

Human REV3 contains two REV7-binding motifs (#1: residues 1877-1898 and #2: 1993-2003 of 3130 in human REV3), suggesting that active Pol ζ might incorporate two copies of REV7 (Hara et al., 2009; 2010; Tomida et al., 2015). Interestingly, a reconstituted REV7:REV3$^{1848\text{-}1898}$ complex forms a heterotetramer in solution, and this tetramer is disrupted by mutation of REV7 arginine 124, located within the canonical HORMA domain dimerization interface on helix αC (Hara et al., 2009). As mutation of the equivalent residue in Mad2 (Arg133) disrupts Mad2 dimer formation (Sironi et al., 2001), this evidence supports the idea that Rev7 can form canonical HORMA domain dimers. Our own yeast two-hybrid analysis confirms that REV7 can self-associate, and that mutation of arginine 124 disrupts this association (not shown). Thus, an attractive model is that two copies of Rev7 might bind the two motifs in Rev3 and then homodimerize. This Rev7 homodimer could promote a productive conformation of Rev3, and/or also recruit additional proteins to coordinate TLS (Tomida et al., 2015).

Rev7 binds to the inserter polymerase Rev1 through a surface on its β-sheet face that includes β8' and β8", close to but not overlapping the putative Rev7 dimerization surface (**Figure 0.4A**) (Wojtaszek et al., 2012; Kikuchi et al., 2012). This interaction surface is unique among HORMA domain proteins, and because of its dependence on β8' and β8", likely requires the "closed" conformation of Rev7. Another potential binding partner is the transcription factor TFII-I, which is proposed to bind Rev7 and recruit Pol ζ to sites of damage through an interaction with PCNA (Fattah et al., 2014). *In vitro*, TFII-I can bind to a reconstituted Rev3:Rev7:Rev1 complex (Fattah et al., 2014), suggesting that the Rev7 HORMA domain may possess yet another unique protein interaction surface. Finally, one or more Rev7 interactions may be phospho-regulated: the multifunctional Dbf4-dependent protein kinase (DDK), which is required for TLS in yeast (Yamada et al., 2013), is proposed to phosphorylate Rev7 to promote Pol ζ localization to sites of repair (Brandão et al., 2014). Overall, while much work remains to tease out the details of its multiple interactions, it is clear that Rev7 is central to the assembly and function of TLS polymerases.

While early work on Rev7 revealed its highly conserved roles in the TLS pathway, mammalian REV7 also plays a supporting role in the control of cell division. Based on sequence similarity to MAD2, human REV7 was rediscovered in 1999 and named MAD2B/MAD2L2 (Cahill et al., 1999). Later work showed that REV7 inhibits the APC/C *in vitro* through a direct interaction with CDH1/FZR1, a paralog of CDC20 (Chen and Fang, 2001; Pfleger et al., 2001; Listovsky and Sale, 2013). CDH1 directs APC/C activity after CDC20-mediated anaphase onset, to promote mitotic exit and the transition to G1 (Primorac and Musacchio, 2013; Sivakumar and Gorbsky, 2015). REV7 binds and sequesters CDH1 during metaphase, and is targeted for degradation by APC/C-CDC20 in early anaphase, thereby releasing CDH1 (**Figure 0.4C**) (Listovsky and Sale, 2013). This mechanism complements other pathways for control of CDH1-APC/C interactions (reviewed in (Primorac and Musacchio, 2013)), and is required for the proper timing of mitotic exit (Listovsky and Sale, 2013). In an intriguing connection with Rev7's TLS functions, Rev1 is also a substrate for APC/C-Cdc20-mediated degradation at anaphase, and its ubiquitylation and degradation depends on the presence of Rev7 (Chun et al., 2013).

Recently Rev7 has been implicated in recombination pathway choice during DNA double-strand break repair. Eukaryotic cells can repair DNA double-strand breaks (DSBs) either by non-homologous end joining (NHEJ), which is highly error-prone, or by homologous recombination (HR). The choice of pathway is heavily influenced by cell-cycle stage, and the signaling networks controlling pathway choice have only recently become well-understood. A critical step determining which pathway is used for repair is the amount of 5'-to-3' resection that occurs at a break: the generation of a long 3' single-stranded overhang favors HR, while limited resection favors NHEJ. A cascade of factors is recruited to DNA break sites, including the proteins 53BP1 and Rif1, which together inhibit end resection to promote NHEJ. Recently, two separate screens for factors governing recombination pathway choice in very different contexts identified Rev7 as another inhibitor of DSB end resection (Xu et al., 2015; Boersma et al., 2015). Rev7 was shown to act downstream of 53BP1 and Rif1 to limit resection and promote NHEJ

(**Figure 0.4D**), but the mechanism for its recruitment to DSB sites, and how it ultimately inhibits end resection is currently unknown.

Finally, there are hints that Rev7 has even more roles than space here allows us to discuss, including epigenetic reprogramming of germ cells and maintenance of pluripotency (Pirouz et al., 2013; Watanabe et al., 2013; Sale, 2013; Pirouz et al., 2015), heterochromatin maintenance (Vermeulen et al., 2010), and additional roles in mitosis (Medendorp et al., 2009; 2010) and DNA damage signaling (Zhang et al., 2007). An important avenue for future inquiry will be to determine if these diverse roles of Rev7 are linked, perhaps by a shared cell-cycle dependence or as-yet unappreciated common regulation in developmental pathways.

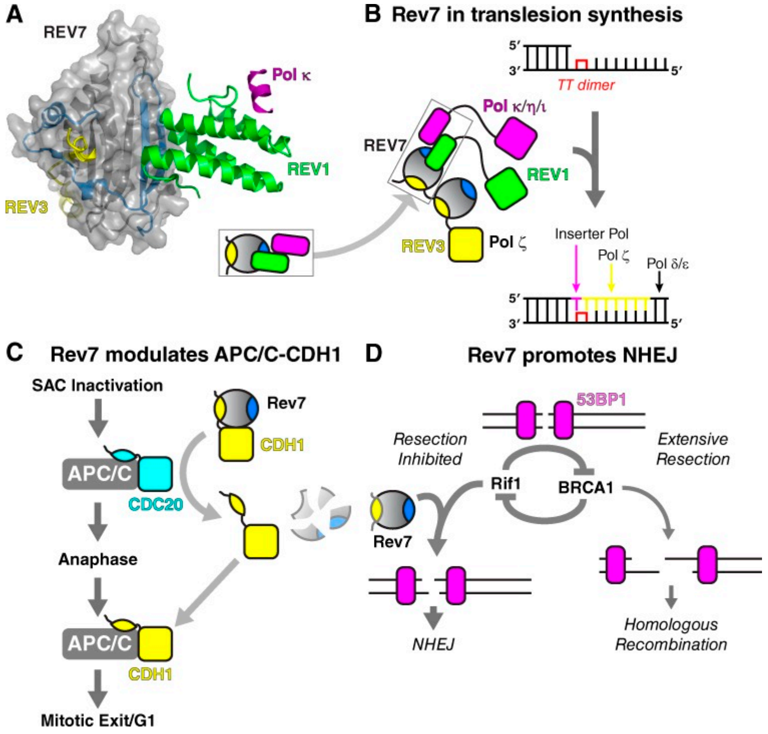

## Figure 0.4 Biological roles of Rev7

(A) Crystal structure of the complex between Rev7 (shown as gray "surface" representation), Rev3 (yellow), Rev1 (green), and the Rev1-interacting region of Pol κ (purple) (Wojtaszek et al., 2012; Xie et al., 2012). *Inset:* schematic version of this structure. (B) Diagram outlining the role of Rev7 and associated TLS polymerases during lesion bypass. Rev1 or an associated "inserter" polymerase inserts the first base opposite the thymine dimer, and Pol ζ performs the following extension step. (C) Proposed role of Rev7 as an inhibitor of APC/C-CDH1 during mitosis. Rev7 binds CDH1/FZR1, potentially through a HORMA domain-binding motif as in Mad2:Cdc20, sequestering it from the APC/C. Once APC/C-CDC20 is activated at anaphase onset, Rev7 is targeted for degradation, resulting in the release of CDH1 and its incorporation into the APC/C. (D) The role of Rev7 during DSB repair. After 53BP1 association with a DSB, Rif1 and BRCA play antagonistic roles to promote end resection and homologous recombination, or inhibition of resection leading to non-homologous end joining (NHEJ). Rev7 acts downstream of Rif1 through an unknown mechanism, to inhibit resection and promote NHEJ.

## 0.5 HORMA domain proteins in autophagy initiation

Autophagy (literally, “self-eating”) is a conserved starvation-response pathway in eukaryotic cells, in which part of a cell’s contents are engulfed and then degraded (Mizushima, 2007; Xie and Klionsky, 2007). The first step in autophagy is formation of the PAS (Pre-Autophagosomal Structure or Phagophore Assembly Site), which in *S. cerevisiae* is initiated by assembly of the Atg1 kinase complex (Mizushima, 2010). This complex is composed of three functional units: the Atg1 kinase, the Atg17/29/31 scaffold complex, and Atg13 (**Figure 0.5B**). Atg13 possesses an N-terminal HORMA domain (Jao et al. 2013) and an extended C-terminal tail with regulatory phosphorylation sites and binding sites for both Atg1 and the Atg17 scaffold complex (Stjepanovic et al., 2014; Fujioka et al., 2014). Autophagy initiation is regulated by Atg13 tail phosphorylation: in nutrient-rich conditions, the TOR kinase phosphorylates Atg13, inactivating it. In response to starvation, Atg13 is rapidly dephosphorylated, allowing the C-terminus to bind both Atg1 (Kabeya et al., 2005; Ragusa et al., 2012) and Atg17 (Kamada et al., 2000), thereby initiating PAS formation.

When the crystal structure of the N-terminal domain of budding-yeast Atg13 was determined in 2013, it revealed a previously-unidentified HORMA domain in a closed conformation but without a binding partner (**Figure S0.1F**) (Jao et al., 2013), immediately raising the question as to what this domain might bind. Recently it was found that the Atg13 HORMA domain is required for the recruitment of Atg9-containing vesicles, a critical step in development of the PAS (Suzuki et al., 2015b). This was further demonstrated to be mediated by a direct interaction between the Atg13 HORMA domain and the N-terminal disordered region of Atg9, strongly suggesting that the Atg13

HORMA domain binds a motif within Atg9 in a manner equivalent to other HORMA domain proteins (Suzuki et al., 2015b).

In contrast to the case in fission yeast and animals (see below), budding-yeast Atg13 has not been shown to form homo- or heterodimers. It has been suggested that a budding-yeast specific addition to the HORMA domain, termed the cap (**Figure S0.1F**), stabilizes the closed monomeric structure of Atg13 (Jao et al., 2013; Suzuki et al., 2015a). On the other hand, *S. cerevisiae* Atg13 promotes self-interaction and activation of the Atg1 kinase, suggesting that budding-yeast Atg13 may in fact self-associate (Yeh et al., 2011). Further work will be required to determine whether the putative self-interaction of Atg13 is mediated by the HORMA domain, either through homodimerization or HORMAD-style head-to-tail association.

Autophagy initiation in animals and the fission yeast *S. pombe* involve orthologs of Atg1 kinase (ULK1/2 in animals) and Atg13, while the Atg17 scaffold complex is functionally replaced by other proteins (Mizushima, 2010; Hurley and Schulman, 2014). These proteins include a second HORMA domain protein, Atg101, which folds into the open state and binds directly to Atg13, forming an open-closed heterodimer similar in structure to the open-closed Mad2 dimer (Hosokawa et al., 2009; Mercer et al., 2009; Michel et al., 2015; Suzuki et al., 2015a; Qi et al., 2015) (**Figure 0.5A**). The dimerization interface of Atg101 is highly conserved, and disruption of the interface results in severe autophagy defects *in vivo* (Suzuki et al., 2015a). The functional significance of Atg13:Atg101 dimerization, and whether this complex is dynamic as in Mad2, is not currently known. The Atg101 safety belt is truncated, containing a β7 strand but no β8 strand, making it unlikely that the protein can adopt the open state and supporting the idea that the Atg13:Atg101 dimer is stable/constitutive (Suzuki et al., 2015a; Qi et al., 2015; Michel et al., 2015). In addition to binding Atg13, Atg101 has several unique structural features that are important for autophagy signaling. In particular, an extended loop connecting β4 and β5 referred to as the "WF finger" motif because of the presence of conserved aromatic residues, is required for autophagy and is proposed to mediate protein-protein interactions important for autophagy initiation (Suzuki et al., 2015a). These interactions may compensate for a proposed loss of interaction potential within the HORMA domain of Atg13 in these species: a recent structure of human ATG13 showed that this protein's safety belt is shorter than that in budding or fission yeast, and may not be capable of binding peptide motifs (Qi et al., 2015). Overall, the roles of the HORMA domains of Atg13 and Atg101 in autophagy signaling are just beginning to be explored, and it will be exciting to see how the common themes of HORMA domain structure and function contribute to signaling in this pathway.

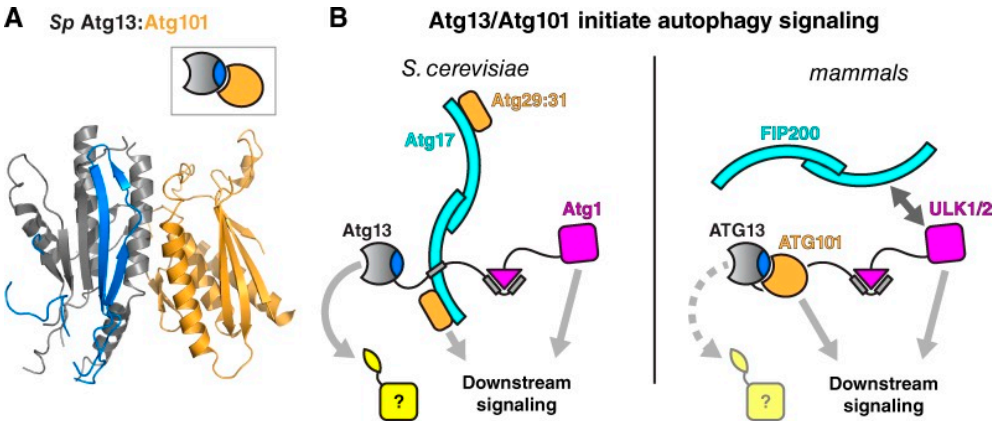

**Figure 0.5 Structure and function of Atg13 and Atg101**

(A) Structure of the *S. pombe* Atg13:Atg101 dimer (PDB ID 4YK8, (Suzuki et al., 2015a)). Closed-conformation Atg13 is colored as in **Figure 1,** and open-conformation Atg101 is colored orange. (B) Role of Atg13 and Atg101 in autophagy signaling. In *S. cerevisiae* (left), Atg13 acts as a scaffold for assembly of the Atg1 complex. The Atg13 HORMA domain likely binds a downstream component (yellow) to mediate autophagy initiation; the best candidate protein identified so far is Atg9 (Suzuki et al., 2015b). In mammals (right), ATG13 plays a similar scaffolding role, along with ATG101, but the ATG13 HORMA domain may not be capable of binding partners due to its shortened safety belt region (Qi et al., 2015).

## Conclusions

Recent years have seen great progress in defining the mechanisms of HORMA domain function in many different cellular contexts. While originally identified as a domain shared between three protein families (Hop1, Rev7, Mad2) (Aravind and Koonin 1998), three additional families with the same fold have since been defined (p31$^{comet}$, Atg13, Atg101). Despite the great functional diversity among these families, some common themes can be drawn from the work on HORMA domain proteins to date. With few exceptions, these proteins' mechanisms are based around two types of interactions: the binding of the safety belt region around short peptide motifs, and homo/heterodimerization. The assembly and disassembly of complexes using these interactions, and the functional interplay between protein interactions and conformational changes within the domain, accounts for many aspects of these proteins' functions. While each family has unique modifications and interaction modes that enable specialized functions, the core role of the HORMA domain remains remarkably constant.

There are many outstanding questions regarding the mechanisms of the known HORMA domain protein families. Chief among them, to us, is the mechanism for binding and exchange of partner proteins in those families that have not been shown to adopt an open state. Of 28 structures of HORMA domain proteins in the Protein Data Bank, 22 depict HORMA domains with their safety belts topologically embracing a binding partner; in the other six, there either is no partner bound, or the HORMA domain is in the open state. The consistent observation that partners are topologically linked to the closed HORMA domain strongly supports the idea that these interactions universally involve “opening” of the safety belt during binding or release, be this a transition to a state like Mad2’s open state, or simply a transient unfolding or disengagement of the safety belt from the core. The question of whether and how HORMA domain proteins “open” has important implications for these proteins’ mechanisms, especially when considering the dynamics of HORMA domain protein complexes during signaling pathway activation and inactivation. Overall, understanding the dynamics and mechanisms of partner protein binding, exchange, and release by each family of HORMA domain proteins will be an important avenue of future research.

Could there be additional HORMA domain proteins waiting to be identified? Our own structure-based searches of several representative genomes reveal no additional examples, but as the saying goes: “The absence of evidence is not evidence of absence.” Given the functional plasticity of the HORMA domain and its consequent central roles in many different pathways, it would not be surprising to find this domain at key signaling junctures in even more pathways in the future.

# Supplemental Data

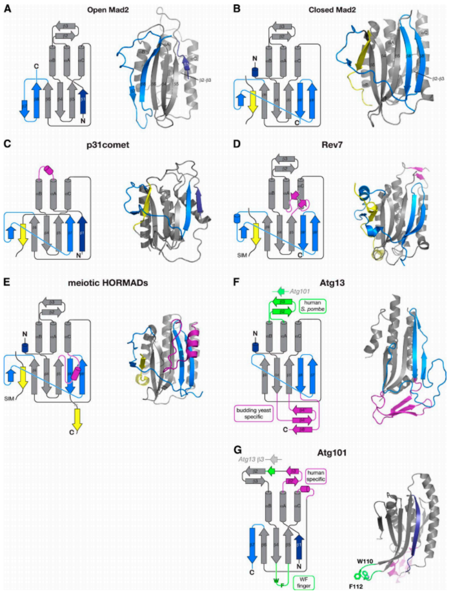

**Figure S0.1 HORMA domain protein structure**

(A) Secondary structure (left) and NMR structure (right; from PDB ID 1DUJ (Luo et al., 2000) of H. sapiens open MAD2 (O-MAD2). The HORMAD domain core is shown in gray, safety belt in light blue, and bound peptide in yellow. (B) Secondary structure (left) and x-ray crystal structure (right; from PDB ID 4AEZ; Chao et al., 2012) of S. pombe closed Mad2 (C-Mad2) bound to the Cdc20 peptide sequence. (C) Secondary structure diagram and crystal structure of H. sapiens p31comet (PDB ID 2QYF; Yang et al., 2007). (D) Secondary structure diagram (left) and crystal structure (right) of Mus musculus REV7 (PDB ID 4FJO; Wojtaszek et al., 2012). Unique β-sheet interaction between the N terminus and β5-αC loop is highlighted in purple. (E) Generic secondary structure diagram of meiotic HORMADs (left) and crystal structure of C. elegans HIM-3 (right; PDB ID 4TRJ; Kim et al., 2014), with unique loop structure between β5-αC loop highlighted in purple. (F) Secondary structure diagram of Atg13 (left), with S. pombe–specific features highlighted in green and Lachancea thermotolerans–specific features highlighted in purple. Crystal structure of L. thermotolerans Atg13 (PDB ID 4J2G; Jao et al., 2013) shown on the right, highlighting the cap structure in purple, which is unique to organisms that do not contain Atg101, implying it may be involved in stabilizing the Atg13 HORMA domain the absence of Atg101. (G) Secondary structure diagram (left) of Atg101, with structural features unique to humans highlighted in purple. The crystal structure of H. sapiens Atg13 is shown on the right, highlighting the WF finger motif identified by the authors (PDB ID 4WZG; Michel et al., 2015).

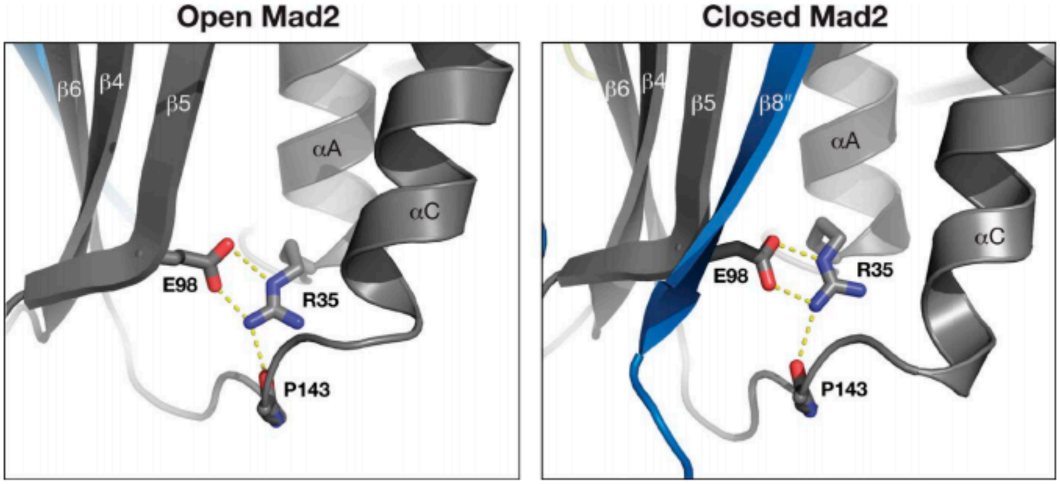

**Figure S0.2 A conserved hydrogen-bonding network stabilizes the HORMA domain core.**

Hydrogen bonding network of Mad2 arginine 35 (R35) and glutamate 98 (E98) in open (left) and closed (right) conformations. The view is similar to that in Fig. S1, A and B. In all HORMA domain structures determined to date, these two residues form a buried salt-bridge interaction. In most examples, the arginine residue also forms a hydrogen bond with the linker connecting αC to β6; in the case of Mad2, this hydrogen bond is to the main-chain carbonyl of proline 143 (P143).

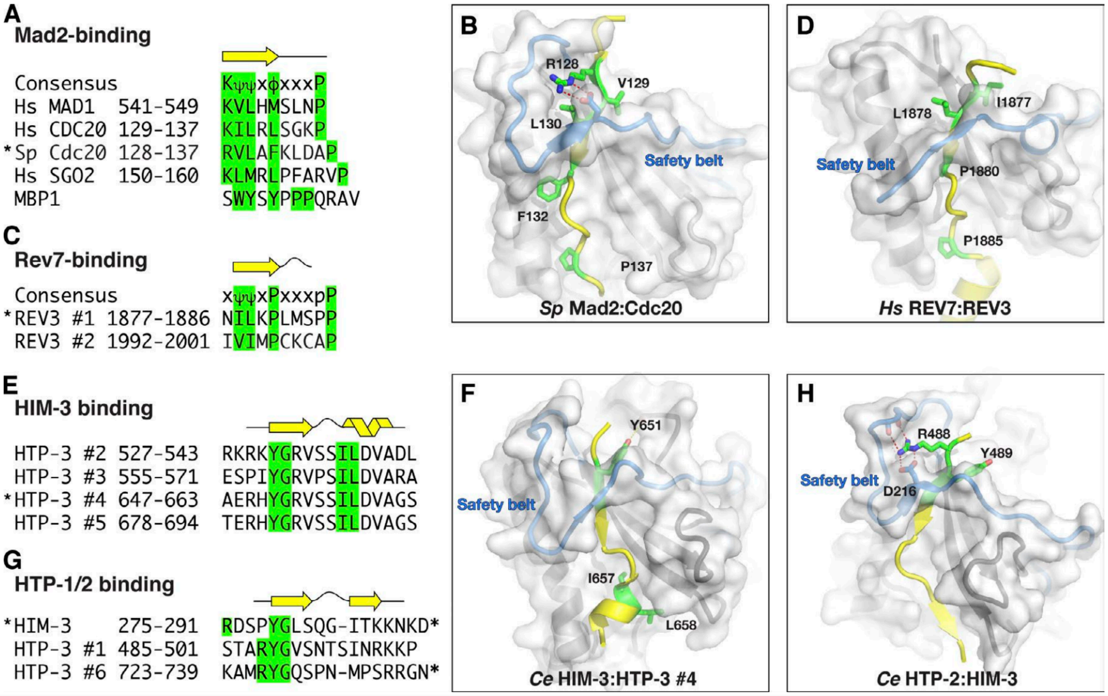

**Figure S0.2 Peptide binding specificity in Mad2, Rev7, and the meiotic HORMADs.**

(A) Sequences known to bind Mad2. Residues important for binding are highlighted in green. The biological function of the H. sapiens SGO2-MAD2 interaction is not well understood, but it may play a role in sister cohesion in meiosis I (Orth et al., 2011). (B) Structure of the S. pombe Mad2–Cdc20 interaction (from PDB ID 4AEZ; Chao et al., 2012), with MIM consensus residues shown as sticks and colored green. (C) Sequences known to bind Rev7. (D) Structure of the H. sapiens REV7–REV3 motif 1 interaction (PDB ID 3ABD; Hara et al., 2010), with consensus-sequence residues shown as sticks and colored green. Also shown is the short α-helix following the Rev7-binding motif, which was found to contribute to binding (Hanafusa et al., 2010). (E) Sequence alignment of HIM-3 binding closure motifs in HTP-3. Canonical residues that are buried in the interior of HIM-3 are highlighted in green. (F) Crystal structure of HTP-3 (648–663) peptide, bound by HIM-3 HORMA domain (PDB ID 4TZJ; Kim et al., 2014). (G) Sequence alignment of HTP-1/2 binding closure motifs in HIM-3 and HTP-3. (H) Crystal structure of C. elegans HTP-2 bound to the HIM-3 closure motif (PDB ID 4TZL; Kim et al., 2014).

## Table S0.1: Structures of HORMA domain proteins in the Protein Data Bank

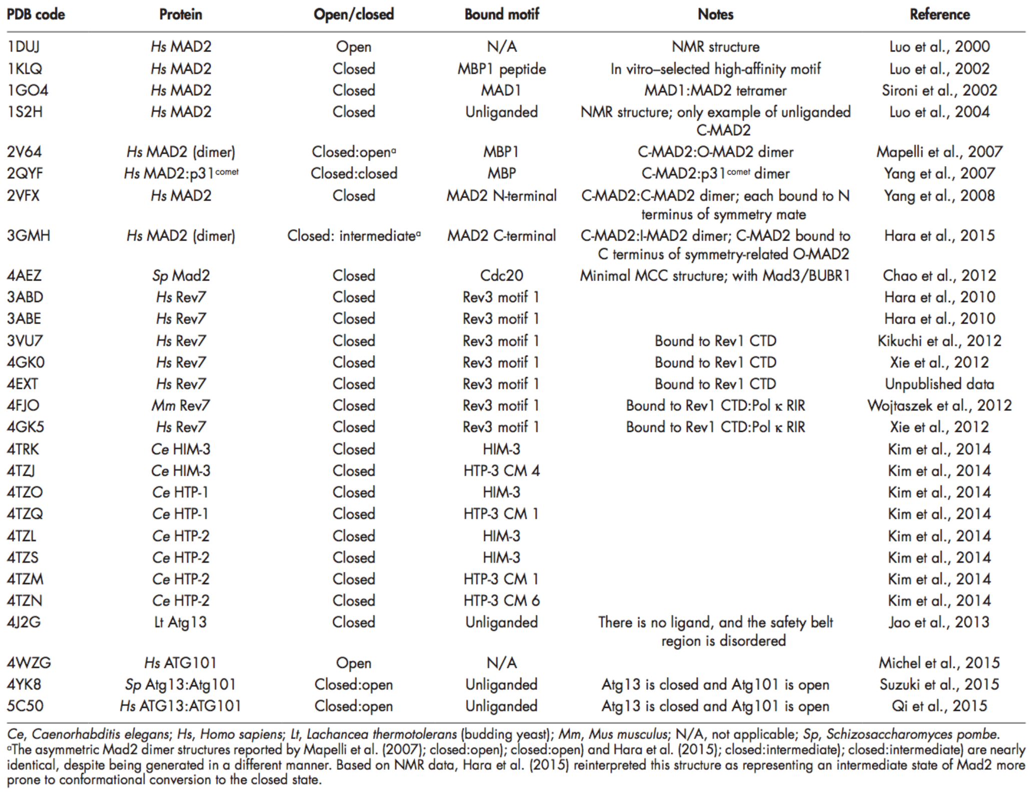

| PDB code | Protein | Open/closed | Bound motif | Notes | Reference |
|---|---|---|---|---|---|
| 1DUJ | *Hs* MAD2 | Open | N/A | NMR structure | Luo et al., 2000 |
| 1KLQ | *Hs* MAD2 | Closed | MBP1 peptide | In vitro–selected high-affinity motif | Luo et al., 2002 |
| 1GO4 | *Hs* MAD2 | Closed | MAD1 | MAD1:MAD2 tetramer | Sironi et al., 2002 |
| 1S2H | *Hs* MAD2 | Closed | Unliganded | NMR structure; only example of unliganded C-MAD2 | Luo et al., 2004 |
| 2V64 | *Hs* MAD2 (dimer) | Closed:open[a] | MBP1 | C-MAD2:O-MAD2 dimer | Mapelli et al., 2007 |
| 2QYF | *Hs* MAD2:p31$^{\text{comet}}$ | Closed:closed | MBP | C-MAD2:p31$^{\text{comet}}$ dimer | Yang et al., 2007 |
| 2VFX | *Hs* MAD2 | Closed | MAD2 N-terminal | C-MAD2:C-MAD2 dimer; each bound to N terminus of symmetry mate | Yang et al., 2008 |
| 3GMH | *Hs* MAD2 (dimer) | Closed: intermediate[a] | MAD2 C-terminal | C-MAD2:I-MAD2 dimer; C-MAD2 bound to C terminus of symmetry-related O-MAD2 | Hara et al., 2015 |
| 4AEZ | *Sp* Mad2 | Closed | Cdc20 | Minimal MCC structure; with Mad3/BUBR1 | Chao et al., 2012 |
| 3ABD | *Hs* Rev7 | Closed | Rev3 motif 1 |  | Hara et al., 2010 |
| 3ABE | *Hs* Rev7 | Closed | Rev3 motif 1 |  | Hara et al., 2010 |
| 3VU7 | *Hs* Rev7 | Closed | Rev3 motif 1 | Bound to Rev1 CTD | Kikuchi et al., 2012 |
| 4GK0 | *Hs* Rev7 | Closed | Rev3 motif 1 | Bound to Rev1 CTD | Xie et al., 2012 |
| 4EXT | *Hs* Rev7 | Closed | Rev3 motif 1 | Bound to Rev1 CTD | Unpublished data |
| 4FJO | *Mm* Rev7 | Closed | Rev3 motif 1 | Bound to Rev1 CTD:Pol κ RIR | Wojtaszek et al., 2012 |
| 4GK5 | *Hs* Rev7 | Closed | Rev3 motif 1 | Bound to Rev1 CTD:Pol κ RIR | Xie et al., 2012 |
| 4TRK | *Ce* HIM-3 | Closed | HIM-3 |  | Kim et al., 2014 |
| 4TZJ | *Ce* HIM-3 | Closed | HTP-3 CM 4 |  | Kim et al., 2014 |
| 4TZO | *Ce* HTP-1 | Closed | HIM-3 |  | Kim et al., 2014 |
| 4TZQ | *Ce* HTP-1 | Closed | HTP-3 CM 1 |  | Kim et al., 2014 |
| 4TZL | *Ce* HTP-2 | Closed | HIM-3 |  | Kim et al., 2014 |
| 4TZS | *Ce* HTP-2 | Closed | HIM-3 |  | Kim et al., 2014 |
| 4TZM | *Ce* HTP-2 | Closed | HTP-3 CM 1 |  | Kim et al., 2014 |
| 4TZN | *Ce* HTP-2 | Closed | HTP-3 CM 6 |  | Kim et al., 2014 |
| 4J2G | Lt Atg13 | Closed | Unliganded | There is no ligand, and the safety belt region is disordered | Jao et al., 2013 |
| 4WZG | *Hs* ATG101 | Open | N/A |  | Michel et al., 2015 |
| 4YK8 | *Sp* Atg13:Atg101 | Closed:open | Unliganded | Atg13 is closed and Atg101 is open | Suzuki et al., 2015 |
| 5C50 | *Hs* ATG13:ATG101 | Closed:open | Unliganded | Atg13 is closed and Atg101 is open | Qi et al., 2015 |

*Ce, Caenorhabditis elegans; Hs, Homo sapiens; Lt, Lachancea thermotolerans* (budding yeast); *Mm, Mus musculus*; N/A, not applicable; *Sp, Schizosaccharomyces pombe.*

[a] The asymmetric Mad2 dimer structures reported by Mapelli et al. (2007); closed:open); closed:open) and Hara et al. (2015); closed:intermediate); closed:intermediate) are nearly identical, despite being generated in a different manner. Based on NMR data, Hara et al. (2015) reinterpreted this structure as representing an intermediate state of Mad2 more prone to conformational conversion to the closed state.

## References

Aravind, L., and E.V. Koonin. 1998. The HORMA domain: a common structural denominator in mitotic checkpoints, chromosome synapsis and DNA repair. *Trends Biochem. Sci.* 23:284–286.

Aravind, L., and L.M. Iyer. 2002. The SWIRM domain: a conserved module found in chromosomal proteins points to novel chromatin-modifying activities. *Genome Biol.* 3:research0039–research0039.7. doi:10.1186/gb-2002-3-8-research0039.

Boersma, V., N. Moatti, S. Segura-Bayona, M.H. Peuscher, J. van der Torre, B.A. Wevers, A. Orthwein, D. Durocher, and J.J.L. Jacobs. 2015. MAD2L2 controls DNA repair at telomeres and DNA breaks by inhibiting 5' end resection. *Nature*. 521:537–540. doi:10.1038/nature14216.

Börner, G.V., A. Barot, and N. Kleckner. 2008. Yeast Pch2 promotes domainal axis organization, timely recombination progression, and arrest of defective recombinosomes during meiosis. *Proc. Natl. Acad. Sci. U.S.A.* 105:3327–3332. doi:10.1073/pnas.0711864105.

Brandão, L.N., R. Ferguson, I. Santoro, S. Jinks-Robertson, and R.A. Sclafani. 2014. The role of Dbf4-dependent protein kinase in DNA polymerase ζ-dependent mutagenesis in Saccharomyces cerevisiae. *Genetics*. 197:1111–1122. doi:10.1534/genetics.114.165308.

Cahill, D.P., L.T. da Costa, E.B. Carson-Walter, K.W. Kinzler, B. Vogelstein, and C. Lengauer. 1999. Characterization of MAD2B and other mitotic spindle checkpoint genes. *Genomics*. 58:181–187. doi:10.1006/geno.1999.5831.

Caryl, A.P., S.J. Armstrong, G.H. Jones, and F.C.H. Franklin. 2000. A homologue of the yeast HOP1 gene is inactivated in the Arabidopsis meiotic mutant asy1. *Chromosoma*. 109:62–71. doi:10.1007/s004120050413.

Chao, W.C.H., K. Kulkarni, Z. Zhang, E.H. Kong, and D. Barford. 2012. Structure of the mitotic checkpoint complex. *Nature*. 484:208–213. doi:10.1038/nature10896.

Chen, C., A. Jomaa, J. Ortega, and E.E. Alani. 2014. Pch2 is a hexameric ring ATPase that remodels the chromosome axis protein Hop1. *Proc. Natl. Acad. Sci. U.S.A.* 111:E44–53. doi:10.1073/pnas.1310755111.

Chen, J., and G. Fang. 2001. MAD2B is an inhibitor of the anaphase-promoting complex. *Genes & Development*. 15:1765–1770. doi:10.1101/gad.898701.

Chun, A.C.-S., K.-H. Kok, and D.-Y. Jin. 2013. REV7 is required for anaphase-promoting complex-dependent ubiquitination and degradation of translesion DNA polymerase REV1. *Cell Cycle*. 12:365–378. doi:10.4161/cc.23214.

Couteau, F., and M. Zetka. 2005. HTP-1 coordinates synaptonemal complex assembly with homolog alignment during meiosis in C. elegans. *Genes & Development*. 19:2744–2756. doi:10.1101/gad.1348205.

Date, D.A., A.C. Burrows, and M.K. Summers. 2014. Phosphorylation regulates the p31Comet-mitotic arrest-deficient 2 (Mad2) interaction to promote spindle assembly checkpoint (SAC) activity. *J. Biol. Chem.* 289:11367–11373. doi:10.1074/jbc.M113.520841.

De Antoni, A., C.G. Pearson, D. Cimini, J.C. Canman, V. Sala, L. Nezi, M. Mapelli, L. Sironi, M. Faretta, E.D. Salmon, and A. Musacchio. 2005. The Mad1/Mad2 complex as a template for Mad2 activation in the spindle assembly checkpoint. *Curr. Biol.* 15:214–225. doi:10.1016/j.cub.2005.01.038.

Eytan, E., K. Wang, S. Miniowitz-Shemtov, D. Sitry-Shevah, S. Kaisari, T.J. Yen, S.T. Liu, and A. Hershko. 2014. Disassembly of mitotic checkpoint complexes by the joint action of the AAA-ATPase TRIP13 and p31comet. *Proceedings of the National Academy of Sciences*. 111:12019–12024. doi:10.1073/pnas.1412901111.

Fattah, F.J., K. Hara, K.R. Fattah, C. Yang, N. Wu, R. Warrington, D.J. Chen, P. Zhou, D.A. Boothman, and H. Yu. 2014. The transcription factor TFII-I promotes DNA translesion synthesis and genomic stability. *PLoS Genet.* 10:e1004419. doi:10.1371/journal.pgen.1004419.

Ferdous, M., J.D. Higgins, K. Osman, C. Lambing, E. Roitinger, K. Mechtler, S.J. Armstrong, R. Perry, M. Pradillo, N. Cuñado, and F.C.H. Franklin. 2012. Inter-homolog crossing-over and synapsis in Arabidopsis meiosis are dependent on the chromosome axis protein AtASY3. *PLoS Genet.* 8:e1002507. doi:10.1371/journal.pgen.1002507.

Fujioka, Y., S.W. Suzuki, H. Yamamoto, C. Kondo-Kakuta, Y. Kimura, H. Hirano, R. Akada, F. Inagaki, Y. Ohsumi, and N.N. Noda. 2014. Structural basis of starvation-induced assembly of the autophagy initiation complex. *Nat. Struct. Mol. Biol.* 21:513–521. doi:10.1038/nsmb.2822.

Fukuda, T., K. Daniel, L. Wojtasz, A. Toth, and C. Höög. 2010. A novel mammalian HORMA domain-containing protein, HORMAD1, preferentially associates with unsynapsed meiotic chromosomes. *Exp. Cell Res.* 316:158–171. doi:10.1016/j.yexcr.2009.08.007.

Goodyer, W., S. Kaitna, F. Couteau, J.D. Ward, S.J. Boulton, and M. Zetka. 2008. HTP-3 links DSB formation with homolog pairing and crossing over during C. elegans meiosis. *Dev. Cell*. 14:263–274. doi:10.1016/j.devcel.2007.11.016.

Habu, T., S.H. Kim, J. Weinstein, and T. Matsumoto. 2002. Identification of a MAD2-binding protein, CMT2, and its role in mitosis. *EMBO J.* 21:6419–6428. doi:10.1093/emboj/cdf659.

Hagan, R.S., M.S. Manak, H.K. Buch, M.G. Meier, P. Meraldi, J.V. Shah, P.K. Sorger, and S.J. Doxsey. 2011. p31comet acts to ensure timely spindle checkpoint silencing subsequent to kinetochore attachment. *Mol. Biol. Cell*. 22:4236–4246. doi:10.1091/mbc.E11-03-0216.

Hanafusa, T., T. Habu, J. Tomida, E. Ohashi, Y. Murakumo, and H. Ohmori. 2010. Overlapping in short motif sequences for binding to human REV7 and MAD2 proteins. *Genes Cells*. 15:281–296. doi:10.1111/j.1365-2443.2009.01380.x.

Hara, K., H. Hashimoto, Y. Murakumo, S. Kobayashi, T. Kogame, S. Unzai, S. Akashi, S. Takeda, T. Shimizu, and M. Sato. 2010. Crystal structure of human REV7 in complex with a human REV3 fragment and structural implication of the interaction between DNA polymerase zeta and REV1. *J. Biol. Chem.* 285:12299–12307. doi:10.1074/jbc.M109.092403.

Hara, K., T. Shimizu, S. Unzai, S. Akashi, M. Sato, and H. Hashimoto. 2009. Purification, crystallization and initial X-ray diffraction study of human REV7 in complex with a REV3 fragment. *Acta Crystallogr. Sect. F Struct. Biol. Cryst. Commun.* 65:1302–1305. doi:10.1107/S1744309109046181.

Hara, M., E. Özkan, H. Sun, H. Yu, and X. Luo. 2015. Structure of an intermediate conformer of the spindle checkpoint protein Mad2. *Proc. Natl. Acad. Sci. U.S.A.* vol. 112:11252–11257. doi:10.1073/pnas.1512197112.

Haracska, L., I. Unk, R.E. Johnson, E. Johansson, P.M. Burgers, S. Prakash, and L. Prakash. 2001. Roles of yeast DNA polymerases delta and zeta and of Rev1 in the bypass of abasic sites. *Genes & Development*. 15:945–954. doi:10.1101/gad.882301.

Hegedűs, K., P. Nagy, Z. Gáspári, and G. Juhász. 2014. The putative HORMA domain protein Atg101 dimerizes and is required for starvation-induced and selective autophagy in Drosophila. *Biomed Res Int*. 2014:470482–13. doi:10.1155/2014/470482.

Hollingsworth, N.M., and A.D. Johnson. 1993. A conditional allele of the Saccharomyces cerevisiae HOP1 gene is suppressed by overexpression of two other meiosis-specific genes: RED1 and REC104. *Genetics*. 133:785–797.

Hollingsworth, N.M., L. Goetsch, and B. Byers. 1990. The HOP1 gene encodes a meiosis-specific component of yeast chromosomes. *Cell*. 61:73–84. doi:10.1016/0092-8674(90)90216-2.

Hosokawa, N., T. Sasaki, S.-I. Iemura, T. Natsume, T. Hara, and N. Mizushima. 2009. Atg101, a novel mammalian autophagy protein interacting with Atg13. *Autophagy*. 5:973–979.

Howell, B.J., B. Moree, E.M. Farrar, S. Stewart, G. Fang, and E.D. Salmon. 2004. Spindle checkpoint protein dynamics at kinetochores in living cells. *Curr. Biol.* 14:953–964. doi:10.1016/j.cub.2004.05.053.

Howell, B.J., B.F. McEwen, J.C. Canman, D.B. Hoffman, E.M. Farrar, C.L. Rieder, and E.D. Salmon. 2001. Cytoplasmic dynein/dynactin drives kinetochore protein transport to the spindle poles and has a role in mitotic spindle checkpoint inactivation. *J. Cell Biol.* 155:1159–1172. doi:10.1083/jcb.200105093.

Humphryes, N., and A. Hochwagen. 2014. A non-sister act: recombination template choice during meiosis. *Exp. Cell Res.* 329:53–60. doi:10.1016/j.yexcr.2014.08.024.

Hurley, J.H., and B.A. Schulman. 2014. Atomistic autophagy: the structures of cellular self-digestion. *Cell*. 157:300–311. doi:10.1016/j.cell.2014.01.070.

Jao, C.C., M.J. Ragusa, R.E. Stanley, and J.H. Hurley. 2013. A HORMA domain in Atg13 mediates PI 3-kinase recruitment in autophagy. *Proc. Natl. Acad. Sci. U.S.A.* 110:5486–5491. doi:10.1073/pnas.1220306110.

Kabeya, Y., Y. Kamada, M. Baba, H. Takikawa, M. Sasaki, and Y. Ohsumi. 2005. Atg17 functions in cooperation with Atg1 and Atg13 in yeast autophagy. *Mol. Biol. Cell*. 16:2544–2553. doi:10.1091/mbc.E04-08-0669.

Kamada, Y., T. Funakoshi, T. Shintani, K. Nagano, M. Ohsumi, and Y. Ohsumi. 2000. Tor-mediated induction of autophagy via an Apg1 protein kinase complex. *J. Cell Biol.* 150:1507–1513.

Kauppi, L., M. Barchi, J. Lange, F. Baudat, M. Jasin, and S. Keeney. 2013. Numerical constraints and feedback control of double-strand breaks in mouse meiosis. *Genes & Development*. 27:873–886. doi:10.1101/gad.213652.113.

Kikuchi, S., K. Hara, T. Shimizu, M. Sato, and H. Hashimoto. 2012. Structural basis of recruitment of DNA polymerase ζ by interaction between REV1 and REV7 proteins. *J. Biol. Chem.* 287:33847–33852. doi:10.1074/jbc.M112.396838.

Kim, Y., S.C. Rosenberg, C.L. Kugel, N. Kostow, O. Rog, V. Davydov, T.Y. Su, A.F. Dernburg, and K.D. Corbett. 2014. The Chromosome Axis Controls Meiotic Events through a Hierarchical Assembly of HORMA Domain Proteins. *Dev. Cell*. 31:487–502. doi:10.1016/j.devcel.2014.09.013.

Kironmai, K.M., K. Muniyappa, D.B. Friedman, N.M. Hollingsworth, and B. Byers. 1998. DNA-binding activities of Hop1 protein, a synaptonemal complex component from Saccharomyces cerevisiae. *Mol. Cell. Biol.* 18:1424–1435.

Kraft, C., F. Herzog, C. Gieffers, K. Mechtler, A. Hagting, J. Pines, and J.-M. Peters. 2003. Mitotic regulation of the human anaphase-promoting complex by phosphorylation. *EMBO J.* 22:6598–6609. doi:10.1093/emboj/cdg627.

Lambing, C., K. Osman, K. Nuntasoontorn, A. West, J.D. Higgins, G.P. Copenhaver, J. Yang, S.J. Armstrong, K. Mechtler, E. Roitinger, and F.C.H. Franklin. 2015. Arabidopsis PCH2 Mediates Meiotic Chromosome Remodeling and Maturation of Crossovers. *PLoS Genet.* 11:e1005372. doi:10.1371/journal.pgen.1005372.

Lara-Gonzalez, P., F.G. Westhorpe, and S.S. Taylor. 2012. The spindle assembly checkpoint. *Curr. Biol.* 22:R966–80. doi:10.1016/j.cub.2012.10.006.

Listovsky, T., and J.E. Sale. 2013. Sequestration of CDH1 by MAD2L2 prevents premature APC/C activation prior to anaphase onset. *J. Cell Biol.* 203:87–100. doi:10.1083/jcb.201302060.

London, N., and S. Biggins. 2014. Signalling dynamics in the spindle checkpoint response. *Nat. Rev. Mol. Cell Biol.* 15:736–747. doi:10.1038/nrm3888.

Luo, X., and H. Yu. 2008. Protein metamorphosis: the two-state behavior of Mad2. *Structure*. 16:1616–1625. doi:10.1016/j.str.2008.10.002.

Luo, X., G. Fang, M. Coldiron, Y. Lin, H. Yu, M.W. Kirschner, and G. Wagner. 2000. Structure of the Mad2 spindle assembly checkpoint protein and its interaction with Cdc20. *Nat. Struct. Biol.* 7:224–229. doi:10.1038/73338.

Luo, X., Z. Tang, G. Xia, K. Wassmann, T. Matsumoto, J. Rizo, and H. Yu. 2004. The Mad2 spindle checkpoint protein has two distinct natively folded states. *Nat. Struct. Mol. Biol.* 11:338–345. doi:10.1038/nsmb748.

Luo, X., Z. Tang, J. Rizo, and H. Yu. 2002. The Mad2 spindle checkpoint protein undergoes similar major conformational changes upon binding to either Mad1 or Cdc20. *Mol. Cell*. 9:59–71. doi:10.1016/S1097-2765(01)00435-X.

MacQueen, A.J., and A. Hochwagen. 2011. Checkpoint mechanisms: the puppet masters of meiotic prophase. *Trends Cell Biol.* 21:393–400. doi:10.1016/j.tcb.2011.03.004.

Makarova, A.V., and P.M. Burgers. 2015. Eukaryotic DNA polymerase ζ. *DNA Repair (Amst.)*. 29:47–55. doi:10.1016/j.dnarep.2015.02.012.

Mao-Draayer, Y., A.M. Galbraith, D.L. Pittman, M. Cool, and R.E. Malone. 1996. Analysis of meiotic recombination pathways in the yeast Saccharomyces cerevisiae. *Genetics*. 144:71–86.

Mapelli, M., and A. Musacchio. 2007. MAD contortions: conformational dimerization boosts spindle checkpoint signaling. *Curr. Opin. Struct. Biol.* 17:716–725. doi:10.1016/j.sbi.2007.08.011.

Mapelli, M., F.V. Filipp, G. Rancati, L. Massimiliano, L. Nezi, G. Stier, R.S. Hagan, S. Confalonieri, S. Piatti, M. Sattler, and A. Musacchio. 2006. Determinants of conformational dimerization of Mad2 and its inhibition by p31comet. *EMBO J.* 25:1273–1284. doi:10.1038/sj.emboj.7601033.

Mapelli, M., L. Massimiliano, S. Santaguida, and A. Musacchio. 2007. The Mad2 conformational dimer: structure and implications for the spindle assembly checkpoint. *Cell*. 131:730–743. doi:10.1016/j.cell.2007.08.049.

Medendorp, K., J.J.M. van Groningen, L. Vreede, L. Hetterschijt, W.H. van den Hurk, D.R.H. de Bruijn, L. Brugmans, and A.G. van Kessel. 2009. The mitotic arrest deficient protein MAD2B interacts with the small GTPase RAN throughout the cell cycle. *PLoS ONE*. 4:e7020. doi:10.1371/journal.pone.0007020.

Medendorp, K., L. Vreede, J.J.M. van Groningen, L. Hetterschijt, L. Brugmans, P.A.M. Jansen, W.H. van den Hurk, D.R.H. de Bruijn, and A.G. van Kessel. 2010. The mitotic arrest deficient protein MAD2B interacts with the clathrin light chain A during mitosis. *PLoS ONE*. 5:e15128. doi:10.1371/journal.pone.0015128.

Mercer, C.A., A. Kaliappan, and P.B. Dennis. 2009. A novel, human Atg13 binding protein, Atg101, interacts with ULK1 and is essential for macroautophagy. *Autophagy*. 5:649–662. doi:10.4161/auto.5.5.8249.

Michel, M., M. Schwarten, C. Decker, L. Nagel-Steger, D. Willbold, and O.H. Weiergräber. 2015. The mammalian autophagy initiator complex contains two HORMA domain proteins. *Autophagy*. 0. doi:10.1080/15548627.2015.1076605.

Mizushima, N. 2007. Autophagy: process and function. *Genes & Development*. 21:2861–2873. doi:10.1101/gad.1599207.

Mizushima, N. 2010. The role of the Atg1/ULK1 complex in autophagy regulation. *Curr. Opin. Cell Biol.* 22:132–139. doi:10.1016/j.ceb.2009.12.004.

Mo, M., A. Arnaoutov, and M. Dasso. 2015. Phosphorylation of Xenopus p31(comet) potentiates mitotic checkpoint exit. *Cell Cycle*. 0. doi:10.1080/15384101.2015.1033590.

Muniyappa, K., R. Kshirsagar, and I. Ghodke. 2014. The HORMA domain: an evolutionarily conserved domain discovered in chromatin-associated proteins, has unanticipated diverse functions. *Gene*. 545:194–197. doi:10.1016/j.gene.2014.05.020.

Musacchio, A., and E.D. Salmon. 2007. The spindle-assembly checkpoint in space and time. *Nat. Rev. Mol. Cell Biol.* 8:379–393. doi:10.1038/nrm2163.

Nelson, J.R., C.W. Lawrence, and D.C. Hinkle. 1996a. Thymine-Thymine Dimer Bypass by Yeast DNA Polymerase zeta. *Science*. 272:1646–1649. doi:10.1126/science.272.5268.1646.

Nelson, J.R., C.W. Lawrence, and D.C. Hinkle. 1996b. Deoxycytidyl transferase activity of yeast REV1 protein. *Nature*. 382:729–731. doi:10.1038/382729a0.

Nelson, J.R., P.E. Gibbs, A.M. Nowicka, D.C. Hinkle, and C.W. Lawrence. 2000. Evidence for a second function for Saccharomyces cerevisiae Rev1p. *Mol. Microbiol.* 37:549–554.

Orth, M., B. Mayer, K. Rehm, U. Rothweiler, D. Heidmann, T.A. Holak, and O.

Stemmann. 2011. Shugoshin is a Mad1/Cdc20-like interactor of Mad2. *EMBO J.* 30:2868–2880. doi:10.1038/emboj.2011.187.

Pfleger, C.M., A. Salic, E. Lee, and M.W. Kirschner. 2001. Inhibition of Cdh1-APC by the MAD2-related protein MAD2L2: a novel mechanism for regulating Cdh1. *Genes & Development*. 15:1759–1764. doi:10.1101/gad.897901.

Pines, J. 2011. Cubism and the cell cycle: the many faces of the APC/C. *Nat. Rev. Mol. Cell Biol.* 12:427–438. doi:10.1038/nrm3132.

Pirouz, M., A. Rahjouei, F. Shamsi, K.N. Eckermann, G. Salinas-Riester, C. Pommerenke, and M. Kessel. 2015. Destabilization of pluripotency in the absence of Mad2l2. *Cell Cycle*. 14:1596–1610. doi:10.1080/15384101.2015.1026485.

Pirouz, M., S. Pilarski, and M. Kessel. 2013. A critical function of Mad2l2 in primordial germ cell development of mice. *PLoS Genet.* 9:e1003712. doi:10.1371/journal.pgen.1003712.

Prakash, S., R.E. Johnson, and L. Prakash. 2005. Eukaryotic translesion synthesis DNA polymerases: specificity of structure and function. *Annu. Rev. Biochem.* 74:317–353. doi:10.1146/annurev.biochem.74.082803.133250.

Primorac, I., and A. Musacchio. 2013. Panta rhei: the APC/C at steady state. *J. Cell Biol.* 201:177–189. doi:10.1083/jcb.201301130.

Qi, S., D.J. Kim, G. Stjepanovic, and J.H. Hurley. 2015. Structure of the Human Atg13-Atg101 HORMA Heterodimer: an Interaction Hub within the ULK1 Complex. *Structure*. doi:10.1016/j.str.2015.07.011.

Ragusa, M.J., R.E. Stanley, and J.H. Hurley. 2012. Architecture of the Atg17 complex as a scaffold for autophagosome biogenesis. *Cell*. 151:1501–1512. doi:10.1016/j.cell.2012.11.028.

Reddy, S.K., M. Rape, W.A. Margansky, and M.W. Kirschner. 2007. Ubiquitination by the anaphase-promoting complex drives spindle checkpoint inactivation. *Nature*. 446:921–925. doi:10.1038/nature05734.

Ross, A.-L., L.J. Simpson, and J.E. Sale. 2005. Vertebrate DNA damage tolerance requires the C-terminus but not BRCT or transferase domains of REV1. *Nucleic Acids Res.* 33:1280–1289. doi:10.1093/nar/gki279.

Sakuno, T., and Y. Watanabe. 2015. Phosphorylation of cohesin Rec11/SA3 by casein kinase 1 promotes homologous recombination by assembling the meiotic chromosome axis. *Dev. Cell*. 32:220–230. doi:10.1016/j.devcel.2014.11.033.

Sale, J.E. 2013. Translesion DNA synthesis and mutagenesis in eukaryotes. *Cold Spring Harb Perspect Biol*. 5:a012708–a012708. doi:10.1101/cshperspect.a012708.

San-Segundo, P.A., and G.S. Roeder. 1999. Pch2 links chromatin silencing to meiotic checkpoint control. *Cell*. 97:313–324. doi:10.1016/S0092-8674(00)80741-2.

Shah, J.V., E. Botvinick, Z. Bonday, F. Furnari, M. Berns, and D.W. Cleveland. 2004. Dynamics of centromere and kinetochore proteins; implications for checkpoint signaling and silencing. *Curr. Biol.* 14:942–952. doi:10.1016/j.cub.2004.05.046.

Shin, Y.-H., Y. Choi, S.U. Erdin, S.A. Yatsenko, M. Kloc, F. Yang, P.J. Wang, M.L. Meistrich, and A. Rajkovic. 2010. Hormad1 mutation disrupts synaptonemal complex formation, recombination, and chromosome segregation in mammalian meiosis. *PLoS Genet.* 6:e1001190. doi:10.1371/journal.pgen.1001190.

Sironi, L., M. Mapelli, S. Knapp, A. De Antoni, K.-T. Jeang, and A. Musacchio. 2002. Crystal structure of the tetrameric Mad1-Mad2 core complex: implications of a "safety belt" binding mechanism for the spindle checkpoint. *EMBO J.* 21:2496–2506. doi:10.1093/emboj/21.10.2496.

Sironi, L., M. Melixetian, M. Faretta, E. Prosperini, K. Helin, and A. Musacchio. 2001. Mad2 binding to Mad1 and Cdc20, rather than oligomerization, is required for the spindle checkpoint. *EMBO J.* 20:6371–6382. doi:10.1093/emboj/20.22.6371.

Sivakumar, S., and G.J. Gorbsky. 2015. Spatiotemporal regulation of the anaphase-promoting complex in mitosis. *Nat. Rev. Mol. Cell Biol.* 16:82–94. doi:10.1038/nrm3934.

Smith, A.V., and G.S. Roeder. 1997. The yeast Red1 protein localizes to the cores of meiotic chromosomes. *J. Cell Biol.* 136:957–967. doi:10.1083/jcb.136.5.957.

Stjepanovic, G., C.W. Davies, R.E. Stanley, M.J. Ragusa, D.J. Kim, and J.H. Hurley. 2014. Assembly and dynamics of the autophagy-initiating Atg1 complex. *Proc. Natl. Acad. Sci. U.S.A.* 111:12793–12798. doi:10.1073/pnas.1407214111.

Subramanian, V.V., and A. Hochwagen. 2014. The meiotic checkpoint network: step-by-step through meiotic prophase. *Cold Spring Harb Perspect Biol*. 6:a016675–a016675. doi:10.1101/cshperspect.a016675.

Sudakin, V., G.K. Chan, and T.J. Yen. 2001. Checkpoint inhibition of the APC/C in HeLa cells is mediated by a complex of BUBR1, BUB3, CDC20, and MAD2. *J. Cell Biol.* 154:925–936. doi:10.1083/jcb.200102093.

Suzuki, H., T. Kaizuka, N. Mizushima, and N.N. Noda. 2015a. Structure of the Atg101-Atg13 complex reveals essential roles of Atg101 in autophagy initiation. *Nat. Struct. Mol. Biol.* doi:10.1038/nsmb.3036.

Suzuki, S.W., H. Yamamoto, Y. Oikawa, C. Kondo-Kakuta, Y. Kimura, H. Hirano, and Y. Ohsumi. 2015b. Atg13 HORMA domain recruits Atg9 vesicles during autophagosome formation. *Proc. Natl. Acad. Sci. U.S.A.* 112:3350–3355. doi:10.1073/pnas.1421092112.

Teichner, A., E. Eytan, D. Sitry-Shevah, S. Miniowitz-Shemtov, E. Dumin, J. Gromis, and A. Hershko. 2011. p31comet Promotes disassembly of the mitotic checkpoint complex in an ATP-dependent process. *Proc. Natl. Acad. Sci. U.S.A.* 108:3187–3192. doi:10.1073/pnas.1100023108.

Thacker, D., N. Mohibullah, X. Zhu, and S. Keeney. 2014. Homologue engagement controls meiotic DNA break number and distribution. *Nature*. 510:241–246. doi:10.1038/nature13120.

Tipton, A.R., K. Wang, P. Oladimeji, S. Sufi, Z. Gu, and S.-T. Liu. 2012. Identification of novel mitosis regulators through data mining with human centromere/kinetochore proteins as group queries. *BMC Cell Biol.* 13:15. doi:10.1186/1471-2121-13-15.

Tomida, J., K.-I. Takata, S.S. Lange, A.C. Schibler, M.J. Yousefzadeh, S. Bhetawal, S.Y.R. Dent, and R.D. Wood. 2015. REV7 is essential for DNA damage tolerance via two REV3L binding sites in mammalian DNA polymerase ζ. *Nucleic Acids Res.* 43:1000–1011. doi:10.1093/nar/gku1385.

Vader, G., and A. Musacchio. 2014. HORMA domains at the heart of meiotic chromosome dynamics. *Dev. Cell*. 31:389–391. doi:10.1016/j.devcel.2014.11.009.

Vermeulen, M., H.C. Eberl, F. Matarese, H. Marks, S. Denissov, F. Butter, K.K. Lee, J.V. Olsen, A.A. Hyman, H.G. Stunnenberg, and M. Mann. 2010. Quantitative interaction proteomics and genome-wide profiling of epigenetic histone marks and their readers. *Cell*. 142:967–980. doi:10.1016/j.cell.2010.08.020.

Vink, M., M. Simonetta, P. Transidico, K. Ferrari, M. Mapelli, A. De Antoni, L. Massimiliano, A. Ciliberto, M. Faretta, E.D. Salmon, and A. Musacchio. 2006. In vitro FRAP identifies the minimal requirements for Mad2 kinetochore dynamics. *Curr. Biol.* 16:755–766. doi:10.1016/j.cub.2006.03.057.

Wang, K., B. Sturt-Gillespie, J.C. Hittle, D. Macdonald, G.K. Chan, T.J. Yen, and S.-T. Liu. 2014. Thyroid hormone receptor interacting protein 13 (TRIP13) AAA-ATPase is a novel mitotic checkpoint-silencing protein. *J. Biol. Chem.* 289:23928–23937. doi:10.1074/jbc.M114.585315.

Wang, K., M. Wang, D. Tang, Y. Shen, B. Qin, M. Li, and Z. Cheng. 2011. PAIR3, an axis-associated protein, is essential for the recruitment of recombination elements onto meiotic chromosomes in rice. *Mol. Biol. Cell*. 22:12–19. doi:10.1091/mbc.E10-08-0667.

Watanabe, N., S. Mii, N. Asai, M. Asai, K. Niimi, K. Ushida, T. Kato, A. Enomoto, H. Ishii, M. Takahashi, and Y. Murakumo. 2013. The REV7 subunit of DNA polymerase ζ is essential for primordial germ cell maintenance in the mouse. *J. Biol. Chem.* 288:10459–10471. doi:10.1074/jbc.M112.421966.

Waters, L.S., B.K. Minesinger, M.E. Wiltrout, S. D'Souza, R.V. Woodruff, and G.C. Walker. 2009. Eukaryotic translesion polymerases and their roles and regulation in

DNA damage tolerance. *Microbiol. Mol. Biol. Rev.* 73:134–154. doi:10.1128/MMBR.00034-08.

Westhorpe, F.G., A. Tighe, P. Lara-Gonzalez, and S.S. Taylor. 2011. p31comet-mediated extraction of Mad2 from the MCC promotes efficient mitotic exit. *J. Cell. Sci.* 124:3905–3916. doi:10.1242/jcs.093286.

Wojtasz, L., J.M. Cloutier, M. Baumann, K. Daniel, J. Varga, J. Fu, K. Anastassiadis, A.F. Stewart, A. Reményi, J.M.A. Turner, and A. Toth. 2012. Meiotic DNA double-strand breaks and chromosome asynapsis in mice are monitored by distinct HORMAD2-independent and -dependent mechanisms. *Genes & Development*. 26:958–973. doi:10.1101/gad.187559.112.

Wojtasz, L., K. Daniel, I. Roig, E. Bolcun-Filas, H. Xu, V. Boonsanay, C.R. Eckmann, H.J. Cooke, M. Jasin, S. Keeney, M.J. McKay, and A. Toth. 2009. Mouse HORMAD1 and HORMAD2, two conserved meiotic chromosomal proteins, are depleted from synapsed chromosome axes with the help of TRIP13 AAA-ATPase. *PLoS Genet.* 5:e1000702. doi:10.1371/journal.pgen.1000702.

Wojtaszek, J., C.-J. Lee, S. D'Souza, B. Minesinger, H. Kim, A.D. D'Andrea, G.C. Walker, and P. Zhou. 2012. Structural basis of Rev1-mediated assembly of a quaternary vertebrate translesion polymerase complex consisting of Rev1, heterodimeric polymerase (Pol) ζ, and Pol κ. *J. Biol. Chem.* 287:33836–33846. doi:10.1074/jbc.M112.394841.

Woltering, D., B. Baumgartner, S. Bagchi, B. Larkin, J. Loidl, T. de los Santos, and N.M. Hollingsworth. 2000. Meiotic segregation, synapsis, and recombination checkpoint functions require physical interaction between the chromosomal proteins Red1p and Hop1p. *Mol. Cell. Biol.* 20:6646–6658. doi:10.1128/MCB.20.18.6646-6658.2000.

Xia, G., X. Luo, T. Habu, J. Rizo, T. Matsumoto, and H. Yu. 2004. Conformation-specific binding of p31(comet) antagonizes the function of Mad2 in the spindle checkpoint. *EMBO J.* 23:3133–3143. doi:10.1038/sj.emboj.7600322.

Xie, W., X. Yang, M. Xu, and T. Jiang. 2012. Structural insights into the assembly of human translesion polymerase complexes. *Protein Cell*. 3:864–874. doi:10.1007/s13238-012-2102-x.

Xie, Z., and D.J. Klionsky. 2007. Autophagosome formation: core machinery and adaptations. *Nat. Cell Biol.* 9:1102–1109. doi:10.1038/ncb1007-1102.

Xu, G., J.R. Chapman, I. Brandsma, J. Yuan, M. Mistrik, P. Bouwman, J. Bartkova, E. Gogola, D. Warmerdam, M. Barazas, J.E. Jaspers, K. Watanabe, M. Pieterse, A. Kersbergen, W. Sol, P.H.N. Celie, P.C. Schouten, B. van den Broek, A. Salman, M. Nieuwland, I. de Rink, J. de Ronde, K. Jalink, S.J. Boulton, J. Chen, D.C. van Gent, J. Bartek, J. Jonkers, P. Borst, and S. Rottenberg. 2015. REV7 counteracts DNA double-strand break resection and affects PARP inhibition. *Nature*. 521:541–544. doi:10.1038/nature14328.

Yamada, M., K. Watanabe, M. Mistrik, E. Vesela, I. Protivankova, N. Mailand, M. Lee, H. Masai, J. Lukas, and J. Bartek. 2013. ATR-Chk1-APC/CCdh1-dependent stabilization of Cdc7-ASK (Dbf4) kinase is required for DNA lesion bypass under replication stress. *Genes & Development*. 27:2459–2472. doi:10.1101/gad.224568.113.

Yang, M., B. Li, C.-J. Liu, D.R. Tomchick, M. Machius, J. Rizo, H. Yu, and X. Luo. 2008. Insights into mad2 regulation in the spindle checkpoint revealed by the crystal structure of the symmetric mad2 dimer. *PLoS Biol.* 6:e50. doi:10.1371/journal.pbio.0060050.

Yang, M., B. Li, D.R. Tomchick, M. Machius, J. Rizo, H. Yu, and X. Luo. 2007. p31comet blocks Mad2 activation through structural mimicry. *Cell*. 131:744–755. doi:10.1016/j.cell.2007.08.048.

Ye, Q., S.C. Rosenberg, A. Moeller, J.A. Speir, T.Y. Su, and K.D. Corbett. 2015. TRIP13 is a protein-remodeling AAA+ ATPase that catalyzes MAD2 conformation switching. *Elife*. 4:e07367. doi:10.7554/eLife.07367.

Yeh, Y.-Y., K.H. Shah, and P.K. Herman. 2011. An Atg13 protein-mediated self-association of the Atg1 protein kinase is important for the induction of autophagy. *J. Biol. Chem.* 286:28931–28939. doi:10.1074/jbc.M111.250324.

Zhang, L., S.-H. Yang, and A.D. Sharrocks. 2007. Rev7/MAD2B links c-Jun N-terminal protein kinase pathway signaling to activation of the transcription factor Elk-1. *Mol. Cell. Biol.* 27:2861–2869. doi:10.1128/MCB.02276-06.

## Acknowledgements

Chapter 0 (Introduction), in full, is a reprint of the material as it appears in The multifaceted roles of the HORMA domain in cellular signaling. J Cell Biol. 2015 Nov 23;211(4):745-55. doi: 10.1083/jcb.201509076. Review. PubMed PMID: 26598612; PubMed Central PMCID: PMC4657174. Rosenberg SC, Corbett KD. The dissertation author is the primary author for this paper.

The authors thank Juan Wang, Susan Ferro-Novick, Pablo Lara Gonzalez, Dhanya Cheerambathur, Arshad Desai, Yumi Kim, and members of the Corbett laboratory for critical reading and helpful discussions.

K.D. Corbett acknowledges support from the Ludwig Institute for Cancer Research and the National Institutes of Health (R01GM104141).

The authors declare no competing financial interests.

# Chapter 1: The chromosome axis controls meiotic events through a hierarchical assembly of HORMA domain proteins

## 1.1 Summary

Proteins of the HORMA domain family play central but poorly understood roles in chromosome organization and dynamics during meiosis. In *C. elegans*, four such proteins (HIM-3, HTP-1, HTP-2, and HTP-3) have distinct but overlapping functions. Through combined biochemical, structural, and *in vivo* analysis, we find that these proteins form hierarchical complexes through binding of their HORMA domains to cognate peptides within their partners' C-terminal tails, analogous to the "safety belt" binding mechanism of Mad2. These interactions are critical for recruitment of HIM-3, HTP-1, and HTP-2 to chromosome axes. HTP-3, in addition to recruiting the other HORMA domain proteins to the axis, plays an independent role in sister chromatid cohesion and double-strand break formation. Finally, we find that mammalian HORMAD1 binds a peptide motif found both at its own C-terminus and that of HORMAD2, indicating that this mode of intermolecular association is a conserved feature of meiotic chromosome structure in eukaryotes.

## 1.2 Introduction

Meiosis is the specialized cell division program in which homologs, and then sister chromatids, segregate from one another in two successive divisions to generate haploid gametes. The emergence of this process during evolution required major innovations in chromosome organization and function. A ubiquitous feature of meiosis is the formation of chromosome axes, which organize replicated chromosomes into linear arrays of DNA loops (Blat et al., 2002; Zickler and Kleckner, 1999). These axes form the lateral elements of the tripartite synaptonemal complex (SC), which brings homologs into close juxtaposition (synapsis) (Kleckner, 2006; Zickler and Kleckner, 1999). Axis assembly is essential for homologous pairing and synapsis, and is also required for proper initiation and regulation of the specialized homologous recombination pathway that physically links homologs through crossover formation (Panizza et al. 2011; Niu 2005; Schwacha and Kleckner 1997). The axis comprises meiosis-specific cohesin complexes and, in most species, meiosis-specific HORMA domain-containing proteins. How these proteins contribute to profoundly reorganize chromosomes and to govern meiotic chromosome dynamics remains unknown.

The HORMA domain was first recognized by sequence similarity in three functionally diverse budding yeast proteins: Hop1, the fungal meiotic chromosome axis protein; Rev7, an accessory subunit of the translesion DNA polymerase ζ; and the spindle assembly checkpoint protein Mad2 (HORMA: Hop1/Rev7/Mad2) (Aravind and Koonin, 1998). More recently, HORMA domains have been characterized in the Mad2 regulator p31$^{\text{comet}}$ and the autophagy factor Atg13 (Jao et al., 2013; Xia et al., 2004; Yang et al., 2007). The best-studied HORMA domain protein, Mad2, is an essential kinetochore protein that binds and inhibits Cdc20 to prevent APC/C activation and anaphase onset until kinetochores are attached to spindle microtubules. Structural studies have shown that Mad2 undergoes a conformational change from an “open” to a “closed” conformation when it binds to short peptides within Cdc20 or Mad1, a kinetochore adaptor for Mad2 (Luo et al., 2002; 2004; Sironi et al., 2002). Through dimerization with closed Mad2 at the kinetochore, soluble open Mad2 switches to the closed conformation to become an active, diffusible Cdc20 inhibitor. Currently, it remains unclear whether other HORMA domain proteins, including the meiosis-specific family members, share these properties of conformational switching and binding partner exchange.

Throughout eukaryotic phyla, the meiosis-specific HORMA domain proteins localize to and are required for formation of the meiotic chromosome axis. There they promote double- strand DNA break (DSB) formation by Spo11/SPO-11 (Goodyer et al., 2008; Panizza et al., 2011), bias recombination toward the homolog to promote crossover formation (Martinez-Perez and Villeneuve, 2005; Niu, 2005; Schwacha and Kleckner, 1997), mediate homolog pairing and SC assembly (Daniel et al., 2011; Hollingsworth et al., 1990; Wojtasz et al., 2009), and participate in meiotic checkpoints that monitor synapsis and/or crossover formation (Baumgartner et al., 2000; Wojtasz et al., 2012). Fungi and plants have a single meiosis-specific HORMA domain protein (Caryl et al., 2000; Hollingsworth and Johnson, 1993) while mammals express two paralogs (HORMAD1 and 2) (Chen et al., 2005; Fukuda et al., 2010; Pangas et al., 2004; Wojtasz et al., 2009), and the nematode *C. elegans* has four (Couteau and Zetka, 2005; Goodyer et al., 2008; Hodgkin et al., 1979). The four meiotic HORMA domain proteins in *C. elegans* (HIM-3, HTP-1, HTP-2, and HTP-3) have related but distinct functions. HTP-3 is required for the proper axis localization of meiotic cohesin complexes and HIM-3, HTP-1, and HTP-2 (Goodyer et al., 2008; Severson et al., 2009), and its absence leads to failures in homolog pairing, synapsis, and DSB formation (Goodyer et al., 2008). HIM-3 is dispensable for cohesin or HTP-3 association with the chromosome axis, but is required for homolog pairing and synapsis (Couteau et al., 2004; Zetka et al., 1999). HIM-3 also promotes crossover formation by biasing recombination to the homolog instead of the sister chromosome, reflecting a conserved function with fungal and mammalian HORMA domain proteins (Couteau and Zetka, 2011; Couteau et al., 2004; Martinez-Perez and Villeneuve, 2005; Niu, 2005; Schwacha and Kleckner, 1997; Shin et al., 2010; Wojtasz et al., 2009; 2012; Zetka et al., 1999). Finally, HTP-1 and HTP-2 are highly similar to one another and appear to play partially overlapping roles. While *htp-2* mutants have no obvious meiotic defects, *htp-1* mutants exhibit extensive nonhomologous synapsis, suggesting a role in restricting SC assembly to occur between properly paired homologs (Couteau and Zetka, 2005; Martinez-Perez and Villeneuve, 2005). These proteins also play a role in defining the pattern of cohesin cleavage during the meiotic divisions. In *C. elegans*, the single crossover site on each holocentric chromosome defines two distinct regions, a “short arm” where cohesion is released during meiosis I and “long arm” that retains cohesion until meiosis II (Kaitna et al., 2002; Nabeshima et al., 2005; Rogers et al., 2002). While HTP-3 and HIM-3 persist along both arms, HTP-1 and HTP-2 become restricted to the long arms in late prophase (Martinez-Perez et al., 2008) mirroring the localization of LAB-1, a direct protector of cohesin complex integrity (de Carvalho et al., 2008; Tzur et al., 2012).

Despite their wide conservation and fundamental roles in meiosis, how the HORMA domain proteins interact with each other to establish the meiotic chromosome axis and to govern chromosome dynamics during meiosis is unknown. Combining *in vitro* reconstitution, X-ray crystallography, and *in vivo* analysis of mutant proteins, we show that the *C. elegans* meiotic HORMA domain proteins form a hierarchical complex whose architecture is dictated by specific associations between each protein’s HORMA domain and short motifs, termed “closure motifs”, in the proteins’ C-terminal tails. This complex is unique to the meiotic HORMA domain proteins, and is critical for the assembly of the chromosome axis, formation of the SC, and the faithful segregation of chromosomes in meiosis.

## 1.3 Results

### 1.3.1 The structure of HIM-3 reveals a conserved C-terminal "closure motif"

To establish the molecular basis for meiotic HORMA domain protein function, we sought to determine these proteins' 3D structures. The four *C. elegans* meiotic HORMA domain proteins share a similar domain structure, with an N-terminal HORMA domain and a variable-length C-terminal tail predicted to lack intrinsic structure, ranging from ~50 residues in HIM-3 to ~100 residues in HTP-1 and HTP-2, and over 500 residues in HTP-3.

We first crystallized and determined the 3D structure of full-length HIM-3 to a resolution of 1.75 Å (Table S1.1). Residues 19-248 (of 291) of HIM-3 adopts a HORMA domain fold, consisting of a seven-stranded β-sheet backed on one side by three long α-helices (Figure 1.1A). This structure is extremely similar to those of Mad2 and Rev7 in their "closed" conformations (Figure S1.1A). The most significant structural difference between HIM-3 and previously characterized HORMA domain proteins is an extended loop between β5 and αC (residues 127-158 in HIM-3), which drapes over the β-sheet and forms an additional short α-helix not observed in Mad2 or Rev7. This loop is intimately associated with the C-terminal β-strands β8′ and β8″ through both ionic and Van der Waals interactions, potentially stabilizing HIM-3 in the closed state (see below).

In the closed states of Mad2 and Rev7, a peptide ligand forms a β-strand that packs against strand β6 of the HORMA domain and is held in place by a "safety belt" encompassing β-strands β7, β8′, and β8″ (Hara et al., 2010; Luo et al., 2002; Sironi et al., 2002). In our structure of HIM-3, experimental electron density maps clearly revealed a peptide forming a β-strand apposed to β6. The high resolution of our structure enabled us to unambiguously identify this peptide as residues 278-286 of HIM-3 (Residues ~249-277 are disordered in our structure; Figure 1.1, S1.3A). Because HIM-3 adopts a closed conformation around this C-terminal motif, we designate it the HIM-3 “closure motif”.

Sequence alignments of HIM-3 orthologs in related nematodes revealed that the HIM-3 closure motif is highly conserved, particularly a Pro-Tyr-Gly motif that is closely associated with the “safety belt” of the HORMA domain in our structure (Figure 1.1B,C, S1.1B). We also identified a similar conserved motif near the C-termini of HTP-1 and HTP-2 and their orthologs, which contains a nearly invariant Pro-Tyr-Ser motif (Figure 1.1C, S1.1C). The long C-terminal tail of HTP-3 has a repetitive sequence in which six motifs bearing signatures of the HIM-3 closure motif can be discerned (Figure 1.1C). Four of these motifs (#2-5) are nearly identical to one another, and flanking these four motifs are two variable motifs (#1 and 6), with motif #6 located at the extreme C-terminus of HTP-3. Sequence alignments of HTP-3 orthologs from related nematodes reveal only limited sequence homology outside the HORMA domain, but we were able to identify potential closure motifs in the C-termini of HTP-3 orthologs from *C. briggsae, C. remanei, C. brenneri, C. japonica,* and *C. sp. 5* (Figure S1.1D).

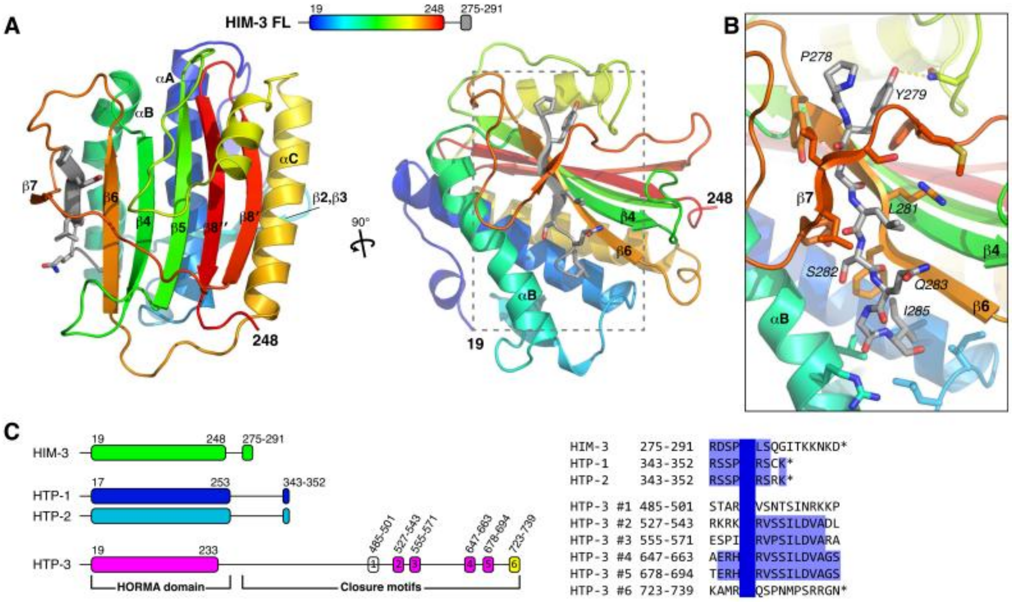

**Figure 1.1 Structure of C. elegans HIM-3 reveals conserved "closure motifs"**

(A) Two views of C. elegans HIM-3, with HORMA domain colored as a rainbow from N- to C-termini and secondary structure elements labeled according to the Mad2 convention (Luo et al., 2002; Sironi et al., 2002), with the C-terminal "closure motif" residues 278-285 in gray (see schematic, top). See Figure S1A for comparison with Mad2 and Rev7. (B) Detail view showing interactions between the closure motif and the "safety belt" of HIM-3. (C) Left: schematic of HIM-3, HTP-1, HTP-2 and HTP-3 N-terminal HORMA domains and C-terminal "closure motifs." Right: alignment of putative closure motifs from all four C. elegans HORMA domain proteins. See also Figure S1B-D.

### 1.3.2 *C. elegans* meiotic HORMA domain proteins form intermolecular complexes

The identification of several putative “closure motifs” within the tail of HTP-3, together with the knowledge that HTP-3 is required for association of the other meiotic HORMA domain proteins with the axis, suggested that axis assembly might be mediated by HORMA domain:closure motif interactions. To test this idea, and to identify other components associated with the *C. elegans* meiotic chromosome axis, we purified HTP-3-containing protein complexes from a worm strain expressing a functional *htp-3-gfp* fusion (*ieSi6*). Mass spectrometry analysis of soluble HTP-3 complexes indicated that the protein physically associates with HIM-3, HTP-1, and HTP-2 (Figure 1.2A). A parallel analysis of chromosome-associated HTP-3 complexes additionally detected multiple cohesin subunits, including the meiosis-specific kleisin subunits REC-8, COH-3, and COH-4 (Figure 1.2A). These results indicate that *C. elegans* axial elements are mainly composed of cohesin complexes and the four meiotic HORMA domain proteins, consistent with prior genetic and cytological studies (Couteau and Zetka, 2005; Goodyer et al., 2008; Martinez-Perez and Villeneuve, 2005; Zetka et al., 1999).

To investigate how the four HORMA domain proteins interact with one another, we used a bacterial polycistronic expression system to co-express various combinations of the four proteins. When expressed individually, both HIM-3 and HTP-3 were soluble and monomeric in solution, as judged by size exclusion chromatography and multi-angle light scattering (SEC-MALS) (Figure 1.2B, C, S1.2). HTP-1 formed soluble aggregates when expressed on its own (not shown), but when HTP-1 was co-expressed with HIM-3 we detected soluble complexes with a stoichiometry of 1 HIM-3:1 HTP-1 (Figure 1.2B, C). Co-expression of HIM-3, HTP-1, and HTP-2 yielded a mixture of 1 HIM-3:1 HTP-1 and 1 HIM-3:1 HTP-2 complexes (not shown).

When HTP-3 was co-expressed with different combinations of HIM-3, HTP-1, and HTP-2, the resulting complexes were heterogeneous. Analysis of the composition and average molecular weights of these complexes indicated that multiple copies of the smaller HORMA domain proteins can associate simultaneously with a single HTP-3 (Figure 1.2, S1.2). Importantly, we found that HTP-1 and HIM-3 could each associate independently with HTP-3 (Figure 1.2C). Together, these results reveal that HTP-3 is able to associate simultaneously with multiple copies of HIM-3, HTP-1, and HTP-2.

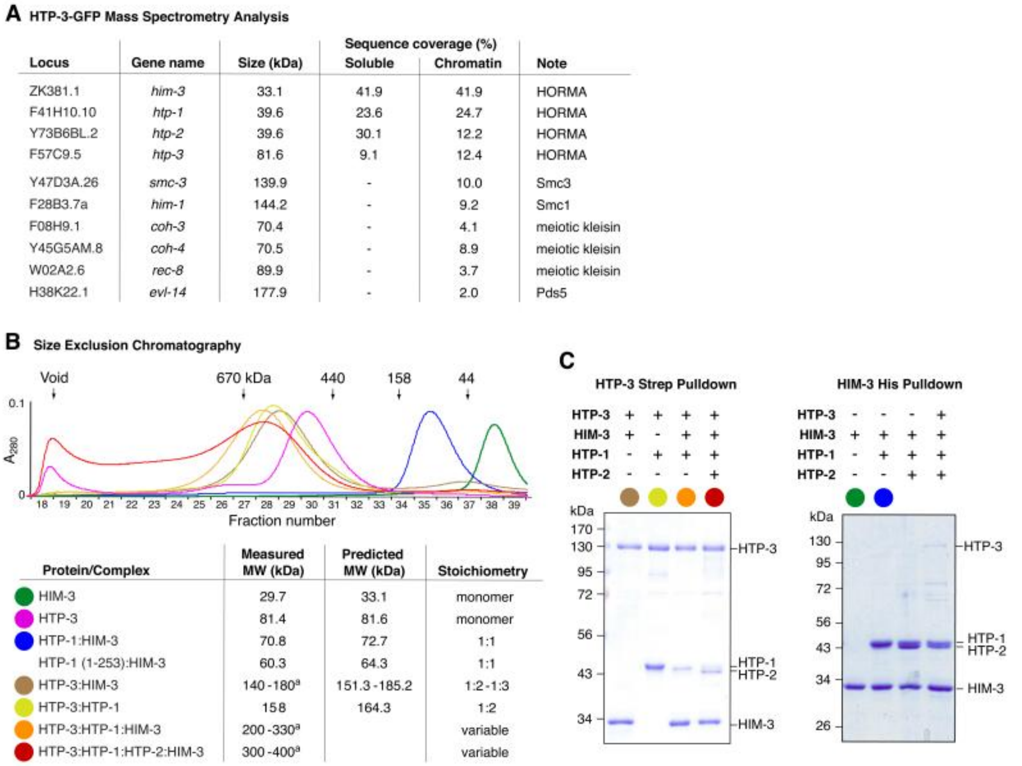

**A** HTP-3-GFP Mass Spectrometry Analysis

| Locus | Gene name | Size (kDa) | Sequence coverage (%) |  | Note |
|---|---|---|---|---|---|
|  |  |  | Soluble | Chromatin |  |
| ZK381.1 | *him-3* | 33.1 | 41.9 | 41.9 | HORMA |
| F41H10.10 | *htp-1* | 39.6 | 23.6 | 24.7 | HORMA |
| Y73B6BL.2 | *htp-2* | 39.6 | 30.1 | 12.2 | HORMA |
| F57C9.5 | *htp-3* | 81.6 | 9.1 | 12.4 | HORMA |
| Y47D3A.26 | *smc-3* | 139.9 | - | 10.0 | Smc3 |
| F28B3.7a | *him-1* | 144.2 | - | 9.2 | Smc1 |
| F08H9.1 | *coh-3* | 70.4 | - | 4.1 | meiotic kleisin |
| Y45G5AM.8 | *coh-4* | 70.5 | - | 8.9 | meiotic kleisin |
| W02A2.6 | *rec-8* | 89.9 | - | 3.7 | meiotic kleisin |
| H38K22.1 | *evl-14* | 177.9 | - | 2.0 | Pds5 |

**B** Size Exclusion Chromatography

| Protein/Complex | Measured MW (kDa) | Predicted MW (kDa) | Stoichiometry |
|---|---|---|---|
| ● HIM-3 | 29.7 | 33.1 | monomer |
| ● HTP-3 | 81.4 | 81.6 | monomer |
| ● HTP-1:HIM-3 | 70.8 | 72.7 | 1:1 |
| HTP-1 (1-253):HIM-3 | 60.3 | 64.3 | 1:1 |
| ● HTP-3:HIM-3 | 140-180[a] | 151.3-185.2 | 1:2-1:3 |
| ● HTP-3:HTP-1 | 158 | 164.3 | 1:2 |
| ● HTP-3:HTP-1:HIM-3 | 200-330[a] |  | variable |
| ● HTP-3:HTP-1:HTP-2:HIM-3 | 300-400[a] |  | variable |

**C**

## Figure 1.2 The C. elegans meiotic HORMA domain proteins form a complex

(A) Mass spectrometry results from HTP-3-GFP pulldowns. Pulldowns were performed in conditions that favored either soluble or chromatin-associated complexes (see **Extended Experimental Procedures**). (B) Size exclusion chromatography and multi-angle light scattering (SEC-MALS) analysis of HORMA domain protein complexes (a: complexes containing HTP-3 showed strong polydispersity indicative of a mixture of different-weight particles). See **Figure S2** for SDS-PAGE analysis of fractions and representative SEC-MALS results. (C) SDS-PAGE analysis of co-expressed complexes purified using Strep-HTP-3 (left panel) or HIM-3-6His (right panel).

### 1.3.3 Specific HORMA domain-closure motif interactions define a hierarchical assembly

Our reconstitution experiments showed that HIM-3, HTP-1, and HTP-2 can each bind directly to HTP-3, and that HTP-1 and HTP-2 can also independently bind HIM-3. By co-expressing truncated proteins, we further found that the HIM-3:HTP-1 interaction requires the C-terminal tail of HIM-3 (co-expression of HTP-1 with HIM-3 (1-245) did not result in a complex despite expression of both proteins; not shown), and also required the HORMA domain of HTP-1, but not its C-terminal tail. These results strongly suggest that the HIM-3-HTP-1 interaction is mediated by HORMA domain-closure motif binding *in trans* (Figure 1.2B; compare measured stoichiometry of HTP-1:HIM-3 with HTP-1 (1-253):HIM-3). Using a fluorescence polarization (FP) peptide-binding assay, we measured the affinity and specificity of HORMA domain:closure motif interactions. We found that HIM-3 binds strongly to a peptide that includes the HTP-3 motif #4 sequence ($K_d$ 0.3 µM; Figure 1.3A), and is therefore likely to also bind motifs #2, #3, and #5. However, HIM-3 did not bind a randomized version of HTP-3 motif #4, nor did it bind the divergent HTP-3 motifs #1 or #6. As full-length HIM-3 was used for this binding assay, our results show that HTP-3 motif #4 can effectively compete for binding to the HORMA domain of HIM-3 in the presence of the closure motif within HIM-3's tail. By contrast, full-length HIM-3 did not effectively bind in *trans* to the motif found within its own tail. To further characterize the selectivity of the HIM-3 HORMA domain, we co-expressed untagged HIM-3 HORMA domain (residues 1-245) in *E. coli* together with tagged closure motif peptides and measured HIM-3 association using a pulldown assay. In this assay, the HIM-3 HORMA domain bound strongly to HTP-3 motif #4, but again did not detectably bind its own closure motif (not shown). Together with results from the FP peptide-binding assay described above, this indicates that binding of the HORMA domain of HIM-3 to the closure motif within its own tail is a low-affinity interaction that depends on the high effective concentration imparted by covalent association between the HORMA domain and tail.

We next measured the binding of HTP-1 and HTP-2 to various closure motif peptides (Figure 1.3B,C). As noted above, both HTP-1 and HTP-2 form soluble aggregates when expressed in isolation, and the resulting purified proteins did not specifically bind any peptides in the FP assay (not shown). However, co-expression of $His_6$-tagged HTP-1 or HTP-2 with untagged HTP-3 resulted in a mixed population of HTP-3:HTP-1/2 complexes and free monomeric HTP-1/2, suggesting that HTP-3 may act as a chaperone for these proteins when they are co-expressed in *E. coli*. When these monomers were purified away from their respective HTP-3 complexes, both HTP-1 and HTP-2 bound strongly to the HIM-3 closure motif and to HTP-3 motifs #1 and #6, but did not associate detectably with HTP-3 motif #4 (Figure 1.3B,C). The two proteins showed similar specificities, with only subtle differences in binding affinities (Figure 1.3D).

Full-length HTP-3 did not detectably associate with either the HIM-3 or HTP-2 closure motif peptides in our peptide-binding assay (not shown). In co-expression/pulldown tests, the HTP-3 HORMA domain was also unable to interact with any of the identified closure motifs in its own C-terminus (not shown); we were unable to confirm this result through peptide binding assays due to the difficulty in purifying the truncated HTP-3 construct. Overall, these results are consistent with the idea that HTP-3 binds an as-yet-unidentified partner to mediate its localization to the meiotic chromosome axis.

Finally, none of the four proteins associated with the putative closure motif at the C-terminus of HTP-2. Notably, this motif and that of HTP-1 contain a serine in place of the highly conserved glycine in other closure motifs; our *in vitro* and *in vivo* data (see below) suggest that larger amino acid side chains at this position might interfere with binding. It is possible that the highly-conserved C-terminal motifs in HTP-1 and HTP-2 act as low-affinity closure motifs that facilitate HTP-1/2 folding or stability, but evidence supporting this idea is currently lacking. Taken together, our peptide binding assays are consistent with the knowledge that HIM-3, HTP-1, and HTP-2 require HTP-3 to associate with the meiotic chromosome axis, and suggest that that they are recruited to the axis by binding of their HORMA domains to specific closure motifs within HTP-3 and/or HIM-3 (Figure 1.3E).

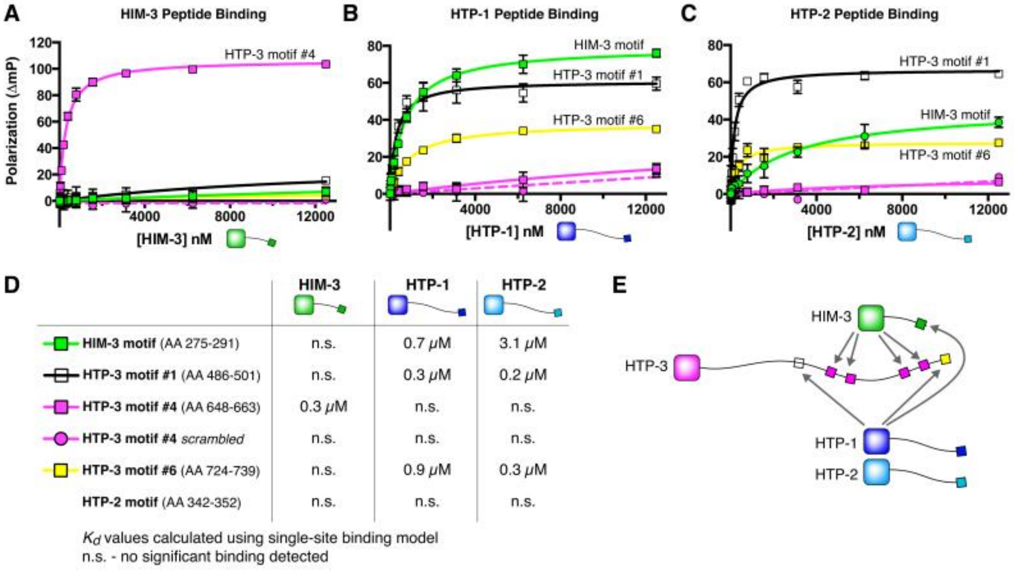

| | HIM-3 | HTP-1 | HTP-2 |
|---|---|---|---|
| 🟩 **HIM-3 motif** (AA 275-291) | n.s. | 0.7 μM | 3.1 μM |
| ☐ **HTP-3 motif #1** (AA 486-501) | n.s. | 0.3 μM | 0.2 μM |
| 🟪 **HTP-3 motif #4** (AA 648-663) | 0.3 μM | n.s. | n.s. |
| ● **HTP-3 motif #4** *scrambled* | n.s. | n.s. | n.s. |
| 🟨 **HTP-3 motif #6** (AA 724-739) | n.s. | 0.9 μM | 0.3 μM |
| **HTP-2 motif** (AA 342-352) | n.s. | n.s. | n.s. |

$K_d$ values calculated using single-site binding model
n.s. - no significant binding detected

**Figure 1.3 *C. elegans* HORMA domain proteins bind distinct closure motifs**

Fluorescence polarization (FP) peptide-binding assay for HIM-3 (A), HTP-1 (B), and HTP-2 (C). Peptides used are shown in panel (D). (D) Measured $K_d$'s for HIM-3, HTP-1, and HTP-2 binding different closure motifs. n.s.; no significant binding detected. (E) Schematic illustrating the closure motif binding specificities of HIM-3, HTP-1, and HTP-2.

### 1.3.4 Specific closure motifs within HTP-3 recruit HIM-3 to mediate homologous synapsis

To gain insight into the functional importance of the interaction between HIM-3 and HTP-3, we determined the structure of a chimeric protein in which the closure motif of HIM-3 was replaced by HTP-3 motif #4. This structure shows the HIM-3 HORMA domain in essentially the same conformation as in the native HIM-3 structure (Cα r.m.s.d. of 0.62 Å over 228 residues), and shows strong electron density for residues 649-662 of HTP-3 (Figure 1.4A, B, S1.3B) within the binding pocket. The interaction of the HIM-3 HORMA domain with HTP-3 motif #4 is much more extensive than with its own closure motif, burying 1620 Å$^2$ of total surface area versus 1150 Å$^2$ for the intramolecular binding interaction, consistent with the higher affinity measured in our peptide-binding and pull-down assays. HTP-3 residues 650-654 adopt a β-strand conformation and form a continuous β-sheet with HIM-3 β6 (within the HORMA domain) and β7 (in the “safety belt”). The tyrosine residue conserved in all closure motifs (Y651 in HTP-3 motif #4) is positioned close to the HIM-3 safety belt, and makes a hydrogen bond with asparagine 139 of HIM-3. The following residue, glycine 652, is buried against the HIM-3 HORMA domain. Arginine 653, conserved in HTP-3 motifs #2-5, makes a salt bridge with HIM-3 glutamate 115. This arginine residue is conserved in the majority of closure motifs we identified in *Caenorhabditis* HTP-3 orthologs (Figure S1.1D), and glutamate 115 is highly conserved in *Caenorhabditis* HIM-3 orthologs; this interaction may therefore represent a specific feature of HTP-3:HIM-3 complexes. The C-terminus of the closure motif (HTP-3 residues 657-662) forms an amphipathic α-helix that packs against a hydrophobic cavity in the HIM-3 HORMA domain. The hydrophobic residues in this helix are conserved within HTP-3 motifs #2-5, but in motifs #1 and #6 the corresponding side chains are charged or polar. Thus, several distinct features of HTP-3 closure motifs #2-5 contribute to HIM-3's preference for these sequences.

In all of our HORMA domain:closure motif structures, a conserved glycine near the N-terminus of the closure motif is packed tightly against a hydrophobic surface in the HORMA domain (Figure 1.4B,C). We found that mutation of this glycine to lysine in HTP-3 motif #4 (G652K) abolished binding to HIM-3 in two independent *in vitro* assays (Figure 1.4D, S1.4A). We therefore created HTP-$3^{4GK}$, in which the conserved glycine residues in the four central HTP-3 closure motifs (#2-5) were all mutated to lysine. As expected, this 4GK mutation strongly abrogated binding of HIM-3 to HTP-3 when the proteins were co-expressed in *E. coli*, but did not affect binding of HTP-1 to HTP-3 (Figure 1.4E). This result agrees with our peptide binding data, and validates the idea that HTP-3 motifs #2-5 are specific binding sites for HIM-3.

To determine the consequences of disrupting HIM-3:HTP-3 binding *in vivo*, we engineered an *htp-3-gfp* transgene with the 4GK substitutions, which was used to generate transgenic animals by Mos1-mediated single copy insertion (MosSCI) (Frøkjaer-Jensen et al., 2008) at a defined genomic locus (ttTi5605 on Chr II). Worms expressing either wild-type or 4GK mutant HTP-3-GFP were crossed to the null allele *htp-3(tm3655)*. The wild-type *htp-3-gfp* transgene supported normal chromosome axis and SC assembly dynamics (Figure 1.4F-H) and fully rescued the viability of embryos produced by homozygous animals (100% of embryos from *htp-3(tm3655) I; htp-*$3^{WT}$ *II* were viable, compared to 13% from *htp-3*(*tm3655) I*) (Figure S1.4C, D). HTP-$3^{4GK}$-GFP showed slightly lower protein expression compared to the wild-type tagged protein (Figure S1.4B), but localized properly to the chromosome axes in meiotic nuclei (Figure 1.4F). However, animals expressing HTP-$3^{4GK}$-GFP produced mostly dead eggs (only

3.1% of embryos produced by self-fertilizing *htp-3(tm3655) I; htp-3*$^{4GK}$ *II* survived to adulthood), and 27.5% of the few survivors were males (Figure 1.4F, S1.4C, D), indicating that mutation of these central four motifs leads to severe defects in meiotic chromosome segregation. Consistent with our *in vitro* data, HIM-3 failed to load onto the chromosomes in the HTP-3$^{4GK}$ mutant, while HTP-1 was still detected along the axes (Figure 1.4F). As in *him-3* mutants, chromosomes failed to pair and synapse in the HTP-3$^{4GK}$ mutant (Figure 1.4G, H). These results demonstrate that HTP-3 closure motifs #2-5 play a critical role in chromosome axis assembly and homolog synapsis through their recruitment of HIM-3 to the chromosomes. The localization of HTP-1 to the chromosomes in the HTP-3$^{4GK}$ mutant further confirms that HTP-1/HTP-2 recruitment can be mediated by direct binding to HTP-3, presumably through motifs #1 and #6, in the absence of HIM-3.

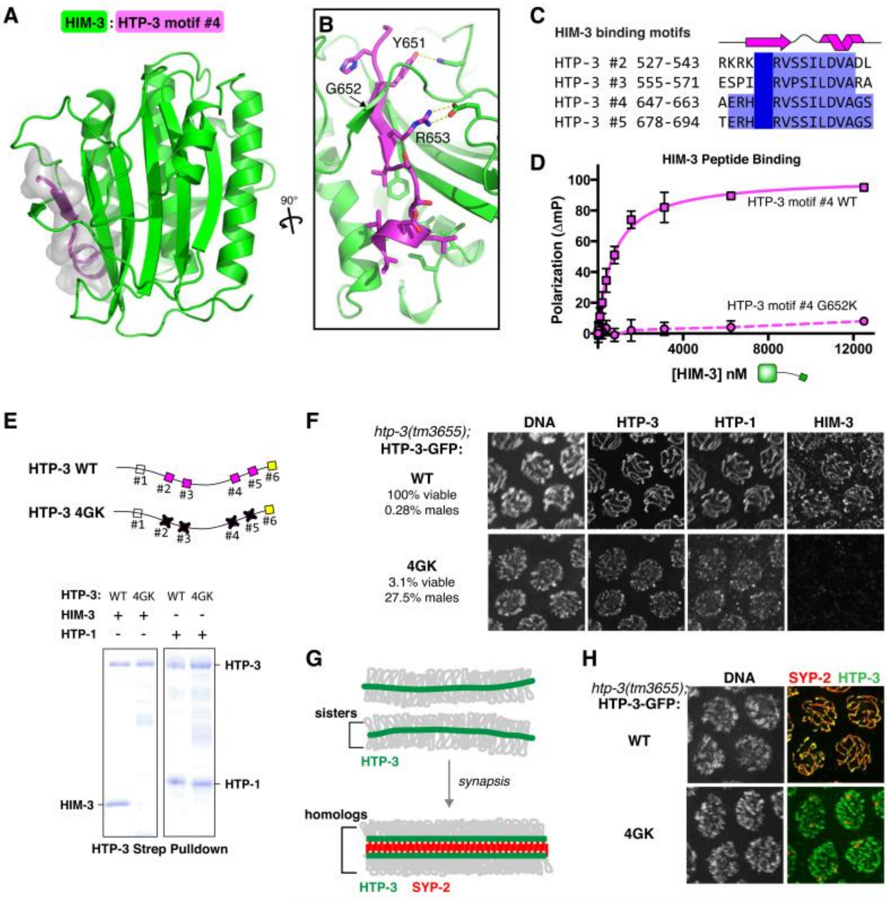

## Figure 1.4 HIM-3 binding to HTP-3 motifs #2-5 is critical for homolog synapsis and successful meiosis

(A) Structure of HIM-3 (green) bound to HTP-3 motif #4 (magenta). Molecular surface is shown in gray for the bound closure motif. (B) Detail view showing interactions between the closure motif and the "safety belt" of HIM-3. See also **Figure S3**. (C) Sequence alignment of HTP-3 motifs #2-#5. (D) FP peptide binding assay for HIM-3 binding HTP-3 motif #4 wild-type (as in **Figure 3A**) and G652K mutant. See also **Figure S4**. (E) Strep-tagged HTP-3, either wild-type or 4GK mutant (conserved glycine in HTP-3 motifs #2-#5 mutated to lysine; schematic at top), was coexpressed in *E. coli* with untagged HIM-3 (*left*) or HTP-1 (*right*), and purified using Strep-tactin resin to isolate HTP-3 and directly bound proteins. (F) Wild-type and 4GK mutant *htp-3-gfp* transgenes were expressed in the *htp-3(tm3655)I* background, and mid-pachytene nuclei stained for DNA, HTP-3:GFP, HTP-1, and HIM-3. Scale bar, 5 μm. (G) Schematic showing meiotic chromosome axis formation and synapsis. (H) Wild-type or 4GK mutant HTP-3:GFP transgenes were expressed in the *htp-3(tm3655)I* background, and mid-pachytene nuclei were stained for DNA, HTP-3:GFP (green), and SYP-2 (red). All images are maximum-intensity projections of deconvolved 3D image stacks. Scale bar, 5 μm. See also **Figure S5**.

### 1.3.5 Redundant mechanisms recruit HTP-1 and HTP-2 to the meiotic chromosome axis

The HIM-3 HORMA domain binds specifically to HTP-3 closure motifs #2-5. In contrast, HTP-1 and HTP-2 preferentially bind to HTP-3 motifs #1 and #6, and bind the HIM-3 closure motif with similarly high affinity (Figure 1.3B-D). To determine the basis for their specificity, we co-expressed and purified the HORMA domains of both HTP-1 and HTP-2 (residues 1-253 of 352) with different closure motifs. HTP-2 readily co-crystallized with the HIM-3 motif, HTP-3 motif #1, and HTP-3 motif #6, and we determined structures for each of these complexes (Figure 1.5D-G, Table 1.1). When initial crystallization screens for HTP-1:closure motif complexes failed, we examined the crystal packing interactions of HTP-2 complexes. Based on this analysis, we designed a point mutant of HTP-1 (proline 84 to leucine, P84L) to mimic a specific crystal packing interaction observed in HTP-2 structures. This residue resides on a surface-exposed α-helix (αB) and is poorly conserved among HTP-1/HTP-2 orthologs, so this mutation is unlikely to have a significant effect on HTP-1's structure or binding. Complexes containing the mutant HTP-1(1-253)$^{P84L}$ crystallized readily in conditions similar to those for HTP-2(1-253) complexes, and we determined its structure bound to both the HIM-3 closure motif and HTP-3 closure motif #1 (Figure 1.5A-C).

HTP-1 and HTP-2 share 82% sequence identity, and their HORMA domains have nearly identical crystal structures, with an overall Cα r.m.s.d of less than 0.5 Å (Figure 1.5A, D). Both are also highly similar to HIM-3 (~1.0 Å r.m.s.d between 180 aligned Cα atoms), with most of the differences in flexible loop regions. The residues that form the closure motif binding pockets within HTP-1 and HTP-2 are identical, and their modes of interaction with closure motifs are also virtually indistinguishable (e.g.

compare Figure 5B and E). The highly conserved Tyr-Gly pair within the closure motifs adopts an identical conformation in all HTP-1/2 structures, tightly engaged by strand β7 of the associated HORMA domain's "safety belt". The major difference when compared to HIM-3 is the conformation of the C-terminal portion of the bound closure motifs: while a HIM-3-bound closure motif adopts a short amphipathic α-helix (Figure 1.4B), all three motifs that bind HTP-1 and HTP-2 adopt a β-strand conformation at both ends of the motif, with a small bulge in the middle (Figure 1.5). This bulge is one residue longer in HTP-3 motif #1 than in the other two motifs, but otherwise the three motifs are bound by the HTP-1 HORMA domain in a nearly identical manner (compare Figure 1.5E with 1.5F and 1.5G; alignment in Figure 1.5H). Each of these three motifs also possesses an arginine N-terminal to the conserved Tyr-Gly pair that packs into the same negatively charged pocket on the HORMA domain, despite variation in its position within each closure motif . Other interactions in the HTP-1 and HTP-2 complexes are mostly backbone-backbone hydrogen bonds characteristic of β-sheets, providing little sequence specificity. This is reminiscent of Mad2, whose known binding peptides in Cdc20, Mad1, and Shugoshin bear only weak sequence similarity (Luo et al., 2002; Orth et al., 2011).

We next generated disruptive glycine-to-lysine mutations in HTP-3 motifs #1 and #6 (motif #1, G490K; motif #6, G728K; both, 2GK), and tested for binding by HIM-3 or HTP-1 when co-expressed in *E. coli*. None of these mutations affected HIM-3 binding (Figure 1.5I), while HTP-1 binding was clearly affected: Mutation of HTP-3 motif #1 (G490K) alone significantly reduced HTP-1 binding. Unexpectedly, mutation of motif #6 (G728K) had no detectable effect on HTP-1 binding, yet did appear to synergize with mutation of motif #1, since the HTP-3$^{2GK}$ mutant did not detectibly bind to HTP-1 (Figure 1.5I). This suggests that HTP-1 interacts more strongly with HTP-3 motif #1 than #6, consistent with results from our peptide binding assays (Figure 1.3B, C). Together with our peptide binding and structural data, these results confirm that HTP-3 motifs #1 and #6 are specific binding sites for HTP-1 and HTP-2.

We next introduced these same mutations (HTP-3 motif #1 (G490K), motif #6 (G728K), and the double mutant (2GK)) into worms by MosSCI and crossed each transgene to the *htp-3(tm3655)* null allele to test the roles of these motifs in meiotic chromosome axis assembly and synapsis. Surprisingly, all three mutant transgenes supported high levels of embryonic viability (G490K, 96.1%; G728K, 100%; 2GK, 98.6%). Consistent with this, in each of these mutants, HTP-1/2 and HIM-3 were detected at the meiotic chromosome axis (Figure 1.5J, S1.5A), and robust homologous synapsis was observed, albeit with a modest delay in animals expressing HTP-3$^{G490K}$ or HTP-3$^{2GK}$ (Figure 1.5K, S1.5B, C). Because the double mutant (HTP-3$^{2GK}$) protein failed to bind HTP-1 *in vitro* (Figure 1.5I), we reasoned that axis localization in this mutant is likely mediated through binding of HTP-1/2 to HIM-3, which in turn is recruited by HTP-3. Consistent with this, when HTP-3$^{2GK}$ was crossed into the *him-3(gk149)* null background, HTP-1/2 was drastically reduced on meiotic chromosomes, and chromosome synapsis was eliminated (Figure 1.5J, K). Similar results were observed when all six closure motifs within HTP-3 were mutated (HTP-3$^{6GK}$), which eliminated recruitment of HIM-3, HTP-1, and HTP-2 (Figure 1.5J, K). Notably, we found that animals expressing a truncated HIM-3 protein lacking the closure motif (residues 1-245) were proficient to recruit HTP-1/2 to the chromosome axis and showed no meiotic nondisjunction (Figure S1.5A). Taken together, these results indicate that HTP-1/2 can be recruited to the axis by binding to HTP-3 motifs #1 and #6, or by binding to the closure motif within HIM-3, and that either mode of HTP-1/2 recruitment is sufficient to support homologous synapsis and meiotic chromosome segregation.

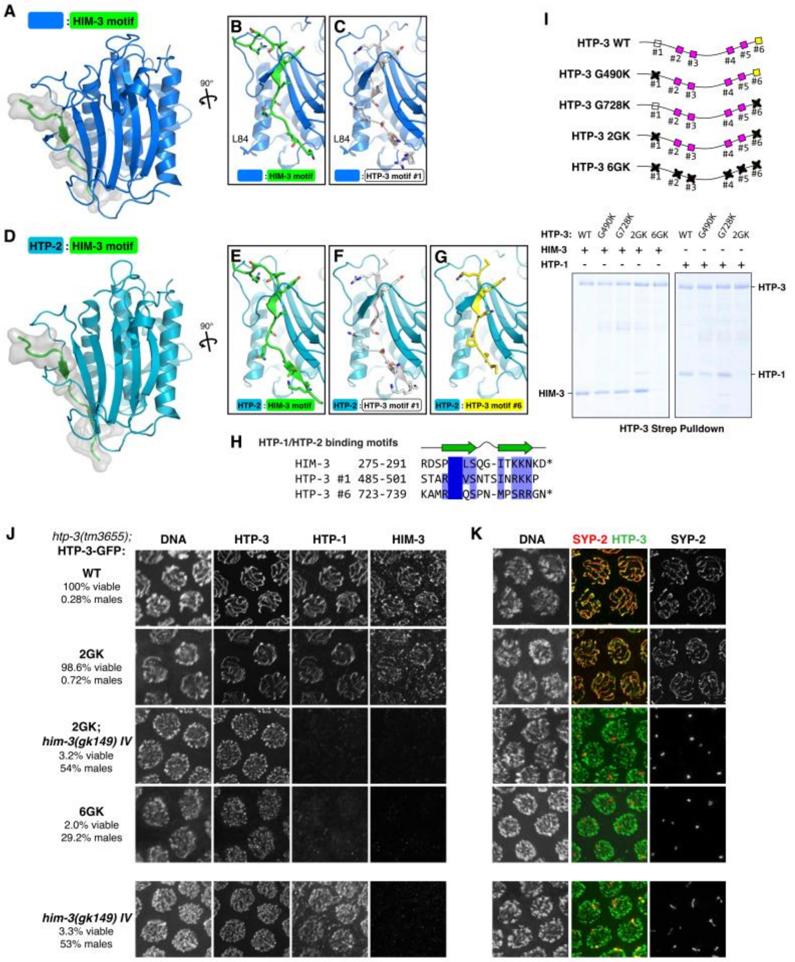

**Figure 1.5 HTP-1/HTP-2 is recruited to chromosomes by both HTP-3 and HIM-3.**

(A) Structure of HTP-1$^{P84L}$ (blue) bound to the HIM-3 closure motif (green). A molecular surface representation is shown in gray for the bound closure motif. (B-C) Detail views showing interactions between HTP-1$^{P84L}$ and the HIM-3 closure motif (B) or HTP-3 motif #1 (C). Leucine 84 is shown in stick view. See **Figure S3** for representative electron density. (D) Structure of HTP-2 (cyan) bound to the HIM-3 closure motif (green). (E-G) Detail views showing interactions between HTP-2 and the HIM-3 closure motif (E), HTP-3 motif #1 (F), or HTP-3 motif #6 (G). (H) Sequence alignment of closure motifs specific for binding the HTP-1 and HTP-2 HORMA domains. (I) Strep-tagged HTP-3 wild-type or GK mutants (schematic at top) were coexpressed in *E. coli* with untagged HIM-3 (*left*) or HTP-1 (*right*), and purified using Strep-tactin resin to isolate HTP-3 and directly bound proteins. (J) Wild-type, 2GK, and 6GK mutant *htp-3-gfp* transgenes were expressed in the *htp-3(tm3655)I* background and combined with the *him-3(gk149) IV* null allele, and mid-pachytene nuclei stained for DNA, HTP-3:GFP, HTP-1, and HIM-3. Scale bar, 5 µm. (K) Projection images showing mid-pachytene nuclei of the strains in (J) stained for DNA, HTP-3:GFP (green), and SYP-2 (red). Scale bar, 5 µm. See also **Figure S5**.

### 1.3.6 HTP-3 promotes chromosome cohesion and DSB formation, independent of HIM-3 and HTP-1/HTP-2 recruitment to the meiotic chromosome axis

In addition to promoting homolog pairing and synapsis and double-strand break formation, HTP-3 is required to maintain sister chromatid cohesion until meiosis II (Severson et al., 2009). Our evidence that HTP-3 recruits the other HORMA domain proteins to the axis through motifs in its C-terminal tail enabled us to test whether these roles of HTP-3 require the other HORMA domain proteins. To determine how HTP-3 contributes to cohesion, we compared cohesin loading in *htp-3* null mutants vs. animals expressing the engineered HTP-$3^{6GK}$ variant, which shows normal axis association but fails to recruit HIM-3 and HTP-1/2. In wild-type animals, cohesin complexes containing the common SMC subunits SMC-1 and SMC-3, but with distinct kleisin subunits (REC-8 or COH-3/COH-4), localize along meiotic chromosome axes from meiotic entry through late pachytene (Pasierbek et al., 2001; Severson et al., 2009). While SMC-1, SMC-3 and COH-3/COH-4 were detected on chromosomes in two *htp-3* null mutants (*tm3655* and *y428*; data not shown for *y428*) (Figure 1.6B, S1.6A, B), REC-8 staining was greatly diminished (Figure 1.6A), as previously reported (Severson et al., 2009). By contrast, REC-8 was clearly retained on meiotic chromosomes in HTP-$3^{6GK}$ mutants (Figure 1.6A). These results indicate that HTP-3 promotes sister chromatid cohesion through loading and/or maintenance of REC-8, but not COH-3/COH-4, and that the requirement for HTP-3 in REC-8 loading is independent of its role in recruiting HIM-3 or HTP-1/HTP-2 to the axis.

Previous work has indicated that HTP-3 is required for the formation of meiotic DSBs (Goodyer et al., 2008). Thus we examined DSB formation in HTP-$3^{6GK}$ mutants by staining for RAD-51, a DNA strand exchange protein that marks recombination intermediates (Colaiácovo et al., 2003; Sung, 1994). While most germline nuclei in *htp-3* null animals lacked RAD-51 foci, consistent with prior work, RAD-51 foci appeared and disappeared with normal kinetics in HTP-$3^{6GK}$ animals despite the absence of pairing, synapsis, or crossover formation (Figure 1.6C, S1.6C). These results indicate that HTP-3's role in DSB formation and/or processing, which has been proposed to involve a direct interaction with the Rad50/Mre11 complex (Goodyer et al., 2008), is also independent of its recruitment of HIM-3 and HTP-1/HTP-2 (Figure 1.6D). The timely disappearance of RAD-51 foci suggests that axial association of HTP-3 is insufficient to pose a barrier to intersister recombination, consistent with previous evidence that HIM-3 and HTP-1 are required for this barrier in *C. elegans* (Couteau and Zetka, 2005; Couteau et al., 2004).

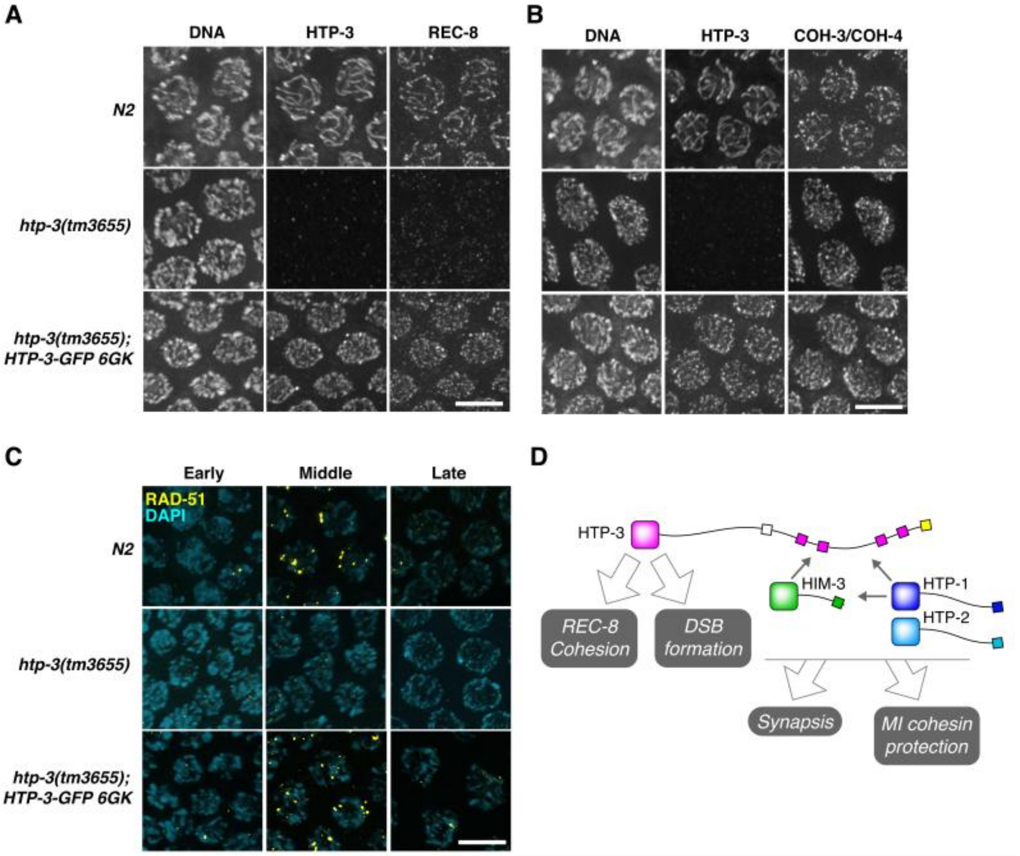

## Figure 1.6 Chromosome axis localization of cohesin complexes in HTP-3 closure motif GK mutants.

(A) and (B) Mid-pachytene nuclei in wild-type *N2*, *htp-3*(*tm3655*), and *htp-3(tm3655);htp-*$3^{6GK}$ worms were stained for HTP-3 and meiosis-specific kleisin subunits of the cohesin complex, REC-8 (A) or COH-3/COH-4 (B). Scale bar, 5 μm. See **Figure S6** for localization of SMC subunits SMC-1 and SMC-3. (C) Projection images showing mid-pachytene nuclei stained for DNA and RAD-51 to assess the formation and repair of meiotic DSBs. (D) Schematic illustrating the major functions and proposed roles of the *C. elegans* meiotic HORMA domain proteins.

### 1.3.7 Meiotic HORMA domain:closure motif interactions are a conserved feature of axis organization

In mouse spermatocytes and oocytes, two meiosis-specific HORMA domain proteins, HORMAD1 and HORMAD2, co-localize on the chromosome axis (Wojtasz et al., 2009). These proteins also physically interact both *in vivo* and *in vitro* (Wojtasz et al., 2012). Like the four *C. elegans* proteins analyzed here, these mammalian proteins contain a HORMA domain followed by a C-terminal tail predicted to lack inherent structure. The tails of mammalian HORMAD1 and HORMAD2 orthologs are highly conserved along their entire lengths, making it impossible to identify putative closure motifs from sequence alone. However, when we compared HORMAD1 to HORMAD2, we noticed two short regions of homology within their tails, including one at their extreme C-termini (Figure 1.7A), suggesting that this region might mediate protein-protein interactions.

To determine whether HORMAD1 and HORMAD2 might interact in a manner similar to the *C. elegans* HORMA domain proteins, we purified the HORMA domain (residues 2-235 of 394) from human HORMAD1, expressed in *E. coli*. Separately, we expressed and purified the C-terminal tails of HORMAD1 (residues 236-394) and HORMAD2 (residues 245-307), each fused to an N-terminal $His_6$-maltose binding protein (MBP) tag. In a $Ni^{2+}$ pulldown assay, we found that both full-length tails strongly interacted with HORMAD1(2-235) (Figure 1.7B, C), suggesting that each tail contains a peptide that can act as a HORMAD1 closure motif. By expressing and purifying tail fragments, we mapped this binding activity to the conserved region at these proteins' C-termini (residues 375-394 of HORMAD1 and 283-307 of HORMAD2). Thus, human HORMAD1 binds a putative closure motif present in the C-terminal tails of both

HORMAD1 and HORMAD2 (Figure 1.7D), indicating that the HORMA domain-tail interactions we have identified in *C. elegans* are conserved in mammals. It is likely that some details of these interactions differ among lineages, given the variable number of meiotic HORMA proteins and our evidence that mammalian HORMAD1 can bind either its own C-terminus or that of HORMAD2, in contrast to the hierarchical interactions we have documented for the *C. elegans* protein family.

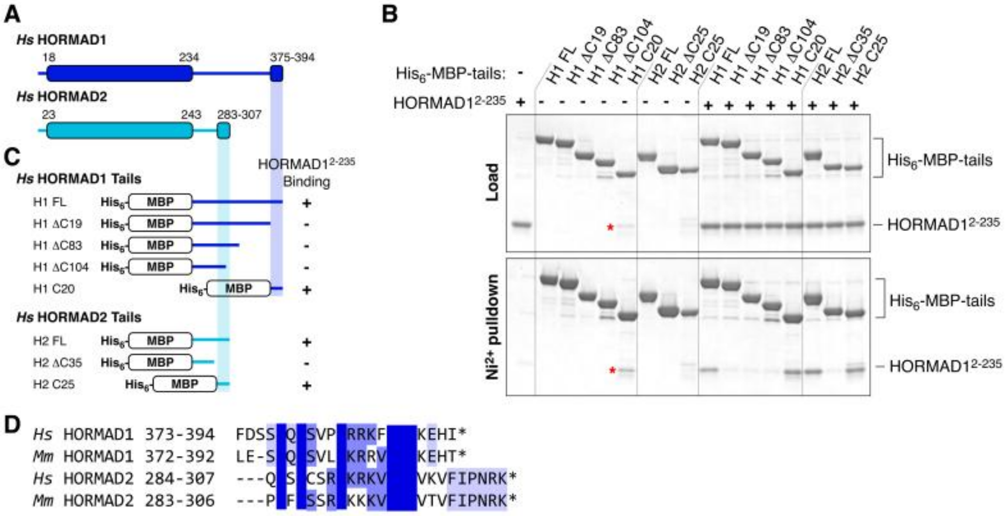

**Figure 1.7 Mammalian HORMAD1 and HORMAD2 contain C-terminal closure motifs.**

Schematic of human HORMAD1 and HORMAD2, with HORMA domain and C-terminal region shown as boxes. (B) Ni$^{2+}$ pulldown using $His_6$-MBP-tagged HORMAD1/2 tail segments, with untagged human HORMAD1(2-235) as prey. *Top panel*: 10% Load sample, *Bottom panel*: Ni$^{2+}$-bound fraction. Red asterisks (*) indicate a contaminant in the HORMAD1 ΔC104 tail construct that is of similar molecular weight to HORMAD1(2-235). (C) Schematic of results from (B), showing that the extreme C-terminal regions of both HORMAD1 and HORMAD2 are necessary and sufficient for HORMAD1(2-235) binding. (D) Sequence alignment of putative HORMAD1 and HORMAD2 closure motifs from human (*Hs*) and mouse (*Mm*).

## 1.4 Discussion

Here we report a combined structural and biochemical characterization of the *C. elegans* meiotic HORMA domain proteins, revealing a new mode of interaction at the meiotic chromosome axis. When compared to the well-characterized Mad2 HORMA domain protein, our structures of HIM-3, HTP-1, and HTP-2 show that these proteins adopt a “closed” conformation, with the extended β5-αC loop draping over strands β8′ and β8″ and likely stabilizing the closed state. It is unknown whether the meiotic HORMA domain proteins readily interconvert between “open” and “closed” conformations, as observed for Mad2 (Luo et al., 2000; Sironi et al., 2002). However, we have found that *in vitro*, HIM-3 can bind an HTP-3 closure motif flanked on both ends by a large globular domain, precluding the possibility of this motif “threading” into its binding site (not shown); moreover, HTP-3 tagged at its C-terminus with the globular GFP can function in lieu of wild-type HTP-3 *in vivo*. These observations indicate that HIM-3 and HTP-1/2 must undergo major conformational changes during closure motif binding/exchange. The nature of these changes, as well as their effects on other potential protein-protein interactions within the axis, remain important unanswered questions.

It is highly likely that meiotic HORMA domain proteins engage in additional interactions beyond the HORMA domain:closure motif binding mechanisms we have characterized here. Prior work on Mad2 and Rev7 has shown that the HORMA domain is capable of multiple simultaneous protein-protein interactions, including homodimerization (Hara et al., 2009; Mapelli et al., 2007) and binding of partner proteins along the surface of the extended β-sheet (Kikuchi et al., 2012). Defining the nature of the conformational changes involved in binding/exchange of closure motifs, as well as characterizing interactions with additional potential partners such as cohesins, LAB-1 (de Carvalho et al., 2008), Mre11 (Goodyer et al., 2008), signaling effectors, and/or synaptonemal complex components, will be critical for understanding the central roles played by HORMA domain proteins along meiotic chromosomes. Additionally, identification of effectors specific to HIM-3 or HTP-1/HTP-2 may help explain why these structurally very similar proteins nonetheless play distinct roles at the meiotic chromosome axis.

Meiotic chromosome axis assembly and disassembly are tightly regulated. HORMA domain proteins are detected in the nucleoplasm of proliferating germline nuclei but do not localize to chromosomes, suggesting that their interactions are triggered upon meiotic entry (Burger et al., 2013). Late in meiotic prophase, an early indication of chromosome remodeling and SC disassembly is the restriction of HTP-1/2 to the “long arm” of the chromosomes, while HTP-3 and HIM-3 persist along both arms (Martinez-Perez et al., 2008). We have shown that HTP-1 and HTP-2 can associate with the chromosome axis in two ways: through direct binding to closure motifs in HTP-3 (#1 or #6) or by binding to HIM-3. Our evidence that the two proteins display distinct binding affinities for these different motifs suggests that there may be differentially regulated pools of HTP-1 and HTP-2 at the chromosome axis. In addition, all of the identified closure motifs contain tyrosine, threonine, and/or serine residues, which may be targets for post-translational modification. Some of these residues lie within consensus phosphorylation motifs for Polo-like or Aurora B kinases, which have been implicated in SC disassembly and regulation of meiotic cohesion in *C. elegans* (Harper et al., 2011; Rogers et al., 2002). We therefore think it likely that dynamic interactions among the

HORMA domain proteins are regulated by phosphorylation or other posttranslational modifications within the closure motifs.

An important question for the future is how HTP-3 is recruited to meiotic chromosomes, and whether this recruitment is mediated by interaction of HTP-3's HORMA domain with a closure motif. Our mass spectrometry analysis of chromosome-associated proteins demonstrates that HTP-3 associates with cohesins, suggesting that HTP-3 may bind directly to a cohesin subunit. This hypothesis is consistent with the earlier findings that cohesin complexes are required for HTP-3 recruitment to meiotic chromosomes (Goodyer et al., 2008; Severson et al., 2009). In addition, our evidence demonstrates that the majority of cohesin subunits (most likely COH-3/COH-4-containing cohesin complexes) can associate with chromosomes independently of HTP-3 (Figure 1.6, S1.6). Thus, we speculate that cohesins provide a foundation for HTP-3 loading and organization of the meiotic chromosome axis, possibly through HORMA domain-closure motif interactions. Clear functional links between the HORMA domain proteins and cohesin complexes are also observed in other eukaryotes (Klein et al., 1999; Llano et al., 2012; Winters et al., 2014) including mammals, where meiotic chromosome axis structure is disrupted in cohesin mutants (Winters et al., 2014). We therefore propose that HORMA domain proteins may be recruited to the chromosome axis through direct interactions with cohesin subunits in diverse eukaryotic lineages.

How widespread is the hierarchical assembly of HORMA domain proteins that we have outlined in *C. elegans*? The conservation of HIM-3, HTP-1, HTP-2, and HTP-3 orthologs throughout the *Caenorhabditis* genus indicates that the hierarchical assembly mechanism is likely similar within this group, while the variable numbers of closure motifs in HTP-3 orthologs (Figure S1D) may represent lineage-specific optimization of the concentration of HORMA domain proteins along the chromosome axis. Mammals and plants possess two meiotic HORMA domain proteins (HORMAD1/2 and ASY1/2, respectively), while most fungi express only one (Hop1). Our *in vitro* binding results indicate that the HORMA domain-closure motif interactions are conserved in mammals. The apparent lack of specificity/directionality of this interaction suggests that, in mammals, HORMAD1 and HORMAD2 may assemble into a less well-defined hierarchical complex than in *C. elegans*. The highly specific architecture of the *C. elegans* complex may be related to the expansion of this protein family in nematodes, and their additional roles in regulating meiotic cohesion on these organisms' holocentric chromosomes.

While only a single meiotic HORMA domain protein, Hop1, is expressed in most fungi, this protein may nonetheless engage in similar HORMA domain:closure motif interactions. In *Saccharomyces cerevisiae*, initial recruitment of Hop1 to the meiotic chromosome axis requires its binding partner Red1, but Hop1 function also depends on a short, highly conserved motif at its extreme C-terminus. Disruption of this C-terminal motif by insertions (Friedman et al., 1994) or missense mutations (Niu et al., 2005) strongly affects Hop1 localization and spore viability, and existing evidence is consistent with the idea that it functions as a closure motif. We therefore speculate that Hop1 may be recruited to the axis through multiple mechanisms (*e.g.*, direct binding to DNA, cohesins, and/or Red1, as well as other Hop1 molecules). A hierarchical network of HORMA domain proteins, mediated in part by HORMA domain-closure motif interactions, is likely to be a prominent structural feature of the meiotic chromosome axis throughout eukaryotes.

## 1.5 Experimental Procedures

For full experimental details, see Supplementary Material.

### 1.5.1 Mass Spectrometry Analysis

*C. elegans* expressing *htp-3-gfp* (*ieSi6*) were synchronized by bleaching and grown in liquid culture at 20°C until worms reached the young adult stage. Animals were harvested by sucrose flotation, frozen, and disrupted using a mixer mill. HTP-3 complexes (soluble or chromatin-associated) were purified using a GFP-binding protein (Rothbauer et al., 2008). Trypsin-digested samples were analyzed for protein identification by MudPIT (Washburn et al., 2001). To enrich for chromatin-associated proteins, worms were incubated in hypotonic buffer and then homogenized in a dounce homogenizer, then spun at low speed to separate nuclei from cell debris, further purified over a sucrose cushion, then treated with micrococcal nuclease to digest chromatin prior to immunoprecipitation as above.

### 1.5.2 In vitro reconstitution and peptide binding

ORFs were amplified from a cDNA library and cloned into *E. coli* expression vectors fused to $His_6$-, $His_6$-maltose binding protein (MBP), or Strep-tag II sequences (*in vitro* reconstitution). Expressed proteins were purified from bacterial lysates using affinity ($Ni^{2+}$ or Strep), ion-exchange, and size-exclusion chromatography. For crystallization, proteins were concentrated and stored at 4°C, and for biochemical experiments, proteins were aliquoted and frozen at -80°C. Purified samples were characterized by size-exclusion chromatography (Superose 6, GE Life Sciences) and multi-angle light scattering (Wyatt Technologies mini-DAWN Treos) to determine molecular weight and complex stoichiometry. FITC-labeled peptides (BioMatik) at 50 nM were incubated with 12 nM-12.5 μM HORMA protein, fluorescence polarization was read using a TECAN Infinite M1000 PRO fluorescence plate reader, and binding data were analyzed with Graphpad Prism v. 6 using a single-site binding model. For $Ni^{2+}$ pulldown assays, human HORMAD1 was purified as above, and HORMAD1/2 tail sequences were fused to $His_6$-MBP and purified. Proteins were mixed, then bound to Ni-NTA beads (Qiagen), washed, and bound proteins were visualized by SDS-PAGE.

### 1.5.3 Crystallization and Structure Solution

Wild-type HIM-3 was purified as above, crystals were grown and cryoprotected in sodium malonate, and the structure was determined using a 2.0 Å resolution single-wavelength anomalous (SAD) selenomethionine dataset. For crystallization of HIM-3 bound to HTP-3 closure motif #4, residues 277-289 of HIM-3 were replaced by residues 649-663 of HTP-3. For crystallization of HTP-2 complexes, HTP-2 residues 1-253 was co-expressed with a closure motif fused to a TEV protease-cleavable $His_6$-MBP tag, and complexes purified as above. For crystallization of HTP-1 complexes, HTP-1 residues 1-253, with proline 84 mutated to leucine, was co-expressed with closure motifs as for HTP-2. All HTP-1/HTP-2:closure motif complexes were crystallized and cryoprotected in polyethylene glycol, and structures were solved by SAD or molecular replacement (Table 1).

### 1.5.4 C. elegans Strains and Immunofluorescence

Strains carrying wild-type, mutant *htp-3-gfp*, and a truncated *him-3* (residues 1-245) transgenes were generated by MosSCI (Frøkjaer-Jensen et al., 2008). Homozygous insertions at the ttTi5605 locus (Chr II) were verified by PCR, and crossed into *htp-3(tm3655)* or *him-3(gk149)* to examine the loading of HORMA domain proteins, cohesin loading and synapsis. Immunofluorescence of dissected gonads was performed as previously described (Phillips et al., 2009).

## 1.6 Supplemental Data

| **Data collection** | **HIM-3 (SeMet)** | **HIM-3 Native** | **HIM-3: HTP-3 motif #4** | **HTP-2:HIM-3 motif $P2_12_12_1$ SeMet** | **HTP-2:HIM-3 motif $P2_12_12_1$ Native** |
|---|---|---|---|---|---|
| Synchtrotron/Beamline | APS 24ID-E | APS 24ID-E | SSRL 12-2 | ALS 8.2.1 | SSRL 12-2 |
| Resolution (Å) | 50.0 – 2.00 | 50.0 – 1.75 | 40 – 2.85 | 50 – 3.4 | 40 – 2.55 |
| Wavelength (Å) | 0.979 | 0.979 | 0.979 | 0.979 | 0.979 |
| Space Group | $P6_1$ | $P6_1$ | R32 | $P2_12_12_1$ | $P2_12_12_1$ |
| Unit Cell Dimensions (a, b, c) Å | 73.19, 73.19, 110.44 | 73.14, 73.14, 110.45 | 161.791, 161.79, 110.55 | 66.80, 81.84, 118.79 | 66.23, 82.67, 118.70 |
| Unit cell Angles ($\alpha,\beta,\gamma$) ° | 90, 90, 120 | 90, 90, 120 | 90, 90, 120 | 90, 90, 90 | 90, 90, 90 |
| $I/\sigma$ (last shell) | 17.3 (2.4) | 13.2 (1.4) | 20.1 (1.4) | 7.9 (2.0) | 15.8 (1.4) |
| $^1R_{sym}$ (last shell) | 0.092 (0.726) | 0.123 (1.457) | 0.057 (1.361) | 0.176 (0.779) | 0.087 (1.631) |
| $^2R_{meas}$ (last shell) | 0.131 (0.865) | 0.133 (1.571) | 0.062 (1.469) | 0.214 (0.951) | 0.095 (1.769) |
| $^3CC_{1/2}$, last shell | 0.738 | 0.454 | 0.656 | 0.628 | 0.745 |
| Completeness (last shell) % | 100.0 (99.9) | 100.0 (99.9) | 95.7 (96.5) | 95.9 (96.7) | 99.0 (98.2) |
| Number of reflections | 167813 | 254169 | 87887 | 49601 | 143932 |
| *unique* | 22367 | 33729 | 12444 | 16424 | 21690 |
| Multiplicity (last shell) | 7.5 (6.9) | 7.5 (7.2) | 7.1 (7.2) | 3.0 (3.0) | 6.6 (6.6) |
| Number of sites | 5 | - | - | 12 | - |
| **Refinement** | | | | | |
| Resolution (Å) | | 50.0 – 1.75 | 50 – 2.85 | | 40 – 2.55 |
| No. of reflections | | 33673 | 12376 | | 21562 |
| *working* | | 31968 | 11796 | | 20479 |
| *free* | | 1705 | 580 | | 1083 |
| $^4R_{work}$ (last shell) (%) | | 15.82 (30.07) | 17.79 (29.68) | | 22.85 (45.59) |
| $^4R_{free}$ (last shell) (%) | | 18.53 (37.95) | 22.99 (31.88) | | 26.42 (44.67) |
| **Structure/Stereochemistry** | | | | | |
| No. of atoms | | 4121 *(note 6)* | 1923 | | 3932 |
| *solvent* | | 287 | 0 | | 18 |
| r.m.s.d. bond lengths (Å) | | 0.011 | 0.004 | | 0.004 |
| r.m.s.d. bond angles (°) | | 1.224 | 0.839 | | 0.771 |
| Protein Data Bank ID[5] | N/A | 4TRK | *awaiting code* | N/A | *awaiting code* |

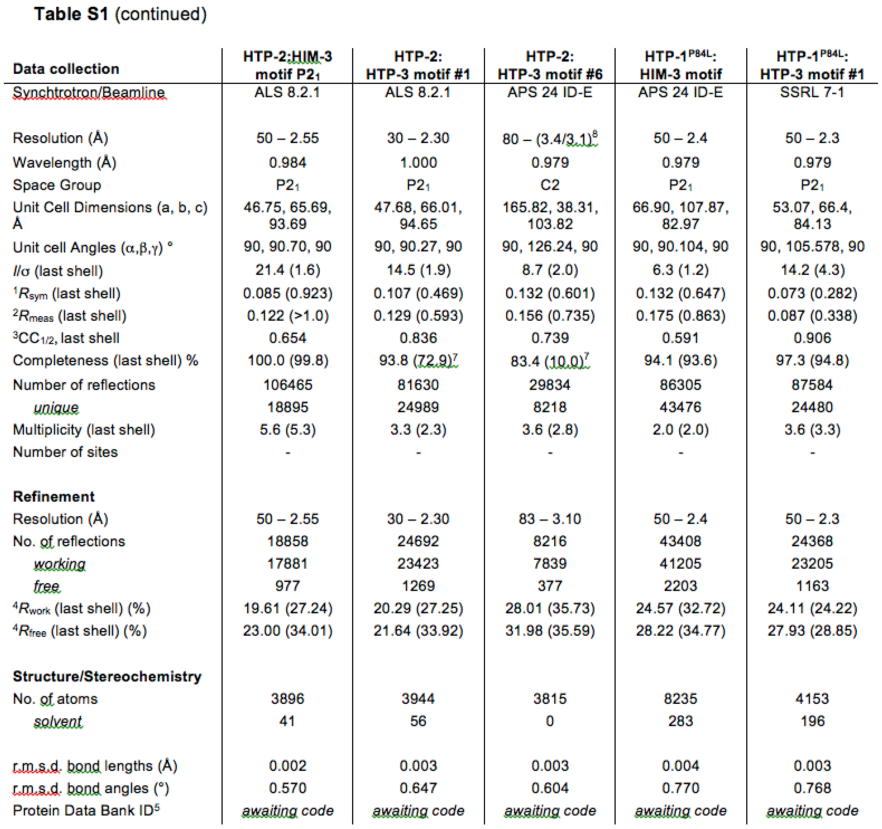

**Table S1** (continued)

| **Data collection** | **HTP-2:HIM-3 motif $P2_1$** | **HTP-2: HTP-3 motif #1** | **HTP-2: HTP-3 motif #6** | **HTP-1$^{P84L}$: HIM-3 motif** | **HTP-1$^{P84L}$: HTP-3 motif #1** |
|---|---|---|---|---|---|
| Synchrotron/Beamline | ALS 8.2.1 | ALS 8.2.1 | APS 24 ID-E | APS 24 ID-E | SSRL 7-1 |
| | | | | | |
| Resolution (Å) | 50 – 2.55 | 30 – 2.30 | 80 – (3.4/3.1)$^8$ | 50 – 2.4 | 50 – 2.3 |
| Wavelength (Å) | 0.984 | 1.000 | 0.979 | 0.979 | 0.979 |
| Space Group | $P2_1$ | $P2_1$ | C2 | $P2_1$ | $P2_1$ |
| Unit Cell Dimensions (a, b, c) Å | 46.75, 65.69, 93.69 | 47.68, 66.01, 94.65 | 165.82, 38.31, 103.82 | 66.90, 107.87, 82.97 | 53.07, 66.4, 84.13 |
| Unit cell Angles ($\alpha,\beta,\gamma$) ° | 90, 90.70, 90 | 90, 90.27, 90 | 90, 126.24, 90 | 90, 90.104, 90 | 90, 105.578, 90 |
| $I/\sigma$ (last shell) | 21.4 (1.6) | 14.5 (1.9) | 8.7 (2.0) | 6.3 (1.2) | 14.2 (4.3) |
| $^1R_{sym}$ (last shell) | 0.085 (0.923) | 0.107 (0.469) | 0.132 (0.601) | 0.132 (0.647) | 0.073 (0.282) |
| $^2R_{meas}$ (last shell) | 0.122 (>1.0) | 0.129 (0.593) | 0.156 (0.735) | 0.175 (0.863) | 0.087 (0.338) |
| $^3CC_{1/2}$, last shell | 0.654 | 0.836 | 0.739 | 0.591 | 0.906 |
| Completeness (last shell) % | 100.0 (99.8) | 93.8 (72.9)$^7$ | 83.4 (10.0)$^7$ | 94.1 (93.6) | 97.3 (94.8) |
| Number of reflections | 106465 | 81630 | 29834 | 86305 | 87584 |
| *unique* | 18895 | 24989 | 8218 | 43476 | 24480 |
| Multiplicity (last shell) | 5.6 (5.3) | 3.3 (2.3) | 3.6 (2.8) | 2.0 (2.0) | 3.6 (3.3) |
| Number of sites | - | - | - | - | - |
| | | | | | |
| **Refinement** | | | | | |
| Resolution (Å) | 50 – 2.55 | 30 – 2.30 | 83 – 3.10 | 50 – 2.4 | 50 – 2.3 |
| No. of reflections | 18858 | 24692 | 8216 | 43408 | 24368 |
| *working* | 17881 | 23423 | 7839 | 41205 | 23205 |
| *free* | 977 | 1269 | 377 | 2203 | 1163 |
| $^4R_{work}$ (last shell) (%) | 19.61 (27.24) | 20.29 (27.25) | 28.01 (35.73) | 24.57 (32.72) | 24.11 (24.22) |
| $^4R_{free}$ (last shell) (%) | 23.00 (34.01) | 21.64 (33.92) | 31.98 (35.59) | 28.22 (34.77) | 27.93 (28.85) |
| | | | | | |
| **Structure/Stereochemistry** | | | | | |
| No. of atoms | 3896 | 3944 | 3815 | 8235 | 4153 |
| *solvent* | 41 | 56 | 0 | 283 | 196 |
| | | | | | |
| r.m.s.d. bond lengths (Å) | 0.002 | 0.003 | 0.003 | 0.004 | 0.003 |
| r.m.s.d. bond angles (°) | 0.570 | 0.647 | 0.604 | 0.770 | 0.768 |
| Protein Data Bank ID$^5$ | *awaiting code* | *awaiting code* | *awaiting code* | *awaiting code* | *awaiting code* |

**Table S1.1: (related to Figures 1.1, 1.4, and 1.5) – Data Collection and Refinement Statistics**

[1] $R_{sym} = \sum\sum_j |I_j - \langle I \rangle| / \sum I_j$, where $I_j$ is the intensity measurement for reflection j and $\langle I \rangle$ is the mean intensity for multiply recorded reflections.

[2] $R_{meas} = \sum_h [\sqrt{(n/(n-1))} \sum_j [I_{hj} - \langle I_h \rangle] / \sum_{hj} \langle I_h \rangle$
where $I_{hj}$ is a single intensity measurement for reflection h, $\langle I_h \rangle$ is the average intensity measurement for multiply recorded reflections, and $n$ is the number of observations of reflection h.

[3] $CC_{1/2}$ is the Pearson correlation coefficient between the average measured intensities of two randomly-assigned half-sets of the measurements of each unique reflection (Karplus and Diederichs, 2012). $CC_{1/2}$ is considered significant above a value of ~0.15.

[4] $R_{work, free} = \sum||F_{obs}| - |F_{calc}||/|F_{obs}|$, where the working and free $R$-factors are calculated using the working and free reflection sets, respectively.

[5] Coordinates and structure factors for each structure have been deposited with the Protein Data Bank (http://www.pdb.org) with the noted accession codes.

[6] Model was refined with 1906 explicitly modeled hydrogen atoms (added to protein only)

[7] Data were highly anisotropic, leading to systematic data incompleteness.

[8] Data were scaled using anisotropic resolution cutoffs; 3.4 Å along the a and c axes, 3.1 Å along the b axis.

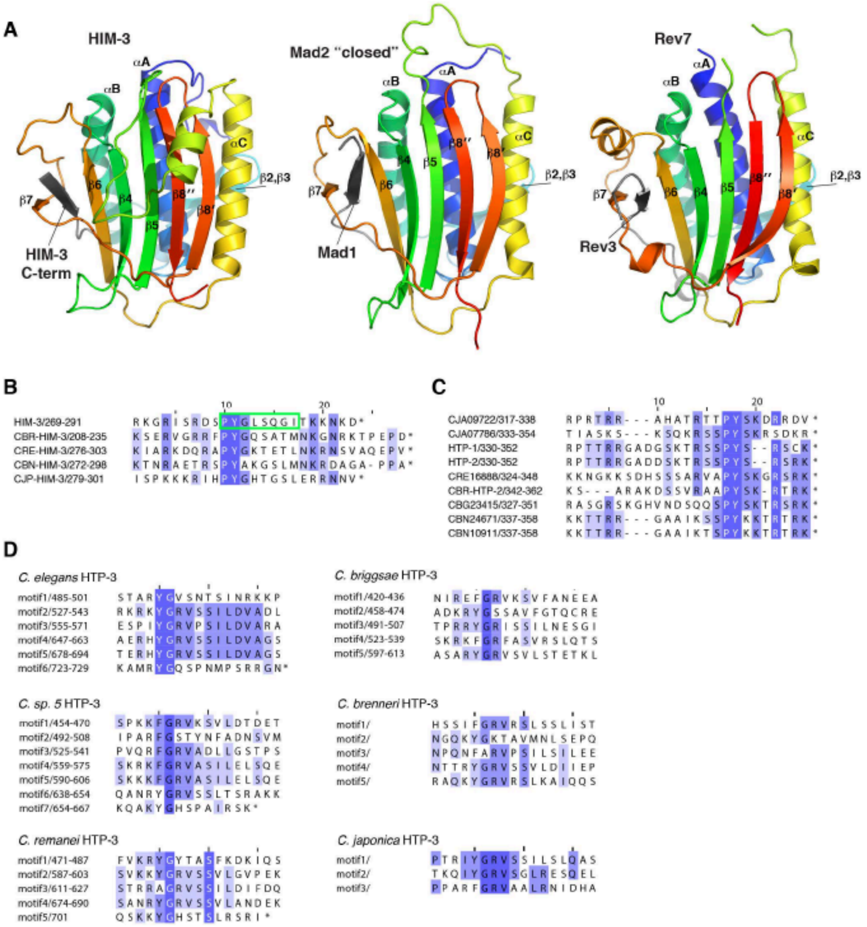

**Figure S1.1 The structure of C. e/egans HIM-3 reveals conserved "closure motifs."**

(A) Structurally aligned HIM-3 (colored as in Figure 1A), "closed" Mad2 in complex with Mad1 (PDB ID 1G04, (Sironi et al., 2002)), and Rev? in complex with Rev3 (PDB ID 3VU7, (Kikuchi et al., 2012)). HIM-3:Mad2 Ca r.m.s.d. 1.66 Å over 166 residues; HIM-3:Rev7 Ca r.m.s.d. 1.77 Å over 149 residues; Mad2:Rev7 Ca r.m.s.d. 1.42 Å over 170 residues. (B) Sequence alignment of nematode HIM-3 orthologs, showing the conserved C-terminal closure motifs. *Green box:* ordered closure motif in HIM-3 crystal structure. (C) Sequence alignment of HTP-1/HTP-2 orthologs in Caenorhabditids, showing the conserved C-terminal closure motifs. HTP-1:HTP-2 identity is 83% in C. *elegans*, 97% in C. *brenneri*, 52% in C. *japonica*, and 46% in C. *briggsae* (CBR-HTP-2 and CBG23415 in alignment). (D) Likely closure motifs of C. *e/egans*, C. *sp.* 5, C. *remanei*, C. *briggsae*, C. *brenneri*, and C. *japonica* HTP-3 proteins.

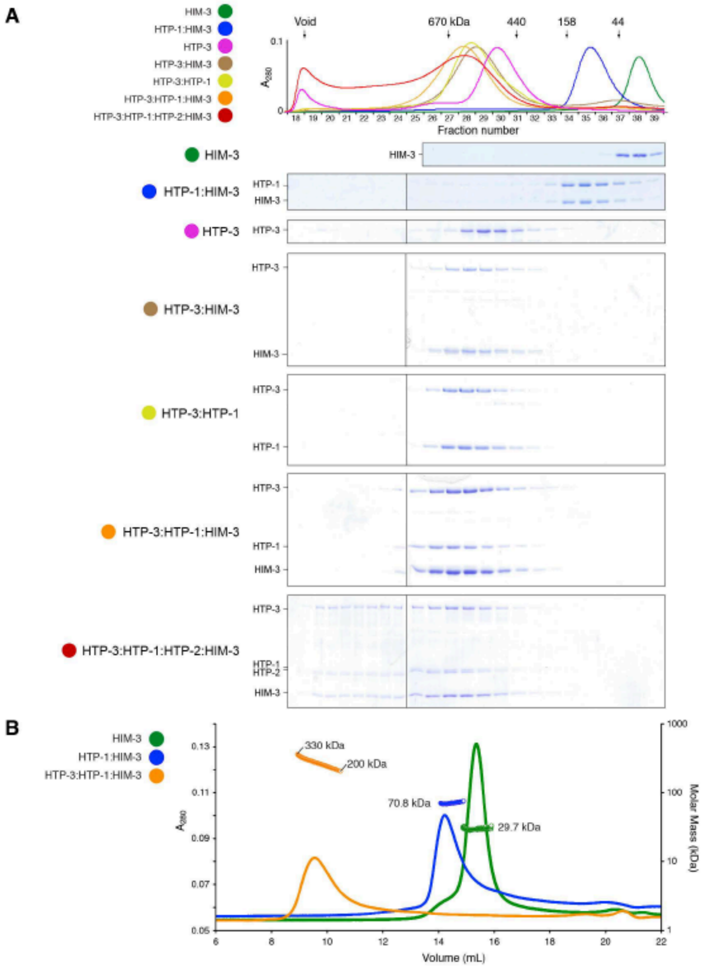

**Figure S1.2 (related to Figure 1.2) -In vitro characterization of C. elegans HORMA protein complexes.**

(A) SDS-PAGE analysis of Superose 6 size-exclusion fractions for C. *e/egans* HORMA protein complexes. (B) Superdex 200 size-exclusion chromatography/multi-angle light scattering (SEC-MALS) analysis of representative complexes from (A), showing monodispersity of HIM-3 (green) and HIM-3:HTP-1 (blue; flat molecular weight measurement across each peak) versus polydispersity of HTP-3:HTP-1:HIM-3 indicative of a mixture of different-weight particles (orange; sloped molecular weight measurement across peak).

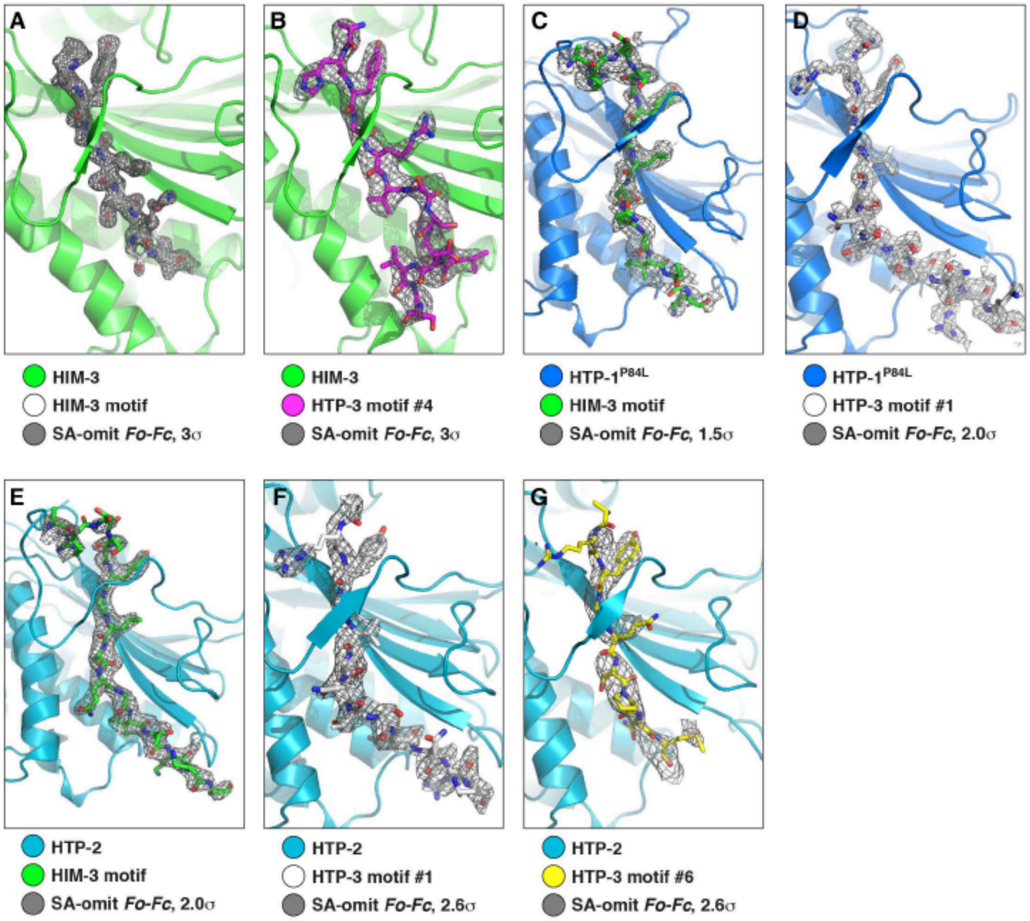

**Figure S1.3 (related to Figures 1.1, 1.4, and 1.5)- Closure motif electron density.**

Simulated annealing *Fo-Fc* map calculated with closure motif peptide omitted, for (A) HIM-3:HIM-3 motif at 1.75 A; (B) HIM-3:HTP-3 motif #4 at 2.85 A; (C) HTP-1P84L:HIM-3 motif at 2.4 A; (D) HTP-1P84L:HTP-3 motif #1 at 2.3 A; (E) HTP-2:HIM-3 motif at 2.55 A; (F) HTP-2:HTP-3 motif #1 at 2.3 A; (G) and HTP-2:HTP-3 motif #6 at 3.1/3.4 A.

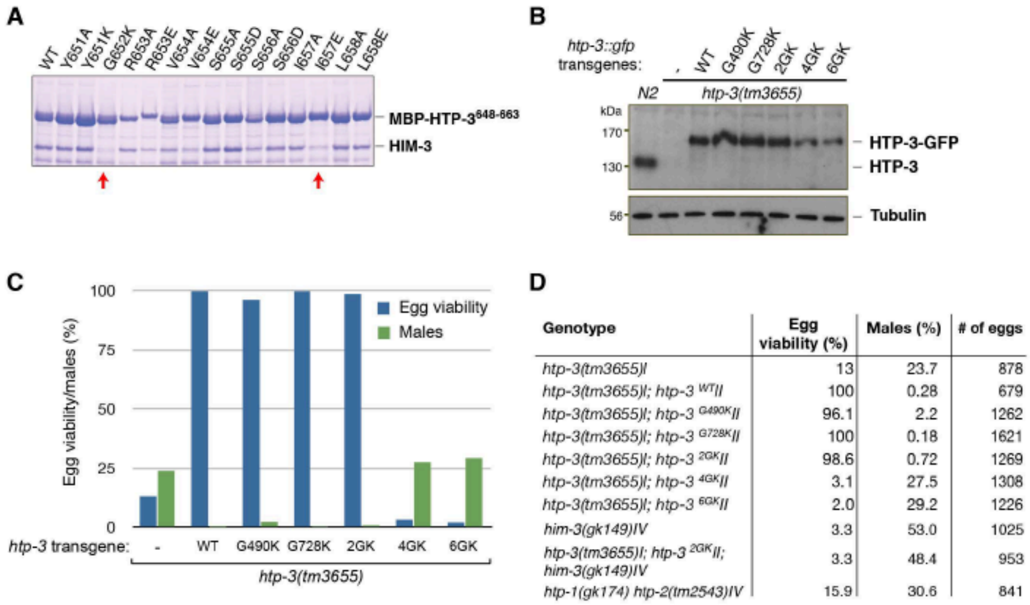

| Genotype | Egg viability (%) | Males (%) | # of eggs |
|---|---|---|---|
| *htp-3(tm3655)I* | 13 | 23.7 | 878 |
| *htp-3(tm3655)I; htp-3* $^{WT}$*II* | 100 | 0.28 | 679 |
| *htp-3(tm3655)I; htp-3* $^{G490K}$*II* | 96.1 | 2.2 | 1262 |
| *htp-3(tm3655)I; htp-3* $^{G728K}$*II* | 100 | 0.18 | 1621 |
| *htp-3(tm3655)I; htp-3* $^{2GK}$*II* | 98.6 | 0.72 | 1269 |
| *htp-3(tm3655)I; htp-3* $^{4GK}$*II* | 3.1 | 27.5 | 1308 |
| *htp-3(tm3655)I; htp-3* $^{6GK}$*II* | 2.0 | 29.2 | 1226 |
| *him-3(gk149)IV* | 3.3 | 53.0 | 1025 |
| *htp-3(tm3655)I; htp-3* $^{2GK}$*II; him-3(gk149)IV* | 3.3 | 48.4 | 953 |
| *htp-1(gk174) htp-2(tm2543)IV* | 15.9 | 30.6 | 841 |

**Figure S1.4 (related to Figures 1.4 and 1.5) -Validation of HTP-3 GK mutations.**

(A) Co-expression of HIM-3 with His6-MBP-HTP-3 motif #4 (residues 648-663). Soluble *E. coli* extracts were incubated with Ni-NTA beads, washed, then bound proteins were eluted and visualized by SDS-PAGE. Red arrows indicate mutations (G652K, 1657E) that strongly affected association of HIM-3. (B) Western blot showing expression levels of HTP-3-GFP transgenes in *htp-3(tm3655)* background. (C Percent viable) /male self-progeny for C. *e/egans* hermaphrodites expressing HTP-3-GFP GK mutants *(htp-3(tm3655)* background). (D) Detailed C. *e/egans* strain information.

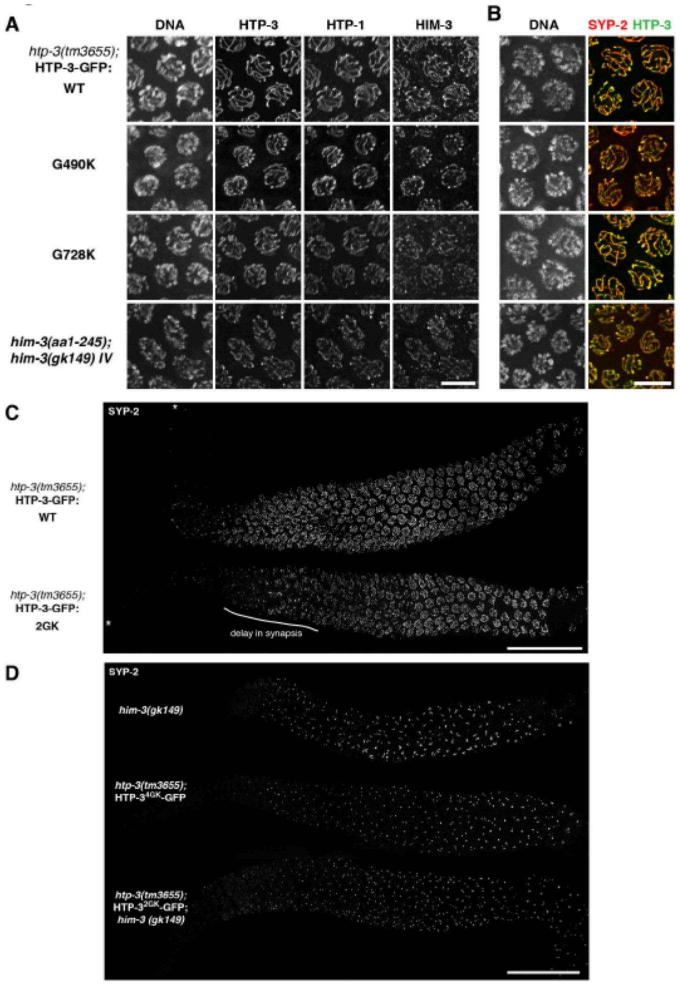

**Figure S1.5 (Related to Figures 1.4 and 1.5) - Synaptonemal Complex assembly in HTP-3 GK mutant strains.**

(A) Worms strains expressing wild-type and GK mutant *htp-3-gfp* transgenes were crossed into the *htp-3(tm3655)* background. A worm strain expressing truncated *him-3(1-245)* transgene was crossed into the *him-3(gk149)* background. Gonads from from the resulting animals were stained for DNA, HTP-3:GFP, HTP-1, and HIM-3. All images show maximum-intensity projections of deconvolved 3D images of mid-pachytene nuclei. Scale bar, 5 IJm. (B) Nuclei from the same set of worm strains shown in (A) were stained for DNA, HTP-3:GFP (green), and SYP-2 (red). Scale bar, 5 IJm. (C) Whole gonads from worm strains expressing wild-type and HTP-32GK transgenes in *htp-3(tm3655)* background were stained for SYP-2. The distal end is to the left (asterisk). (D) Whole gonads from *him-3(gk149), htp-3(tm3655);* htp-34GK, and *htp-3(tm3655);* htp-34GK; *him-3(gk149)* were stained for SYP-2. The distal end is to the left. Scale bar, 50 IJm.

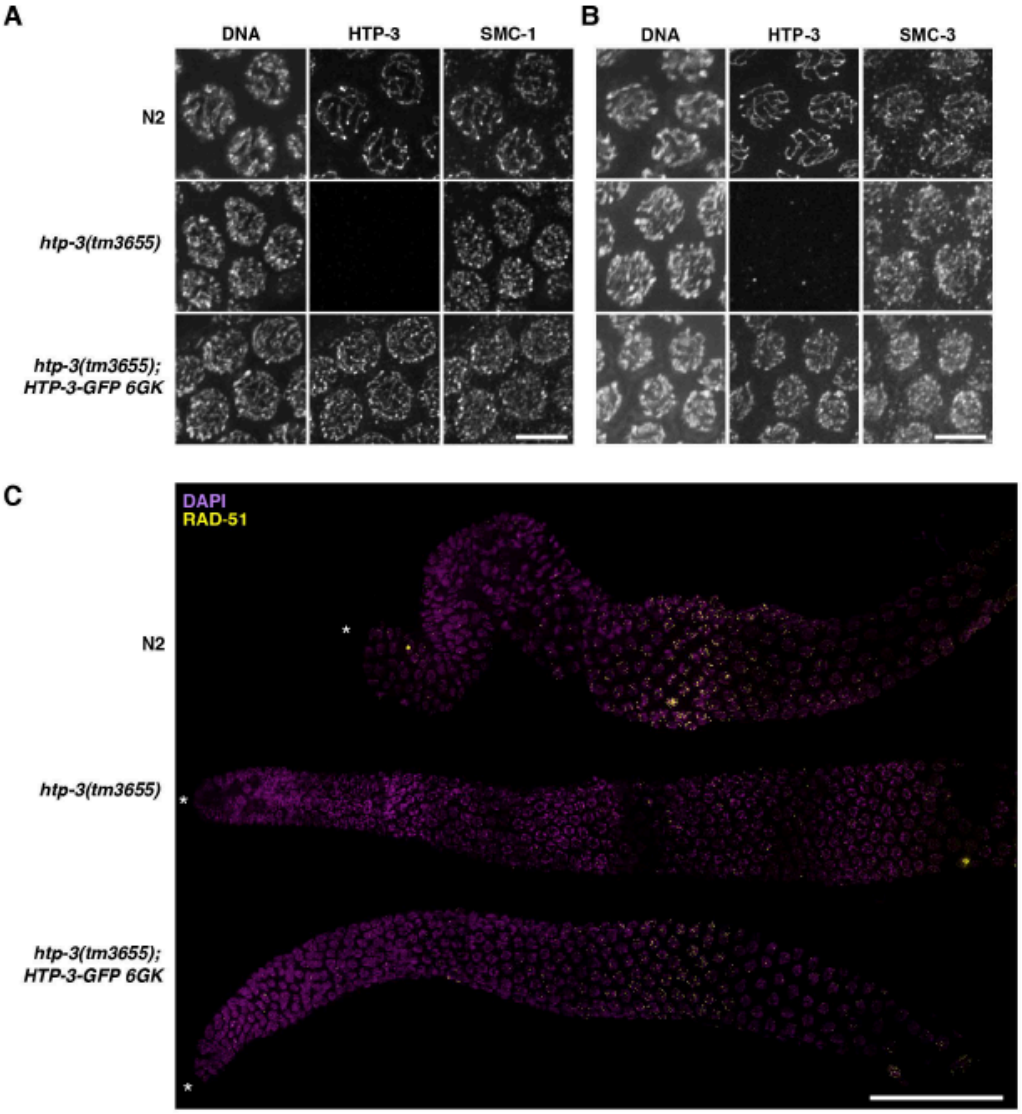

**Figure S1.6 (Related to Figure 1.6) -Chromosome axis localization of cohesin complexes and DSB formation in HTP-3 closure motif GK mutants.**

Mid-pachytene nuclei from wild-type N2, *htp-3* mutant *(tm3655),* and *htp-3 (tm3655);htp-3*$^{6GK}$ worms, stained for HTP-3 and SMC subunits shared by all mitotic and meiotic cohesin complexes, SMC-1 (A) or SMC-3 (B). Scale bar, 5 iJm. (C) Immunofluorescence images of whole gonads showing DAPI (purple) and RAD-51 (yellow) staining in *N2, htp-3(tm3655),* and *htp-3(tm3655);htp-3*$^{6GK}$ worms. The distal end is to the left (asterisk). Scale bar, 50 iJm.

## 1.7 References

Aravind, L., and Koonin, E.V. (1998). The HORMA domain: a common structural denominator in mitotic checkpoints, chromosome synapsis and DNA repair. Trends Biochem. Sci. *23*, 284–286.

Baumgartner, B., Woltering, D., Bagchi, S., Larkin, B., Loidl, J., de los Santos, T., and Hollingsworth, N.M. (2000). Meiotic segregation, synapsis, and recombination checkpoint functions require physical interaction between the chromosomal proteins Red1p and Hop1p. Mol Cell Biol *20*, 6646–6658.

Blat, Y., Protacio, R.U., Hunter, N., and Kleckner, N. (2002). Physical and functional interactions among basic chromosome organizational features govern early steps of meiotic chiasma formation. Cell *111*, 791–802.

Burger, J., Merlet, J., Tavernier, N., Richaudeau, B., Arnold, A., Ciosk, R., Bowerman, B., and Pintard, L. (2013). CRL2(LRR-1) E3-ligase regulates proliferation and progression through meiosis in the *Caenorhabditis elegans* germline. PLoS Genet *9*, e1003375.

Caryl, A.P., Armstrong, S.J., Jones, G.H., and Franklin, F.C. (2000). A homologue of the yeast *HOP1* gene is inactivated in the *Arabidopsis* meiotic mutant *asy1*. Chromosoma *109*, 62–71.

Chen, Y.-T., Venditti, C.A., Theiler, G., Stevenson, B.J., Iseli, C., Gure, A.O., Jongeneel, C.V., Old, L.J., and Simpson, A.J.G. (2005). Identification of CT46/HORMAD1, an immunogenic cancer/testis antigen encoding a putative meiosis-related protein. Cancer Immun. *5*, 9.

Colaiácovo, M.P., Macqueen, A.J., Martinez-Perez, E., McDonald, K., Adamo, A., La Volpe, A., and Villeneuve, A.M. (2003). Synaptonemal complex assembly in *C. elegans* is dispensable for loading strand-exchange proteins but critical for proper completion of recombination. Dev Cell *5*, 463–474.

Couteau, F., and Zetka, M. (2005). HTP-1 coordinates synaptonemal complex assembly with homolog alignment during meiosis in *C. elegans*. Genes Dev. *19*, 2744–2756.

Couteau, F., and Zetka, M. (2011). DNA Damage during Meiosis Induces Chromatin Remodeling and Synaptonemal Complex Disassembly. Dev Cell *20*, 353–363.

Couteau, F., Nabeshima, K., Villeneuve, A., and Zetka, M. (2004). A component of *C. elegans* meiotic chromosome axes at the interface of homolog alignment, synapsis, nuclear reorganization, and recombination. Curr. Biol. *14*, 585–592.

Daniel, K., Lange, J., Hached, K., Fu, J., Anastassiadis, K., Roig, I., Cooke, H.J., Stewart, A.F., Wassmann, K., Jasin, M., et al. (2011). Meiotic homologue alignment and its quality surveillance are controlled by mouse HORMAD1. Nat. Cell Biol. *13*, 599–610.

de Carvalho, C.E., Zaaijer, S., Smolikov, S., Gu, Y., Schumacher, J.M., and Colaiácovo, M.P. (2008). LAB-1 antagonizes the Aurora B kinase in *C. elegans*. Genes Dev. *22*, 2869–2885.

Friedman, D.B., Hollingsworth, N.M., and Byers, B. (1994). Insertional mutations in the yeast *HOP1* gene: evidence for multimeric assembly in meiosis. Genetics *136*, 449–464.

Frøkjaer-Jensen, C., Davis, M.W., Hopkins, C.E., Newman, B.J., Thummel, J.M., Olesen, S.-P., Grunnet, M., and Jorgensen, E.M. (2008). Single-copy insertion of transgenes in *Caenorhabditis elegans*. Nat Genet *40*, 1375–1383.

Fukuda, T., Daniel, K., Wojtasz, L., Toth, A., and Höög, C. (2010). A novel mammalian HORMA domain-containing protein, HORMAD1, preferentially associates with unsynapsed meiotic chromosomes. Exp Cell Res *316*, 158–171.

Goodyer, W., Kaitna, S., Couteau, F., Ward, J.D., Boulton, S.J., and Zetka, M. (2008). HTP-3 links DSB formation with homolog pairing and crossing over during *C. elegans* meiosis. Dev Cell *14*, 263–274.

Hara, K., Hashimoto, H., Murakumo, Y., Kobayashi, S., Kogame, T., Unzai, S., Akashi, S., Takeda, S., Shimizu, T., and Sato, M. (2010). Crystal structure of human REV7 in complex with a human REV3 fragment and structural implication of the interaction between DNA polymerase zeta and REV1. J Biol Chem *285*, 12299–12307.

Hara, K., Shimizu, T., Unzai, S., Akashi, S., Sato, M., and Hashimoto, H. (2009). Purification, crystallization and initial X-ray diffraction study of human REV7 in complex with a REV3 fragment. Acta Crystallogr. Sect. F Struct. Biol. Cryst. Commun. *65*, 1302–1305.

Harper, N.C., Rillo, R., Jover-Gil, S., Assaf, Z.J., Bhalla, N., and Dernburg, A.F. (2011). Pairing centers recruit a Polo-like kinase to orchestrate meiotic chromosome dynamics in *C. elegans*. Dev Cell *21*, 934–947.

Hodgkin, J., Horvitz, H.R., and Brenner, S. (1979). Nondisjunction Mutants of the Nematode *CAENORHABDITIS ELEGANS*. Genetics *91*, 67–94.

Hollingsworth, N.M., and Johnson, A.D. (1993). A conditional allele of the *Saccharomyces cerevisiae HOP1* gene is suppressed by overexpression of two other meiosis-specific genes: *RED1* and *REC104*. Genetics *133*, 785–797.

Hollingsworth, N.M., Goetsch, L., and Byers, B. (1990). The *HOP1* gene encodes a meiosis-specific component of yeast chromosomes. Cell *61*, 73–84.

Jao, C.C., Ragusa, M.J., Stanley, R.E., and Hurley, J.H. (2013). A HORMA domain in Atg13 mediates PI 3-kinase recruitment in autophagy. Proc. Natl. Acad. Sci. USA *110*, 5486–5491.

Kaitna, S., Pasierbek, P., Jantsch, M., Loidl, J., and Glotzer, M. (2002). The aurora B kinase AIR-2 regulates kinetochores during mitosis and is required for separation of homologous Chromosomes during meiosis. Curr. Biol. *12*, 798–812.

Karplus, P.A., and Diederichs, K. (2012). Linking crystallographic model and data quality. Science *336*, 1030–1033.

Kikuchi, S., Hara, K., Shimizu, T., Sato, M., and Hashimoto, H. (2012). Structural basis of recruitment of DNA polymerase ζ by interaction between REV1 and REV7 proteins. J Biol Chem *287*, 33847–33852.

Kleckner, N. (2006). Chiasma formation: chromatin/axis interplay and the role(s) of the synaptonemal complex. Chromosoma *115*, 175–194.

Klein, F., Mahr, P., Gálová, M., Buonomo, S.B., Michaelis, C., Nairz, K., and Nasmyth, K. (1999). A central role for cohesins in sister chromatid cohesion, formation of axial elements, and recombination during yeast meiosis. Cell *98*, 91–103.

Llano, E., Herrán, Y., García-Tuñón, I., Gutiérrez-Caballero, C., de Álava, E., Barbero, J.L., Schimenti, J., de Rooij, D.G., Sánchez-Martín, M., and Pendás, A.M. (2012). Meiotic cohesin complexes are essential for the formation of the axial element in mice. J Cell Biol *197*, 877–885.

Luo, X., Fang, G., Coldiron, M., Lin, Y., Yu, H., Kirschner, M.W., and Wagner, G. (2000). Structure of the Mad2 spindle assembly checkpoint protein and its interaction with Cdc20. Nat. Struct. Biol. *7*, 224–229.

Luo, X., Tang, Z., Rizo, J., and Yu, H. (2002). The Mad2 spindle checkpoint protein undergoes similar major conformational changes upon binding to either Mad1 or Cdc20. Mol Cell *9*, 59–71.

Luo, X., Tang, Z., Xia, G., Wassmann, K., Matsumoto, T., Rizo, J., and Yu, H. (2004). The Mad2 spindle checkpoint protein has two distinct natively folded states. Nat Struct Mol Biol *11*, 338–345.

Mapelli, M., Massimiliano, L., Santaguida, S., and Musacchio, A. (2007). The Mad2 Conformational Dimer: Structure and Implications for the Spindle Assembly Checkpoint. Cell *131*, 730–743.

Martinez-Perez, E., and Villeneuve, A.M. (2005). HTP-1-dependent constraints coordinate homolog pairing and synapsis and promote chiasma formation during *C. elegans* meiosis. Genes Dev. *19*, 2727–2743.

Martinez-Perez, E., Schvarzstein, M., Barroso, C., Lightfoot, J., Dernburg, A.F., and

Villeneuve, A.M. (2008). Crossovers trigger a remodeling of meiotic chromosome axis composition that is linked to two-step loss of sister chromatid cohesion. Genes Dev. *22*, 2886–2901.

Nabeshima, K., Villeneuve, A.M., and Colaiácovo, M.P. (2005). Crossing over is coupled to late meiotic prophase bivalent differentiation through asymmetric disassembly of the SC. J Cell Biol *168*, 683–689.

Niu, H., Wan, L., Baumgartner, B., Schaefer, D., Loidl, J., and Hollingsworth, N.M. (2005). Partner choice during meiosis is regulated by Hop1-promoted dimerization of Mek1. Mol Biol Cell *16*, 5804–5818.

Orth, M., Mayer, B., Rehm, K., Rothweiler, U., Heidmann, D., Holak, T.A., and Stemmann, O. (2011). Shugoshin is a Mad1/Cdc20-like interactor of Mad2. Embo J *30*, 2868–2880.

Pangas, S.A., Yan, W., Matzuk, M.M., and Rajkovic, A. (2004). Restricted germ cell expression of a gene encoding a novel mammalian HORMA domain-containing protein. Gene Expr. Patterns *5*, 257–263.

Panizza, S., Mendoza, M.A., Berlinger, M., Huang, L., Nicolas, A., Shirahige, K., and Klein, F. (2011). Spo11-accessory proteins link double-strand break sites to the chromosome axis in early meiotic recombination. Cell *146*, 372–383.

Pasierbek, P., Jantsch, M., Melcher, M., Schleiffer, A., Schweizer, D., and Loidl, J. (2001). A *Caenorhabditis elegans* cohesion protein with functions in meiotic chromosome pairing and disjunction. Genes Dev. *15*, 1349–1360.

Phillips, C.M., McDonald, K.L., and Dernburg, A.F. (2009). Cytological analysis of meiosis in Caenorhabditis elegans. Methods Mol Biol *558*, 171–195.

Rogers, E., Bishop, J.D., Waddle, J.A., Schumacher, J.M., and Lin, R. (2002). The aurora kinase AIR-2 functions in the release of chromosome cohesion in *Caenorhabditis elegans* meiosis. J Cell Biol *157*, 219–229.

Rothbauer, U., Zolghadr, K., Muyldermans, S., Schepers, A., Cardoso, M.C., and Leonhardt, H. (2008). A versatile nanotrap for biochemical and functional studies with fluorescent fusion proteins. Mol. Cell Proteomics *7*, 282–289.

Schwacha, A., and Kleckner, N. (1997). Interhomolog bias during meiotic recombination: meiotic functions promote a highly differentiated interhomolog-only pathway. Cell *90*, 1123–1135.

Severson, A.F., Ling, L., van Zuylen, V., and Meyer, B.J. (2009). The axial element protein HTP-3 promotes cohesin loading and meiotic axis assembly in *C. elegans* to implement the meiotic program of chromosome segregation. Genes Dev. *23*, 1763–1778.

Shin, Y.-H., Choi, Y., Erdin, S.U., Yatsenko, S.A., Kloc, M., Yang, F., Wang, P.J., Meistrich, M.L., and Rajkovic, A. (2010). *Hormad1* mutation disrupts synaptonemal complex formation, recombination, and chromosome segregation in mammalian meiosis. PLoS Genet *6*, e1001190.

Sironi, L., Mapelli, M., Knapp, S., de Antoni, A., Jeang, K.-T., and Musacchio, A. (2002). Crystal structure of the tetrameric Mad1-Mad2 core complex: implications of a “safety belt” binding mechanism for the spindle checkpoint. Embo J *21*, 2496–2506.

Sung, P. (1994). Catalysis of ATP-dependent homologous DNA pairing and strand exchange by yeast RAD51 protein. Science *265*, 1241–1243.

Tzur, Y.B., Egydio de Carvalho, C., Nadarajan, S., Van Bostelen, I., Gu, Y., Chu, D.S., Cheeseman, I.M., and Colaiácovo, M.P. (2012). LAB-1 targets PP1 and restricts Aurora B kinase upon entrance into meiosis to promote sister chromatid cohesion. PLoS Biol *10*, e1001378.

Washburn, M.P., Wolters, D., and Yates, J.R. (2001). Large-scale analysis of the yeast proteome by multidimensional protein identification technology. Nat. Biotechnol. *19*, 242–247.

Winters, T., McNicoll, F., and Jessberger, R. (2014). Meiotic cohesin STAG3 is required for chromosome axis formation and sister chromatid cohesion. Embo J *33*, 1256–1270.

Wojtasz, L., Cloutier, J.M., Baumann, M., Daniel, K., Varga, J., Fu, J., Anastassiadis, K., Stewart, A.F., Reményi, A., Turner, J.M.A., et al. (2012). Meiotic DNA double-strand breaks and chromosome asynapsis in mice are monitored by distinct HORMAD2-independent and -dependent mechanisms. Genes Dev. *26*, 958–973.

Wojtasz, L., Daniel, K., Roig, I., Bolcun-Filas, E., Xu, H., Boonsanay, V., Eckmann, C.R., Cooke, H.J., Jasin, M., Keeney, S., et al. (2009). Mouse HORMAD1 and HORMAD2, two conserved meiotic chromosomal proteins, are depleted from synapsed chromosome axes with the help of TRIP13 AAA-ATPase. PLoS Genet *5*, e1000702.

Xia, G., Luo, X., Habu, T., Rizo, J., Matsumoto, T., and Yu, H. (2004). Conformation-specific binding of p31(comet) antagonizes the function of Mad2 in the spindle checkpoint. Embo J *23*, 3133–3143.

Yang, M., Li, B., Tomchick, D.R., Machius, M., Rizo, J., Yu, H., and Luo, X. (2007). p31comet blocks Mad2 activation through structural mimicry. Cell *131*, 744–755.

Zetka, M.C., Kawasaki, I., Strome, S., and Müller, F. (1999). Synapsis and chiasma formation in *Caenorhabditis elegans* require HIM-3, a meiotic chromosome core component that functions in chromosome segregation. Genes Dev. *13*, 2258–2270.

Zickler, D., and Kleckner, N. (1999). Meiotic chromosomes: integrating structure and function. Annu Rev Genet *33*, 603–754.

## 1.8 Acknowledgements

Chapter1, in full, is a repreint of the material as it appears in The chromosome axis controls meiotic events through a hierarchical assembly of HORMA domain proteins. Dev Cell. 2014 Nov 24;31(4):487-502. doi: 10.1016/j.devcel.2014.09.013. Epub 2014 Nov 6. PubMed PMID: 25446517; PubMed Central PMCID: PMC4254552. Kim Y, Rosenberg SC, Kugel CL, Kostow N, Rog O, Davydov V, Su TY, Dernburg AF, Corbett KD. The dissertation author is the primary co-author for this paper.

We thank the staffs of NE-CAT beamlines 24ID-C and 24ID-E at the Advanced Photon Source (Argonne, IL), BCSB beamline 8.2.1 at the Advanced Light Source (Berkeley, CA), and beamlines 7-1 and 12-2 at Stanford Synchrotron Light Source (Stanford, CA) for assistance with data collection (see Supplemental Material for synchrotron support statements). We thank Barbara Meyer for providing the anti-SMC-1 antibody, and Lori Kohlstaedt at the UC Berkeley P/MSL for help with mass spectrometry. YK is an HHMI Postdoctoral Fellow of the Damon Runyon Cancer Research Foundation (DRG 2084-11). AFD acknowledges support from the National Institutes of Health (R01 GM065591) and the Howard Hughes Medical Institute, KDC acknowledges support from the Ludwig Institute for Cancer Research, the Sidney Kimmel Foundation Kimmel Scholars program, and the National Institutes of Health (R01 GM104141).

# Chapter 2: Organization of the Mammalian Axial Element

## 2.1 Summary

The chromosome axis is an essential meiotic structure that recruits and controls the recombination machinery and synaptonemal complex, resulting in proper pairing and segregation of homologous chromosomes. While the cohesin complexes, SYCP2, SYCP3, and the HORMADs are recognized as the core components of the mammalian chromosome axis, their assembly mechanisms remain poorly understood. Here we demonstrate that SYCP2 and SYCP3 physically interact through the coiled-coil domains at their C-termini to form 2:2 heterotetramers, which then further assemble into large fiber-like structures. We also show that HORMAD2 can directly bind to a 20-residue motif present in the disordered region of SYCP2, revealing structural and functional parallels between SYCP2 and the yeast protein Red1. This work suggests that the axis foundation proteins SYCP2 and SYCP3 form the contiguous backbone of the meiotic chromosome axis, and suggests that the architecturally similar Red1 protein may function equivalently in fungi.

## 2.2 Introduction

The chromosome axis or axial element (AE) plays central roles in meiotic prophase, physically organizing the chromosomes into a linear loop array and acting as a scaffold of assembly for the recombination machinery and synaptonemal complex (Kleckner, 2006). Meiosis-specific HORMA domain containing proteins (HORMADs) on the AE are required for the recruitment of the DSB protein SPO11 and its accessory factors, which mediate double-strand DNA breakage and initiate the homology search and homolog pairing process (Panizza et al., 2011). After successfully pairing, homologous chromosomes become linked by the transverse filaments of the synaptonemal complex (SC), which assemble between the paired homologs' chromosome axes, which are thereafter referred to as the lateral elements of the SC (Page and Hawley, 2004). Assembly and disassembly of the axis is a dynamic process that is tightly coordinated with progression of meiotic prophase. In many organisms, meiotic HORMADs are removed from regions of the chromosomes that have obtained crossovers and synapsed, thereby down-regulating further DSB formation (Börner et al., 2008; Wojtasz et al., 2009) (Lambing et al., 2015). Although the major components of the axis have largely been identified, the underlying molecular architecture of the AE remains mysterious. Outlining how the structural components of the chromosome axis are assembled will be an important step in understanding the roles of the AE in organizing the meiotic genome and controlling the recombination machinery to promote homolog pairing and recombination.

Along with their well defined roles in sister chromatid cohesion, the meiosis-specific cohesin complexes have also been demonstrated to be the most essential components of the chromosome axis, without which there is no discernable AE (Klein et al., 1999; Llano et al., 2012; Winters et al., 2014). The previous chapter outlined the organization and roles of the meiotic HORMAD proteins as highly conserved elements of the chromosome axis (Y. Kim et al., 2014). Another major component of the chromosome axis in many organisms are proteins we will refer to as "AE foundation proteins", including SYCP2 and SYCP3 in mammals, Red1 in yeast, and ASY3/PAIR3 in plants (Ferdous et al., 2012; Lammers et al., 1994; Offenberg, 1998; Smith and Roeder, 1997; Wang et al., 2011). Although the molecular roles of these proteins remain mysterious, they have been shown to be important structural elements of the chromosome axis, and are essential for homolog pairing, synapsis, and recombination (Li et al., 2011; Wang et al., 2011; Yang et al., 2006; Yuan et al., 2000). One established structural role for the LE foundation proteins in various organisms is the recruitment of meiotic HORMAD proteins (Ferdous et al., 2012; Fukuda et al., 2010; Wang et al., 2011; Woltering et al., 2000).

Although a cohesin-based axis can still form in the absence of other AE proteins, disrupting the foundation proteins results in severe defects to AE morphology, exemplified by discontinuous staining of cohesin proteins in mammals and plants (Kouznetsova, 2005; Pelttari et al., 2001; Wang et al., 2011). In mammals, SYCP3 deletion results in a two-fold increase in overall chromosome length, and a concomitant 50% reduction of chromatin loop length (Kolas et al., 2004; Novak et al., 2008). While highly diverged between different organisms, the AE foundation proteins share a predicted well-ordered N-terminal domain, and a predicted C-terminal coiled-coil domain (Ferdous et al., 2012; Offenberg, 1998; Wang et al., 2011; Woltering et al., 2000). Red1 and SYCP2/SYCP3 have also been shown to self-interact or oligomerize into higher order structures through their coiled-coil domains (Baier et al., 2007; Pelttari et al., 2001; Woltering et al., 2000; Yuan et al., 1998). Based on the interdependent relationship between the AE foundation proteins and cohesins, and the AE defects observed in the absence of Red1/SYCP2/SYCP3/PAIR3, we propose an important structural role for the foundation AE proteins in providing another layer of organization to the chromosomes, by coordinating the cohesin complexes into a compacted linear array. Here we present a biochemical and structural characterization of SYCP2 and SYCP3, establishing a molecular basis for axis assembly and genome organization, drawing parallels to the yeast lateral element protein Red1.

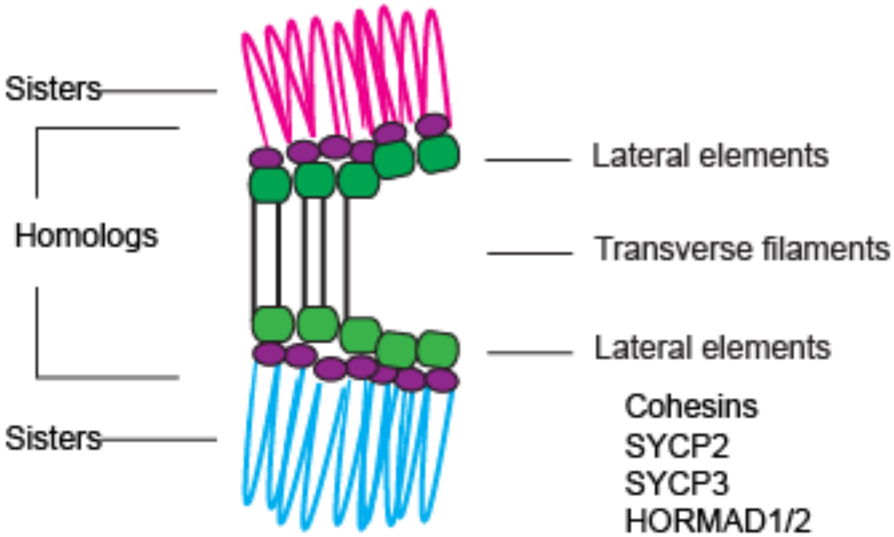

**Figure 2.1 Model of mammalian chromosome organization in prophase**

## 2.3 Results

### 2.2.1 SYCP2 possesses a central HORMAD-binding closure motif revealing structural parallels to Red1

Despite very low sequence homology, SYCP2 has been proposed to be a Red1 homolog since its discovery (Offenberg, 1998). SYCP2 and Red1 both share similar structural predictions, have ordered N-terminal domains separated from a C-terminal coiled-coil domain by long disordered regions (Figure 2.2A). The N-terminal domains of Red1 and SYCP2 are of similar overall size (340 and 394 residues respectively), and can be overexpressed in *E. coli* and purified. The structure of the SYCP2 N-terminus was recently determined, demonstrating that it contains an Armadillo repeat-like domain (ARLD) juxtaposed to a Sptm16-like domain (SLD) (Feng et al., 2017). Little is known about the biological function of the domain, though it is presumed to mediate chromatin localization of the protein. In *S. cerevisiae*, Red1 has been shown to be an important recruiter of Hop1, through a 30-residue motif directly downstream of its N-terminal domain(Woltering et al., 2000). Mutation of this motif significantly reduces Hop1 localization to chromosomes, and results in a reduction of DSBs and accurate homolog pairing(Wan, 2003; Woltering et al., 2000). Recent work from our lab (West et al NAR in press) has further shown that the Hop1-binding motif of Red1 is a *bona fide* closure motif that binds the Hop1 HORMA domain.

To build a molecular model of mammalian chromosome axis architecture, we first performed a yeast two-hybrid assay to identify and confirm interactions between *M. musculus* SYCP2, SYCP3, and HORMAD2 (Figure 2.2B). We confirmed a previously-reported interaction between the coiled-coil regions of SYCP2 and SYCP3, and also identified an interaction between HORMAD2 and a region of SYCP2 spanning residues 390-600. Using a combination of yeast two-hybrid assays and polycistronic bacterial co-expression of HORMAD2$^{2\text{-}241}$ and SYCP2 truncations, we further narrowed down this interaction motif to SYCP2 residues 395-414 (Figure 2.2C). The ability of SYCP2 to directly interact with HORMAD2 reveals another functional and structural parallel with Red1.

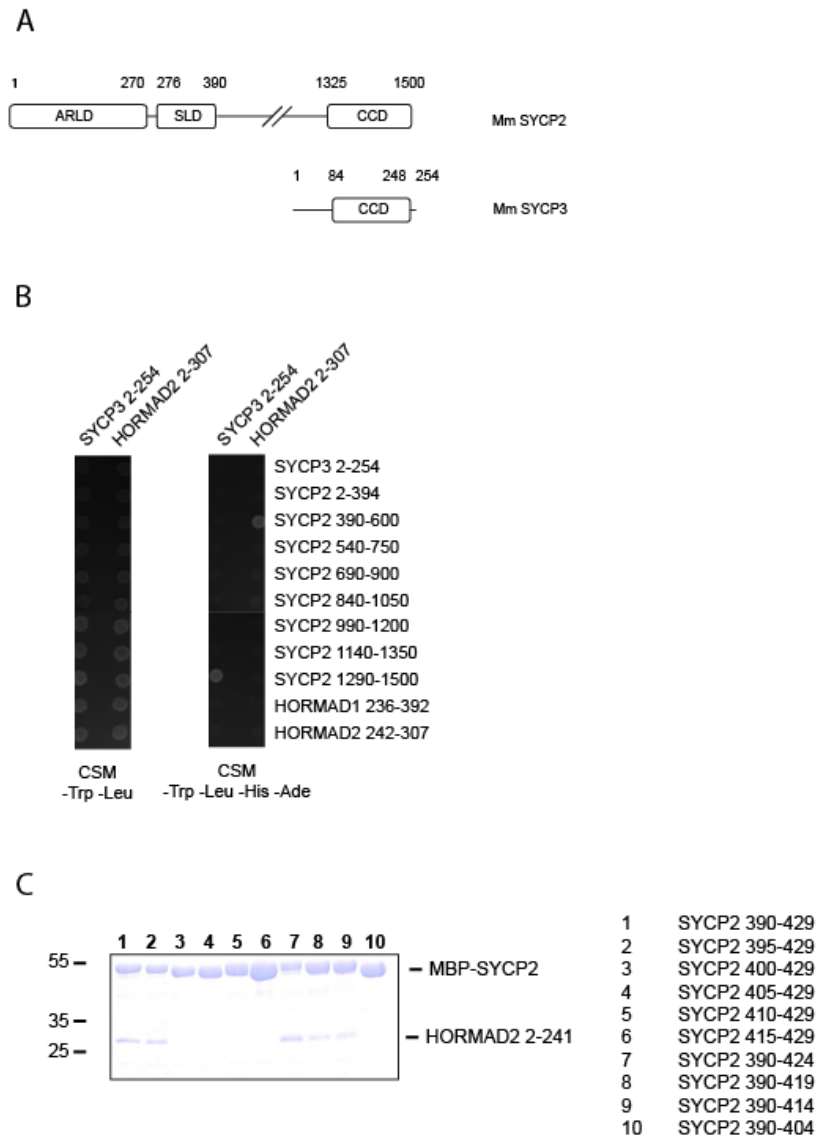

**Figure 2.2 A network of interactions underlies mammalian chromosome axis organization**

(A) Domain outline of SYCP2 and SYCP3. (B) Yeast Two-Hybrid analysis demonstrating binding of FL SYCP3 to the coiled-coil domain of SYCP2 (1290-1500) and HORMAD2 binding to the disordered region of SYCP2 (390-600) (C) In vitro purification of HORMAD2 HORMA domain co-expressed with truncations of the SYCP2 peptide 390-429.

### 2.2.2 The SYCP2 and SYCP3 coiled-coil regions associate and form extended fibers in vitro

The C-terminal coiled-coil of Red1 has been demonstrated to be important for homo-oligomerization (Woltering et al., 2000). SYCP2 and SYCP3 both contain helical/coiled-coil domains at their C-termini (Figure 2.2A), and our results confirm previous findings that these domains can directly interact with each other (Tarsounas et al., 1997) (Pelttari et al., 2001). To outline the architecture of this complex, we aimed to purify and characterize these proteins in vitro. To isolate a stable and soluble complex between SYCP2 and SYCP3, we designed a construct of SYCP3 lacking the disordered 83 N-terminal residues, and also 6 C-terminal residues which have been shown to cause assembly of large SYCP3 fibers/aggregates (Baier et al., 2007; Syrjänen et al., 2014). We co-expressed SYCP3$^{84\text{-}248}$ with SYCP2$^{1325\text{-}1500}$ in *E. coli*, and obtained soluble and stoichiometric complexes as seen by Coomassie blue-stained SDS-PAGE gels (Figure 2.3A). Purification of this complex by size exclusion chromatography resulted in an elution in the void volume (Figure 2.3A). Although proteins that elute in the void volume often form non-specific aggregates, SYCP2 and SYCP3 have been shown to form large fiber like structures when overexpressed in cells (Pelttari et al., 2001), and we suspected the ability of this protein complex to assemble into higher order structures would be an important part of its function.

To determine if the high-molecular weight complexes we purified might be functional aggregates, we visualized our purified samples using negative stain electron microscopy (Figure 2.3B). Our analysis showed that SYCP2 and SYCP3 assemble into large fibers on the order of 100-200 nanometers in length, and only a few nanometers wide. To further test how SYCP2 and SYCP3 might be organized in these higher order structures, we next analyzed a construct with N-terminal maltose binding protein (MBP) tags on SYCP2 (Figure 2.3C). In the resulting electron micrographs, we observed pairs of densities consistent with MBP's size (43 kDa, ~4x6 nm) dotting the length of our SYCP2:SYCP3 fibers in regular intervals of ~23 nm (Figure 2.3D). Given that a 150 residue coiled-coil is predicted to be ~25 nm in length, these results strongly suggest that the SYCP2:SYCP3 complex assembles into a coiled-coil complex, and that these individual complexes interact end-to-end to form higher-order filaments. Further, as most filaments show pairs of MBP densities at each interval along the filament (Figure 2.3C), there are likely two SYCP2 molecules in each coiled-coil unit.

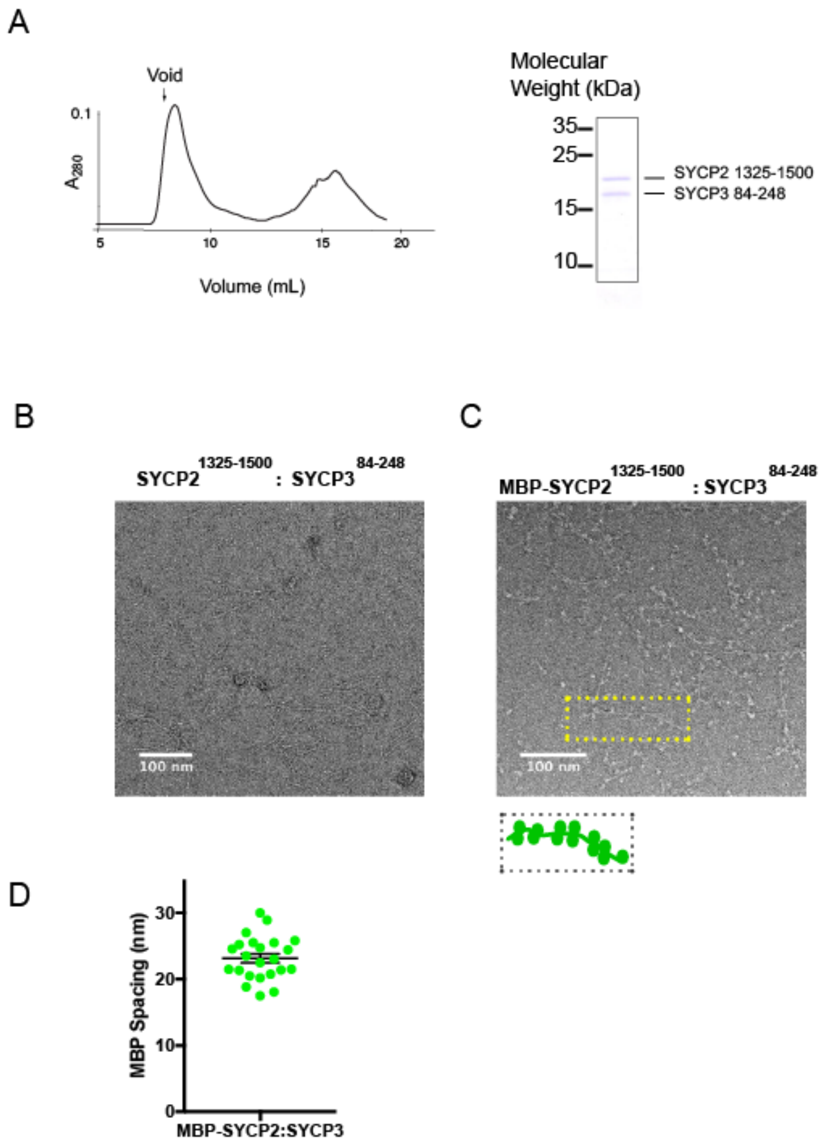

**Figure 2.3 SYCP2 and SYCP3 form filamentous structure in vitro**

(A) Size exclusion chromatography and SDS-PAGE analysis of purified complex between SYCP21325-1500:SYCP384-248. (B) Negative-stain EM of SYCP21325-1500:SYCP384-248. (C) Negative-stain EM of MBP- SYCP21325-1500:SYCP384-248. (D) Measured distances between MBP's along the length of the MBP- SYCP21325-1500:SYCP384-248 fiber.

### 2.2.3 The SYCP2:SYCP3 complex filament is built from 2:2 heterotetramer units

We next sought to isolate the repeating unit of the SYCP2:SYCP3 filaments, to characterize it structurally and outline the molecular architecture of the underlying structures that constitute the chromosome axis. Under the assumption that the fibers were assembled through head to tail interactions of coiled-coil structures, we designed a series of truncations in heptad intervals from the N- and C-termini of our SYCP2 and SYCP3 coiled-coil constructs (Figure 2.4A). We co-expressed each truncation with the un-truncated partner protein, and analyzed the resulting purified complexes by gel filtration chromatography to assess their ability to form fibers based on their elution profiles. Truncation of the N-terminus of our SYCP2 construct had almost no effect on oligomerization when coexpressed with SYCP3$^{84\text{-}248}$. Truncation of the SYCP2 C-terminus, however, had a progressive effect to prevent fiber formation while maintaining tight binding to SYCP3, with removal of the third heptad almost completely favoring formation of a smaller complex (Figure 2.4B). Truncation of the N-terminus of our SYCP3 construct also disrupted filament formation when coexpressed with SYCP2$^{1325\text{-}1500}$ (Figure 2.4B). Removal of two heptads of SYCP3 resulted complete elimination of the fiber formation. Together, these data suggest that the C-terminal region of SYCP2 and the N-terminal region of SYCP3 are responsible for head-to-tail oligomerization of the SYCP2:SYCP3 complex.

We next used size exclusion chromatography coupled to multi-angle light scattering (SEC-MALS) to determine the molecular weight and oligomeric state of our truncated SYCP2:SYCP3 complexes (Figure 2.4C). MBP-SYCP2$^{1325\text{-}1479}$ + SYCP3$^{105\text{-}248}$

eluted as a single peak with a molecular weight of 158 kDa, consistent with a heterotetramer containing two copies of SYCP2 and two copies of SYCP3.

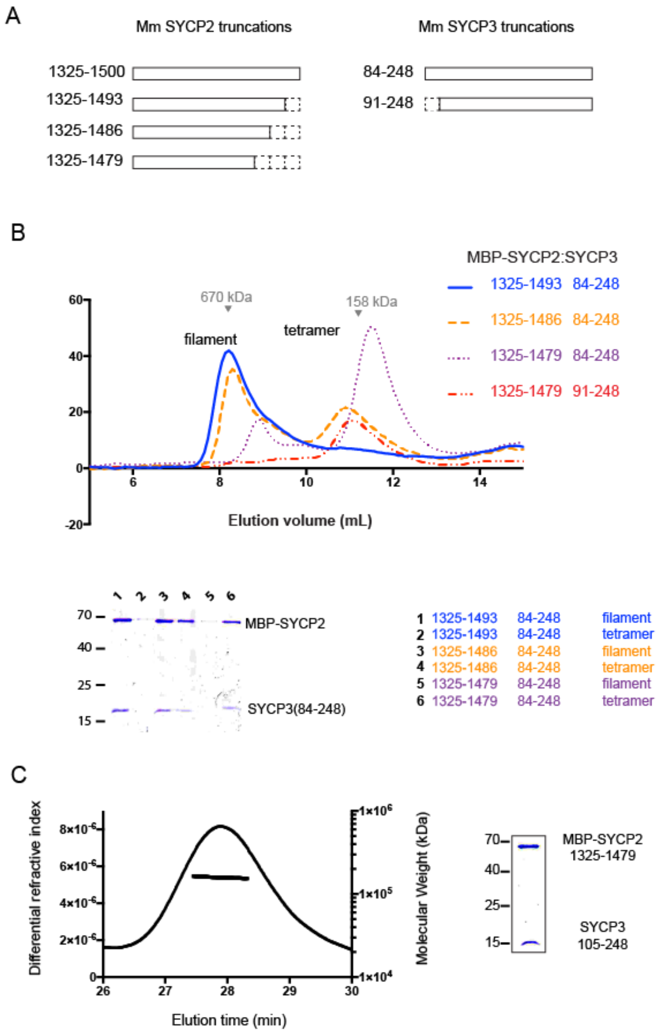

**Figure 2.4 The SYCP2:SYCP3 filament is built from a 2:2 heterotetramer**

(A) Schematic of heptad truncations at the C-terminus of SYCP2 and N-terminus of SYCP3. (B) Size exclusion chromatography and SDS-PAGE analysis of purified SYCP2:SYCP3 truncated complexes. (C) Size exclusion chromatography coupled to multi-angle light scattering (SEC-MALS) and SDS-PAGE analysis of MBP-SYCP2$^{1325\text{-}1479}$:SYCP3$^{105\text{-}248}$

### 2.2.4 Structure of the SYCP3 tetrameric coiled-coil

Prior work with human SYCP3 protein showed that this protein can form a homotetrameric coiled-coil structure on its own, in the absence of SYCP2 (Syrjänen et al., 2014). The crystal structure revealed a four-stranded antiparallel coiled-coil similar to the expected structure of the SYCP2:SYCP3 heterotetramer (Figure 2.5A). As SYCP3 cannot localize to the chromosome axis without SYCP2, we interpret the SYCP3 homotetramer structure as an in vitro artifact arising from the inherent promiscuity of SYCP3's coiled coil region. We found that M. musculus SYCP3 can also form homotetrameric complexes when expressed on its own in E. coli. When we measured the relative stability of the *M. musculus* SYCP2:SYCP3 heterotetramer and the SYCP3 homotetramer using a fluorescence-based thermal melting assay, we found that the SYCP2:SYCP3 heterotetramer is significantly more stable than the SYCP3 homotetramer. These data strongly suggest that while SYCP3 can form homo-oligomeric complexes on its own, the relevant complex in vivo contains both SYCP2 and SYCP3.

We identified preliminary crystallization conditions for the SYCP2:SYCP3 complex using complexes that were purified from *E. coli* with an N-terminal tag on SYCP2 (Figure 2.4C). In an attempt to improve protein expression, we tested other tag configurations and found that a tag on SYCP3 resulted in much higher yield of purified complex. Given that SYCP3 expresses at much higher levels that SYCP2 in *E. coli*, this was likely a mistake in the sense that the resulting complexes were significantly (if not completely) composed of SYCP3 homotetramers, instead of SYCP2:SYCP3 heterotetramers.

Before realizing that we had inadvertently purified SYCP3 homotetramers, we obtained diffracting crystals of this complex in two different space groups, P1 and $P2_1$. We were initially unable to determine the structure, either by molecular replacement with the existing structure of human SYCP3, or by anomalous phasing methods with selenomethionine or bromide-derivatized crystals. We determined the structure in both crystal forms using the ARCIMBOLDO molecular-replacement program, which uses PHASER and SHELXE to iteratively place and score short alpha-helical segments into a given asymmetric unit, ultimately assembling a near-complete model. With the phases from an initial ARCIMBOLDO model, we identified selenomethionine sites in a 2.5 Å-resolution $P2_1$ dataset and calculated unbiased electron density maps for manual rebuilding of the structure. We used this model to determine the structure of the complex in the P1 form to 2.2 Å.

When we built the structure, we realized that it consisted of four copies of SYCP3, instead of the expected 2:2 tetramer of SYCP2 and SYCP3. Indeed, the structure is almost identical to that of the human SYCP3 tetramer. The four SYCP3 helices coil together to form an anti-parallel assembly roughly 18 nanometers in length. Similarly to the human proteins, mouse SYCP3 contains a stretch of 9 hydrophobic residues in the region from 143-179, which follow a classical heptad-repeat pattern. Residues 161-179 make up the central core of the SYCP3 tetramer, and are stabilized by hydrophobic interactions between F161/L168/F172/F179 (Figure 2.5D). The central coiled-coil core is flanked by two four-helix bundles, which are assembled through hydrophobic packing between residues $Y143_{C/D}$/$F147_{C/D}$/$L151_{C/D}$/$W154_{C/D}$/$I158_{C/D}$ and $M190_{A/B}$/$I193_{A/B}$/$H197_{A/B}$/$F200_{A/B}$/$L204_{A/B}$ (Figure 2.5C). The tetramer is also stabilized near its ends, by hydrophobic interactions between $F118_{C/D}/I125_{C/D}$ and $M226_{A/B}/L229_{A/B}/V233_{A/B}$ (Figure 2.5B).

The major difference between the human and mouse structures is the presence of a loop spanning resides 212-218, which is clearly observed in electron density maps for chains C and D, but is completely disordered in chains A and B. The presence of this loop in the mouse SYCP3 structure results in a shift, offsetting the register of the coiled-coils by a half-register from the human structure near the ends of the complex. This may be a result of our construct being ~20 residues shorter at its C-terminus than the crystallized human construct, which could destabilize the ends of our coiled-coil structure.

To ultimately determine the crystal structure of the SYCP2:SYCP3 tetramer, we will pursue several strategies. First, we will return to my initial purification scheme with tagged SYCP2, from which we obtained preliminary crystals, and optimize these crystals further. Next, we will express and purify the equivalent constructs of human SYCP2 and SYCP3, and screen for crystallization conditions after confirming complex stoichiometry by SEC-MALS and mass spectrometry. Finally, I have designed several end-to-end fusions of SYCP2 and SYCP3. Since SYCP2 and SYCP3 are likely anti-parallel in the heterotetramer, a fusion of the coiled-coil regions of SYCP2 and SYCP3, with a flexible linker between them, should form a homodimer with a structure equivalent to the native heterotetramer. This scheme disallows formation of SYCP3 homotetramers, providing significant advantages over the strategy of co-expression, which in any case could result in a mixture of resultant complexes. We will next purify these constructs and determine their oligomeric state by SEC-MALS before screening for crystallization conditions.

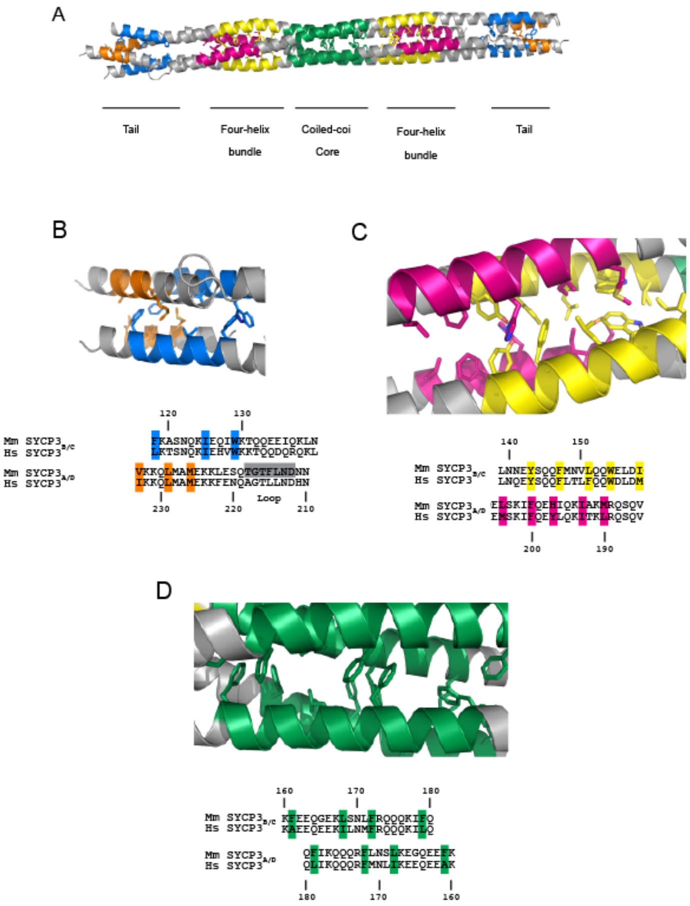

## Figure 2.5 Structure of SYCP3 tetramer

(A) Overall structure of the SYCP3 tetramer, outlining the coiled-coil core, the four-helix bundle arms, and the coiled-coil tails. (B) Zoom in of the coiled-coil tail, with chains B/C in blue and chains A/D in orange. (C) Outline of the four-helix bundle arms, with chains B/C in yellow and chains A/D in pink. (D) outline of the central coiled-coil, containing overlapping regions from chains A/B/C/D in green.

## 2.4 Discussion

SYCP2 and SYCP3's roles as foundational elements of the chromosome axis remain mostly unknown. Here we present a structural and biochemical characterization of *M. musculus* SYCP2 and SYCP3, highlighting a molecular mechanism for how these proteins work together to organize meiotic chromosomes and promote homologous recombination. We found that the C-terminal coiled-coil domains of SYCP2 and SYCP3 can associate to form large filament or fiber-like structures in vitro. We also show that these filaments are assembled through oligomerization of a tetrameric complex formed by SYCP2 and SYCP3. Based on length and stoichiometry of the SYCP2:SYCP3 tetramer we isolated, we hypothesize the structure formed by these proteins will be highly similar to the structure of the SYCP3 homotetramer reported by(Syrjänen et al., 2014). In this study we also identify a HORMAD binding motif in the disordered region of SYCP2. Taken together, these results begin to outline a network of interactions that make up the major components of the mammalian axial element, and provide insight into how these structures organize meiotic chromosomes to facilitate pairing and recombination between homologous chromosomes.

Meiotic chromosomes' ability to undergo recombination and segregate properly is dependent on their structure and organization into a linear array of loops (Blat et al., 2002) (Kleckner, 2006). Sister chromatid cohesion is established in premeiotic S-phase, when meiosis-specific REC8-containing cohesin complexes can be visualized assembling into short axial elements along chromosomes, assembling the foundation of the loop axis structure (Eijpe et al., 2003). Previous work showing that deletion of

SYCP2 or SYCP3 has significant effects on chromatin compaction and DNA loop formation in meiosis suggest these proteins play important roles in organizing the cohesin-based axis that assembles from S phase through leptotene (Kolas et al., 2004; Kouznetsova, 2005; Novak et al., 2008). SYCP2 and SYCP3 are deposited onto chromosomes simultaneously at the onset of leptotene, co-localizing with cohesin complexes (Eijpe et al., 2003; Prieto et al., 2001). If the SYCP2:SYCP3 complex can physically associate with the pre-established axis, then oligomerization of these complexes could explain how these proteins are responsible for compacting the chromatin and generating continuous cohesin staining patterns. We propose a model, where SYCP2 and SYCP3 coalesce the loop-extruding core of the chromosome axis into a highly compacted linear array through their oligomerization (figure).

The next major question to address will be how SYCP2 is recruited to chromosomes. A few lines of reasoning support the idea that the N-terminal domain of SYCP2 is responsible for localizing SYCP2:SYCP3 complexes to chromosomes, potentially through direct binding to cohesin complexes. First, SYCP2 constructs lacking the C-terminal coiled-coil can localize to chromosomes in punctate patterns, while SYCP3 is completely lost from chromosomes in the absence of this domain (Yang et al., 2006). Second, SYCP3 axis patterning depends on cohesin complexes, and SYCP2/SYCP3 been shown to immunoprecipitate with cohesin subunits in rats (Eijpe et al., 2000; Llano et al., 2012; Winters et al., 2014). Finally, the N-terminal domain of SYCP2 has already been implicated in linking it to chromatin through centromeres (Feng et al., 2017), although this is unlikely to be the only mechanism responsible for axis localization. These results suggest independent roles for the N- and C-terminal domains of SYCP2, with the C-terminus being involved in generating a continuous linear axis, and the N-terminus being important for axis localization. Identifying potential axis-associated binding partners for the SYCP2 N-terminal domain will be an important step in outlining SYCP2 function and chromosome axis architecture.

Identification of the HORMAD closure-motif in SYCP2 outlines another mechanism of mammalian AE assembly and organization, and explains some of the HORMAD localization phenotypes seen in SYCP2/3 mutants (Fukuda et al., 2010; Shin et al., 2010). Red1 has well-established roles in meiotic checkpoint signaling and interhomolog bias during the DNA repair pathway through its interactions with Hop1 and checkpoint kinases (Eichinger and Jentsch, 2010; K. P. Kim et al., 2010). Our data supports the idea that SYCP2 and SYCP3 are more than just structural elements of the axis, and are likely involved in these processes through their recruitment and interplay with the meiotic HORMAD proteins (Li et al., 2011).

The discovery of SYCP2's ability to oligomerize through its C-terminal coiled-coil and the presence of a HORMAD recruitment motif illuminate more functional parallels between SYCP2 and Red1, and provide a possible mechanism for how the chromosome axis is assembled. Determining the molecular basis for SYCP2/3 recruitment to the chromosomes will be an important step in further outlining the architecture of the chromosome axis. How potential kinases that work in conjunction with SYCP2 and the meiotic HORMADs could also be an important question in outlining the function of the axial element in meiotic prophase.

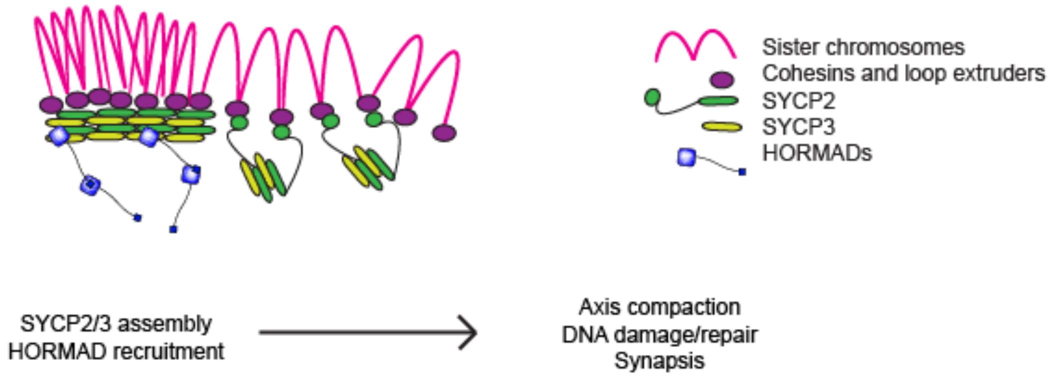

**Figure 2.6 Model of mammalian axial element assembly and organization.**

## 2.5 Experimental Procedures

### 2.5.1 Protein Expression and Purification

Coding sequences for *M. Mus.* SYCP2 and SYCP3 were cloned into Berkeley MacroLab *E. coli* T7 expression vectors containing N-terminal His6-(Maltose binding protein)-tev, His6-Sumo-tev, and no tag vectors using Gibson assembly and ligation independent cloning. For purification of the SYCP2:SYCP3 fibers, His6-MBP-tev-SYCP2 (1325-1500) and No tag-SYCP3(84-248) were co-transformed into Rosetta (DE3) pLysS cells, and grown to O.D.600 of 0.9 at 37C before inducing with 250 mM IPTG at 18C. Cells were purified from cell lysates using Ni2+ resin (HisTrap HP: GE Life Sciences), ion exchange (HiTrap SP or Q: GE Life Sciences), and size exclusion chromatography (Superdex200: GE Life Sciences). The different N- and C-terminal truncations of SYCP2 and SYCP3 were expressed and purified similarly, and analyzed over a 24 mL Superose6 column (GE Life Sciences).

Calculation of the molecular weight of MBP-SYCP2(1325-1479):SYCP3(105-248) was performed using size-exclusion chromatography coupled to multi-angle light scattering (SEC-MALS). Proteins were separated using a Superdex200 10/300 GL size exclusion column (GE Life Sciences), their refractive index and light scattering profiels were collected by Optilab T-rEX and miniDAWN TREOS detectors (Wyatt Technology). The molecular weight of this complex was calculated using ASTRA v.6 software (Wyatt Technology).

For co-expression of *M. Mus* HORMAD2 and SYCP2 truncations, HORMAD2 (2-241) coding sequence was amplified and cloned into a T7 polycistronic co-expression vector with truncations of SYCP2 (390-429) N-terminally tagged by His6-MBP-Tev.

These complexes were purified from cell lysates using a Ni2+ (HisTrap HP: GE Life Sciences) column, and visualized using SDS-PAGE gels and coomassie stain.

### 2.5.2 Negative Stain Electron Microscopy

For negative-stain EM, MBP-SYCP2(1325-1500):SYCP3(84-248) and SYCP2(1325-1500):SYCP3(84-248) were passed over a size exclusion column (Superdex200 GE Life Sciences) in EM buffer (300 mM NaCl, 20 mM Tris7.5, 1 mM DTT), and peak fractions were diluted to ~0.01 mg/mL in EM buffer. Samples were added to freshly glow discharged carbon coated copper grids, blotted into a thin film, and negatively stained by a 2% solution of uranyl formate, repeating this process three times. Data were acquired using a Tecnai F20 Twin transmission electron microscope (FEI, Hillsboro OR) operating at 200 kV. Images were automatically collected using the LEGINON system (Suloway et al. 2005). Images were taken using a Tietz F416 4K x 4k pixel CMOS camera (TVIPS, Gauting, Germany). MBP tagged samples were analyzed using ImageJ to determine the average spacing between MBP's on the SYCP2:SYCP3 filaments.

### 2.5.3 Yeast two-hybrid assay

Sequences for *M. Musculus* HORMAD1, HORMAD2, SYCP2, and SYCP3 were cloned into pGADT7 (Gal4 activation domain fused: "AD") and pBridge (Gal4 binding domain fused: "BD") vectors (Clontech Laboratories, Mountain View CA). Plasmids were transformed into AH109 and Y187 yeast strains, and transformants were selected using

CSM –Leu (pGADT7) and CSM –Trp (pBridge) dropout plates. The haploid yeast strains were mated overnight at room temperature, and diploids were selected using CSM –Lue-Trp dropout plates. Diploids were patched onto low stringency plates (CSM –Trp-Leu-His) and high stringency plates (CSM –Trp-Leu-His-Ade), grown for 3 days at 30C, and imaged.

### 2.5.4 Structure Determination

*M. Musculus* SYCP3 was crystalized at !6% PEG4000, 100 mM Tris pH8.5, and 100 mM NaoAc. Thin square plate crystals were cryoprotected by the addition of 20% sucrose and 18% PEG4000, then diffraction data was collected at XXX. Despite identical growth conditions and similar shape, crystals belonged to two different space groups (P1 and $P2_1$; **Table S2.1**). An initial model was generated by ARCIMBOLDO using a merged $P2_1$ dataset assembled from three individual datasets from different crystals, cut to a final resolution of 2.5 Å. ARCIMBOLDO uses PHASER and SHELXE to place individual $\alpha$-helices by molecular replacement, then assemble individual fragments into a complete model. Phases from the initial ARCIMBOLDO model (393 residues) were used to identify selenomethionine sites, which were then supplied to the Phenix Autosol module for phase calculation in PHASER, density modification including two-fold NCS averaging in RESOLVE, and initial model building in RESOLVE. Initial models from ARCIMBOLDO and RESOLVE were manually rebuilt in COOT and refined in phenix.refine. A partially-refined model was used to determine the P1 structure by molecular replacement in PHASER.

## 2.6 Supplemental Data

### Table S2.1 - Data Collection and Refinement Statistics

| | SYCP3 tetramer P21 | SYCP3 tetramer P1 |
|---|---|---|
| **Data collection** | | |
| Dataset identifier | 1536_6_1 | Five P1 datasets |
| Synchrotron/Beamline | APS 24ID-E | |
| Resolution (Å) | 50 – 2.5 | 50 – 2.2 |
| Wavelength (Å) | 0.9793 | |
| Space Group | $P2_1$ | P1 |
| Unit Cell Dimensions (a, b, c) Å | 45.89, 49.49, 150.56 | 45.84, 52.41, 75.33 |
| Unit cell Angles ($\alpha,\beta,\gamma$) ° | 90, 90.792, 90 | 94.73, 103.98, 110.47 |
| $I/\sigma$ (last shell) | 5.26 (0.58) | 10.4 (1.17) |
| [b] $R_{meas}$ (last shell) | 0.138 (2.26) | 0.119 (1.95) |
| [c] $CC_{1/2}$, last shell | 0.703 | 0.758 |
| Completeness (last shell) % | 98.7 (98.6) | 99.6 (96.3) |
| Number of reflections | 157780 | 405686 |
| *unique* | 45316 | 31847 |
| Multiplicity | 3.5 | 12.7 |
| Number of sites | 28 | – |
| **Refinement** | | |
| | Refine_8 | Refine_12 |
| Resolution (Å) | 50 – 2.5 | 50 – 2.2 |
| No. of reflections | 44896 (anomalous) | 31512 |
| *working* | 42510 | 30041 |
| *free* | 2386 | 1471 |
| [e] $R_{work}$ (%) | 30.11 | 30.83 |
| [e] $R_{free}$ (%) | 36.38 | 36.31 |
| **Structure/Stereochemistry** | | |
| Number of atoms | 3945 | 4017 |
| *non-hydrogen* | 3945 | 4017 |
| *solvent* | 2 | 19 |
| r.m.s.d. bond lengths (Å) | 0.010 | 0.007 |
| r.m.s.d. bond angles (°) | 0.957 | 0.772 |
| [f] PDB ID | | |
| [g] SBGrid Data Bank ID | | |

[b] $R_{meas} = \sum_h [ \sqrt{(n/(n-1))} \sum_j [I_{hj} - \langle I_h \rangle] / \sum_{hj} \langle I_h \rangle$
where $I_{hj}$ is a single intensity measurement for reflection h, $\langle I_h \rangle$ is the average intensity measurement for multiply recorded reflections, and $n$ is the number of observations of reflection h.

[c] $CC_{1/2}$ is the Pearson correlation coefficient between the average measured intensities of two randomly-assigned half-sets of the measurements of each unique reflection (5).

[e] $R_{work,\ free} = \sum||F_{obs}| - |F_{calc}||/|F_{obs}|$, where the working and free $R$-factors are calculated using the working and free reflection sets, respectively.

[f] Coordinates and structure factors have been deposited in the RCSB Protein Data Bank (www.pdb.org) and are awaiting an accession number.

[g] Diffraction data have been deposited with the SBGrid Data Bank (https://data.sbgrid.org) and are awaiting an accession number.

## 2.7 References

Baier, A., Alsheimer, M., Volff, J.N., Benavente, R., 2007. Synaptonemal Complex Protein SYCP3 of the Rat: Evolutionarily Conserved Domains and the Assembly of Higher Order Structures. Sex Dev 1, 161–168. doi:10.1159/000102105

Blat, Y., Protacio, R.U., Hunter, N., Kleckner, N., 2002. Physical and Functional Interactions among Basic Chromosome Organizational Features Govern Early Steps of Meiotic Chiasma Formation. Cell 111, 791–802. doi:10.1016/S0092-8674(02)01167-4

Börner, G.V., Barot, A., Kleckner, N., 2008. Yeast Pch2 promotes domainal axis organization, timely recombination progression, and arrest of defective recombinosomes during meiosis. Proc. Natl. Acad. Sci. U.S.A. 105, 3327–3332. doi:10.1073/pnas.0711864105

Eichinger, C.S., Jentsch, S., 2010. Synaptonemal complex formation and meiotic checkpoint signaling are linked to the lateral element protein Red1. Proceedings of the National Academy of Sciences 107, 11370–11375. doi:10.1073/pnas.1004248107

Eijpe, M., Heyting, C., Gross, B., Jessberger, R., 2000. Association of mammalian SMC1 and SMC3 proteins with meiotic chromosomes and synaptonemal complexes. J. Cell. Sci. 113 ( Pt 4), 673–682.

Eijpe, M., Offenberg, H., Jessberger, R., Revenkova, E., Heyting, C., 2003. Meiotic cohesin REC8 marks the axial elements of rat synaptonemal complexes before cohesins SMC1beta and SMC3. J. Cell Biol. 160, 657–670. doi:10.1083/jcb.200212080

Feng, J., Fu, S., Cao, X., Wu, H., Lu, J., Zeng, M., Liu, L., Yang, X., Shen, Y., 2017. Synaptonemal complex protein 2 (SYCP2) mediates the association of the centromere with the synaptonemal complex. Protein Cell 8, 538–543. doi:10.1007/s13238-016-0354-6

Ferdous, M., Higgins, J.D., Osman, K., Lambing, C., Roitinger, E., Mechtler, K., Armstrong, S.J., Perry, R., Pradillo, M., Cuñado, N., Franklin, F.C.H., 2012. Inter-homolog crossing-over and synapsis in Arabidopsis meiosis are dependent on the chromosome axis protein AtASY3. PLoS Genet. 8, e1002507. doi:10.1371/journal.pgen.1002507

Fukuda, T., Daniel, K., Wojtasz, L., Toth, A., Höög, C., 2010. A novel mammalian HORMA domain-containing protein, HORMAD1, preferentially associates with unsynapsed meiotic chromosomes. Exp. Cell Res. 316, 158–171. doi:10.1016/j.yexcr.2009.08.007

Kim, K.P., Weiner, B.M., Zhang, L., Jordan, A., Dekker, J., Kleckner, N., 2010. Sister cohesion and structural axis components mediate homolog bias of meiotic recombination. Cell 143, 924–937. doi:10.1016/j.cell.2010.11.015

Kim, Y., Rosenberg, S.C., Kugel, C.L., Kostow, N., Rog, O., Davydov, V., Su, T.Y., Dernburg, A.F., Corbett, K.D., 2014. The Chromosome Axis Controls Meiotic Events through a Hierarchical Assembly of HORMA Domain Proteins. Dev. Cell 31, 487–502. doi:10.1016/j.devcel.2014.09.013

Kleckner, N., 2006. Chiasma formation: chromatin/axis interplay and the role(s) of the synaptonemal complex. Chromosoma 115, 175–194. doi:10.1007/s00412-006-0055-7

Klein, F., Mahr, P., Galova, M., Buonomo, S.B., Michaelis, C., Nairz, K., Nasmyth, K., 1999. A central role for cohesins in sister chromatid cohesion, formation of axial elements, and recombination during yeast meiosis. Cell 98, 91–103. doi:10.1016/S0092-8674(00)80609-1

Kolas, N.K., Yuan, L., Höög, C., Heng, H.H.Q., Marcon, E., Moens, P.B., 2004. Male mouse meiotic chromosome cores deficient in structural proteins SYCP3 and SYCP2 align by homology but fail to synapse and have possible impaired specificity of chromatin loop attachment. Cytogenet Genome Res 105, 182–188. doi:10.1159/000078188

Kouznetsova, A., 2005. SYCP2 and SYCP3 are required for cohesin core integrity at diplotene but not for centromere cohesion at the first meiotic division. J. Cell. Sci. 118, 2271–2278. doi:10.1242/jcs.02362

Lambing, C., Osman, K., Nuntasoontorn, K., West, A., Higgins, J.D., Copenhaver, G.P., Yang, J., Armstrong, S.J., Mechtler, K., Roitinger, E., Franklin, F.C.H., 2015. Arabidopsis PCH2 Mediates Meiotic Chromosome Remodeling and Maturation of Crossovers. PLoS Genet. 11, e1005372. doi:10.1371/journal.pgen.1005372

Lammers, J.H., Offenberg, H.H., van Aalderen, M., Vink, A.C., Dietrich, A.J., Heyting, C., 1994. The gene encoding a major component of the lateral elements of synaptonemal complexes of the rat is related to X-linked lymphocyte-regulated genes. Mol. Cell. Biol. 14, 1137–1146. doi:10.1128/MCB.14.2.1137

Li, X.C., Bolcun-Filas, E., Schimenti, J.C., 2011. Genetic evidence that synaptonemal complex axial elements govern recombination pathway choice in mice. Genetics 189, 71–82. doi:10.1534/genetics.111.130674

Llano, E., Herrán, Y., García-Tuñón, I., Gutiérrez-Caballero, C., de Álava, E., Barbero, J.L., Schimenti, J., de Rooij, D.G., Sánchez-Martín, M., Pendás, A.M., 2012. Meiotic cohesin complexes are essential for the formation of the axial element in mice. J. Cell Biol. 197, 877–885. doi:10.1083/jcb.201201100

Novak, I., Wang, H., Revenkova, E., Jessberger, R., Scherthan, H., Höög, C., 2008. Cohesin Smc1beta determines meiotic chromatin axis loop organization. J. Cell Biol.

180, 83–90. doi:10.1083/jcb.200706136

Offenberg, H., 1998. SCP2: a major protein component of the axial elements of synaptonemal complexes of the rat. Nucleic Acids Res. 26, 2572–2579. doi:10.1093/nar/26.11.2572

Page, S.L., Hawley, R.S., 2004. THE GENETICS AND MOLECULAR BIOLOGY OF THE SYNAPTONEMAL COMPLEX. Annu. Rev. Cell Dev. Biol. 20, 525–558. doi:10.1146/annurev.cellbio.19.111301.155141

Panizza, S., Mendoza, M.A., Berlinger, M., Huang, L., Nicolas, A., Shirahige, K., Klein, F., 2011. Spo11-accessory proteins link double-strand break sites to the chromosome axis in early meiotic recombination. Cell 146, 372–383. doi:10.1016/j.cell.2011.07.003

Pelttari, J., Hoja, M.R., Yuan, L., Liu, J.G., Brundell, E., Moens, P., Santucci-Darmanin, S., Jessberger, R., Barbero, J.L., Heyting, C., Höög, C., 2001. A meiotic chromosomal core consisting of cohesin complex proteins recruits DNA recombination proteins and promotes synapsis in the absence of an axial element in mammalian meiotic cells. Mol. Cell. Biol. 21, 5667–5677. doi:10.1128/MCB.21.16.5667-5677.2001

Prieto, I., Suja, J.A., Pezzi, N., Kremer, L., Martínez-A, C., Rufas, J.S., Barbero, J.L., 2001. Mammalian STAG3 is a cohesin specific to sister chromatid arms in meiosis I. Nat. Cell Biol. 3, 761–766. doi:10.1038/35087082

Shin, Y.-H., Choi, Y., Erdin, S.U., Yatsenko, S.A., Kloc, M., Yang, F., Wang, P.J., Meistrich, M.L., Rajkovic, A., 2010. Hormad1 mutation disrupts synaptonemal complex formation, recombination, and chromosome segregation in mammalian meiosis. PLoS Genet. 6, e1001190. doi:10.1371/journal.pgen.1001190

Smith, A.V., Roeder, G.S., 1997. The yeast Red1 protein localizes to the cores of meiotic chromosomes. J. Cell Biol. 136, 957–967. doi:10.1083/jcb.136.5.957

Syrjänen, J.L., Pellegrini, L., Davies, O.R., 2014. A molecular model for the role of SYCP3 in meiotic chromosome organisation. Elife 3, 213. doi:10.7554/eLife.02963

Tarsounas, M., Pearlman, R.E., Gasser, P.J., Park, M.S., Moens, P.B., 1997. Protein-protein interactions in the synaptonemal complex. Mol. Biol. Cell 8, 1405–1414. doi:10.1091/mbc.8.8.1405

Wan, L., 2003. Mek1 Kinase Activity Functions Downstream of RED1 in the Regulation of Meiotic Double Strand Break Repair in Budding Yeast. Mol. Biol. Cell 15, 11–23. doi:10.1091/mbc.E03-07-0499

Wang, K., Wang, M., Tang, D., Shen, Y., Qin, B., Li, M., Cheng, Z., 2011. PAIR3, an axis-associated protein, is essential for the recruitment of recombination elements onto meiotic chromosomes in rice. Mol. Biol. Cell 22, 12–19. doi:10.1091/mbc.E10-08-0667

Winters, T., McNicoll, F., Jessberger, R., 2014. Meiotic cohesin STAG3 is required for chromosome axis formation and sister chromatid cohesion. EMBO J. 33, 1256–1270. doi:10.1002/embj.201387330

Wojtasz, L., Daniel, K., Roig, I., Bolcun-Filas, E., Xu, H., Boonsanay, V., Eckmann, C.R., Cooke, H.J., Jasin, M., Keeney, S., McKay, M.J., Toth, A., 2009. Mouse HORMAD1 and HORMAD2, two conserved meiotic chromosomal proteins, are depleted from synapsed chromosome axes with the help of TRIP13 AAA-ATPase. PLoS Genet. 5, e1000702. doi:10.1371/journal.pgen.1000702

Woltering, D., Baumgartner, B., Bagchi, S., Larkin, B., Loidl, J., de los Santos, T., Hollingsworth, N.M., 2000. Meiotic segregation, synapsis, and recombination checkpoint functions require physical interaction between the chromosomal proteins Red1p and Hop1p. Mol. Cell. Biol. 20, 6646–6658. doi:10.1128/MCB.20.18.6646-6658.2000

Yang, F., La Fuente, De, R., Leu, N.A., Baumann, C., McLaughlin, K.J., Wang, P.J., 2006. Mouse SYCP2 is required for synaptonemal complex assembly and chromosomal synapsis during male meiosis. J. Cell Biol. 173, 497–507. doi:10.1083/jcb.200603063

Yuan, L., Liu, J.-G., Zhao, J., Brundell, E., Daneholt, B., Höög, C., 2000. The Murine SCP3 Gene Is Required for Synaptonemal Complex Assembly, Chromosome Synapsis, and Male Fertility. Mol. Cell 5, 73–83. doi:10.1016/S1097-2765(00)80404-9

Yuan, L., Pelttari, J., Brundell, E., Björkroth, B., Zhao, J., Liu, J.-G., Brismar, H., Daneholt, B., Höög, C., 1998. The Synaptonemal Complex Protein SCP3 Can Form Multistranded, Cross-striated Fibers In Vivo. J. Cell Biol. 142, 331–339. doi:10.1083/jcb.142.2.331

# Chapter 3: Hi-C analysis of genome organization in mouse spermatocytes during prophase

## 3.1 Summary

The meiotic homologous recombination pathway requires a unique organization of chromatin into a linear array of DNA loops coordinated by the chromosome axis. While there has been an explosion of next generation sequencing techniques used to study genome organization in a wide variety of cell types and developmental stages, these methods have not been applied to meiotic cells. Here we present a preliminary study using a chromosome conformation capture technique, called Hi-C, to examine the organization of the meiotic genome in highly synchronized populations of zygotene and pachytene stage mouse spermatocytes. We are able to observe hallmark structural features of the meiotic genome, such as XY body formation and the formation of a chromosomal “bouquet”. Alongside these global characteristics, we also find that the topological associated domains (TADs) found in interphase chromosomes are also present in the local architecture of meiotic prophase chromosomes. Our preliminary results reveal the potential for Hi-C as a powerful tool to investigate meiotic genome organization, and set the stage for future studies to examine the fine structure of individual meiotic chromosomes directly detect inter-homolog interactions during meiotic recombination, and examine the effect of chromosome axis mutants on the architecture of the chromosomes themselves.

## 3.2 Introduction

While earlier chapters of this dissertation have described new insights into the architecture and function of the chromosome axis, the underlying chromosome structure imposed by the axis remains mostly mysterious. The structure of the chromosome itself is important to study, as this has important implications for pairing of homologs and recombination pathway decisions. Early EM studies of meiotic chromosomes revealed a linear array of chromatin loops extending from the chromosome axis, but how this loop-array structure is enforced onto the chromosomes, as well as how this structure is related to chromosome organization in somatic cells, is unknown.

The recent development of “chromatin conformation capture,” coupled with advances in next-generation sequencing technologies, have enabled the examination of the genome’s 3-dimensional organization and folding at unprecedented resolution (Dekker, 2002; Dixon et al., 2012; Lieberman-Aiden et al., 2009). Chromosome conformation capture (3C, known as Hi-C when coupled with high-throughput sequencing) detects pairs of DNA loci that are in close physical proximity in the nucleus, regardless of their genetic location. The resulting data reveals the “interaction frequency” between each pair of loci in the genome at high resolution (<10 kb in recent studies), in certain cases enabling the construction of 3D models of the genome (Varoquaux et al., 2014). Hi-C has recently been used to probe the structure of mammalian chromosomes in both interphase and in mitosis, and in a number of different environmental, developmental, or mutant states. This has allowed an unprecedented view of mammalian genome organization in somatic cells.

Early work using fluorescence in situ-hybridization (FISH) established that interphase chromosomes segregate into “territories”; that is, each chromosome generally occupies its own physical space in the nucleus (Manuelidis, 1985) (Schardin et al., 1985) (Cremer et al., 2008). At the same time, biochemical and structural work established the nucleosome as the fundamental structural unit of chromatin, and showed how higher-order chromatin filaments or fibers might assemble (Cutter and Hayes, 2015). Until the development of chromosome conformation capture, however, a global view of genome architecture linking these two different scales was lacking. Hi-C and related techniques have subsequently identified several levels of genome architecture, including (from smallest to largest) loops, topological-associated domains (TADs; also referred to as domains), and compartments that correspond to transcriptionally active and inactive regions (Dixon et al., 2012; Lieberman-Aiden et al., 2009; Nora et al., 2012).

The first Hi-C analyses of mammalian chromosomes identified TADs and compartments. TADs are continuous regions of high local contact frequency, separated by sharp boundaries, across which contacts rarely occur. TADs can range in size from 100 kb to several megabases, with an average size of 1 MB, although these can vary across organisms (Dixon et al., 2012; Nora et al., 2012). Organization of chromatin into TADs has been shown to depend on structural maintenance of chromosome (SMC)-family cohesin complexes and the insulator protein CTCF (Hansen et al., 2017; Rao et al., 2017; Schwarzer et al., 2017). Based on modeling and mutational data, the predominant view for how TADs arise is that in each cell, loops ~100 kb in size are generated by processive loop-extruding enzymes (potentially cohesin complexes), with loop extrusion inhibited by CTCF proteins bound to the chromosome in a certain orientation (Rao et al., 2014). Simulations modeling loop-extruding enzymes constrained by CTCF binding sites have reproduced TAD structures very similar to what is seen in experimental Hi-C analysis (Fudenberg et al., 2016; Hofmann and Heermann, 2015). More recent high-resolution Hi-C analyses have directly detected individual loops, including stable loops that can be detected in cell populations (Eagen et al., 2017; Phanstiel et al., 2017), and more transient/stochastic loops that are detected in single-cell Hi-C data (Flyamer et al., 2017; Stevens et al., 2017). The origins of the larger-scale compartments, which also correlate with R/G bands, GC content, and transcriptional status, are less well-understood, but tethering of specific loci to the nuclear periphery is likely involved (Carvalho et al., 2001). Finally, very recent analyses have clarified how nuclear features like the nucleolus and nuclear speckles contribute to genome architecture through recruitment of certain loci (rDNA and transcriptionally-active regions, respectively) to specific intra-nuclear compartments, regardless of their location in the genome (Quinodoz et al., 2017).

Alongside analysis of genome architecture in interphase, other work has elucidated the principles for assembly and compaction of mitotic chromosomes. In cells entering mitosis, cohesin complexes on chromosome arms are exchanged for related condensin complexes (Losada et al., 2000) (Sumara et al., 2000) (Waizenegger et al., 2000), and the chromosomes undergo a significant compaction and linear organization. Hi-C analysis has shown that TAD and compartment structures disappear as chromosomes are compacted, and modeling has indicated that this is likely due to the organization of the chromosome into a linear array of loops contrained by, and perhaps also generated by, the condensin complexes (Naumova et al., 2013) (Terakawa et al., 2017).

While chromosome conformation capture has been widely used to map genome organization in a variety of somatic and mitotic cell types, this technique has not been used to probe meiotic genome organization. Meiotic prophase chromosomes are structurally distinct from those of somatic cells, and this unique architecture contributes to the homologous pairing and recombination required for accurate meiotic chromosome segregation (Padmore et al., 1991; Winters et al., 2014). The chromosome axis controls and recruits the recombination machinery, and acts as a scaffold for later assembly of the synaptonemal complex, which serves to closely juxtapose homologs along their entire lengths (Page and Hawley, 2004). Meiotic prophase proceeds along a defined route that has been divided into four substages (figure 3.2A) (Baudat et al., 2013). In leptotene, the chromosome axis can be visualized as proteins begin to assemble into short linear stretches or foci between sister chromosomes. The chromosome axis becomes contiguous in zygotene, and synapsis initiates as transverse filaments begin connecting the chromosome axes of paired homologs. Pachytene is the longest stage of prophase, where synapsis and recombination complete, resulting in the formation of chiasmata between homologs. In diplotene, the synaptonemal complex dissociates, cohesin is exchanged for condensin, and the chromosomes become highly compacted during the prophase-metaphase transition.

This chapter outlines preliminary Hi-C analysis of genome architecture in mouse spermatocyte samples synchronized in either zygotene or pachytene of meiotic prophase. While our analysis is currently incomplete, we observe hallmarks of well-known chromosome morphological features in prophase, including the clustering of telomeres at the nuclear envelope into a “chromosomal bouquet”, and the compaction and segregation of the X and Y chromosomes into the sex body. The local chromosome architecture in both stages appears to contain TADs defined by highly conserved boundary elements seen in many human and mouse cell lines (Darrow et al., 2016) (Rao et al., 2014). We show that Hi-C is a powerful tool in exploring the organization of the meiotic genome, which holds strong promise for better understanding the roles of chromosome-associated proteins in meiotic genome organization and recombination.

## 3.3 Results

### 3.3.1 Hi-C analysis of mouse spermatocytes in meiotic prophase

To analyze the architecture of meiotic chromosomes and also detect inter-homolog interactions, we crossed male C57BL/6J and female CAST/EiJ mice to generate male F1 hybrids whose homologous chromosomes contain a high density of single-nucleotide polymorphisms (SNPs; ~0.75% single-nucleotide polymorphism density) (Keane et al., 2011) (Figure 3.1A). This high SNP density should enable haplotype-specific mapping of a high proportion of sequence reads, allowing us to distinguish between intra- and inter-homolog interactions. We synchronized spermatogenesis using a recently-developed method taking advantage of the dependence of spermatogenesis on retinoic acid (Hogarth and Griswold, 2013), then sacrificed mice and collected spermatocytes (Figure 3.1B). Cells were stained with Hoechst 33342, and fluorescence-assisted cell sorting (FACS) was used to isolate highly pure populations of cells in zygotene and pachytene (Cole et al., 2014) (Figure 3.1C). Cell populations were tested for purity by staining for the axis component SYCP3 and the linker histone H1T, which is a marker for pachytene chromosomes (Figure 3.1C, Table S3.1). Purified cell populations were cross-linked and prepared for Hi-C analysis according to standard methods (van Berkum et al., 2010), using the restriction enzyme MboI (Figure 3.1D). We performed Hi-C analysis on two zygonema samples and one pachynema sample, each containing 600,000-800,000 cells. Each sample was sequenced in a full lane of an Illumina Hi-Seq 4000, set to perform 100 bp paired-end sequencing. We used the publicly available HiC-Pro software pipeline to process our data (Servant et al., 2015). The first step in Hi-C pro is using alignment software, in this case Bowtie2, to align our raw paired-end sequencing reads to a reference genome, creating a list of valid interaction products (Langmead and Salzberg, 2012). HiC-Pro then generates contact maps that we use to visualize genomic interaction frequencies. Bowtie2 mapped ~60% of the total processed reads as unique read pairs, resulting in 170-220 million reads for each of our samples (Table S3.2).

One of the major goals of this project was to use allele-specific mapping to generate inter-homolog contact maps, and obtain high-resolution information about homolog pairing and recombination in meiosis. Given the high SNP density of the F1 hybrid mouse cells used, ~53% of individual 100-bp reads are likely mappable to a unique haplotype (probability of NOT observing a SNP in a 100-bp read = (1-0.0075)^100 = 0.47). When considering paired-end reads, ~78% are likely mappabe to a unique haplotype on at least one end (probability of NOT observing a SNP in 200 bp = (1-0.0075)^200 = 0.22), and ~28% are expected to map to a unique haplotype on both ends (0.53^2 = 0.28). We initially attempted allele-specific mapping using the HiC-Pro pipeline (Servant et al., 2015). Sequence reads were aligned to the reference C57BL/6 genome, for which all polymorphic nucleotides in the Cast/EiJ genome were N-masked, preventing systematic bias in aligning reads to the reference allele in favor of non-reference alleles (Quinlan et al., 2010). HiC-Pro browses reads containing polymorphic sites, identifies the SNP, and assigns the read to either the maternal or paternal allele. Although this method initially appeared to be effective, we noticed that HiC-Pro uniquely mapped ~7% of Y-chromosome reads to the CAST/EiJ genome, despite the Y-chromosome in these mice originating from the C57Bl/6 male parental mouse. Since only 2% of all our reads were identifiable as inter-homolog reads, this 7% represented a read mapping bias resulting in a significant amount of false positives. Thus, a new allele-specific mapping procedure will be required to confidently analyze inter-homolog interactions (see Discussion). Nonetheless, we have performed initial Hi-C analysis using the mapped (but not haplotype-assigned) reads for each dataset.

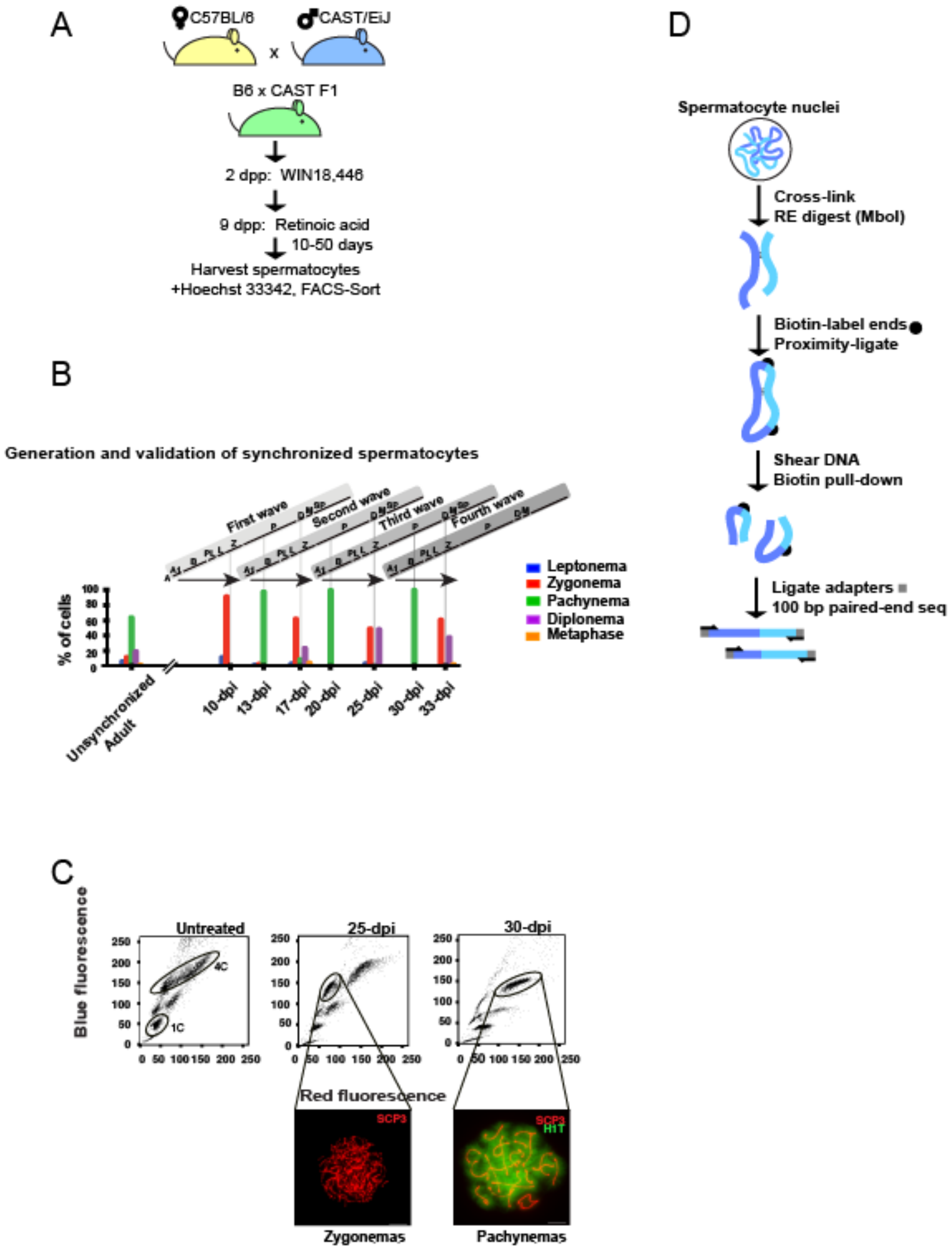

**Figure 3.1 Synchronization of mouse spermatocytes**

(A) Generation of high SNP density B6 x CAST F1 hybrid mouse. (B) Spermatocyte synchronization, cells harvested days post injection (DPI) of retinoic acid. (C) FACS sorting and validation of synchronized spermatocyte purity. (D) Outline of Hi-C procedure.

### 3.3.2 Visualization of meiotic bouquet configuration and telomere clustering

In most eukaryotes, dynamic chromosome movements in prophase I are important for establishing accurate homolog pairing (Koszul and Kleckner, 2009). Chromosome's telomeres become clustered at the nuclear envelope in a "bouquet configuration", and linked to extra-nuclear motors through the transmembrane SUN/KASH domain family of proteins (Starr, 2009; Starr and Fischer, 2005; Tzur et al., 2006). The shuffling and rearranging of chromosomes through these motions is thought to promote homology searching, and disrupt connections between non-homologous chromosomes (Koszul et al., 2008; Wanat et al., 2008; Zickler and Kleckner, 1998). These dynamic chromosome movements have been shown to persist until late prophase, with chromosome dynamics significantly slowing down by diplotene and SUN1 accumulation at telomeres diminishing by late pachytene (Shibuya et al., 2014).

One of the most noticeable features in our global Hi-C contact maps is the X-shaped pattern present in the trans-interaction or inter-chromosomal contact plots (Figure 3.2B). This pattern is present in both prophase samples, indicating that the chromosomes are aligning along their lengths (Figure 3.2B). The telomeric regions in the zygotene sample show high contact frequency with other telomeric regions, representing the clustering of telomeres at the nuclear envelope in the chromosomal bouquet configuration (Figure 3.2C). The pachytene sample shows a significant decrease in telomere clustering, as well as nearly a two-fold drop in inter-chromosomal interactions (17.2% of reads show trans interactions in zygotene samples, compared to 10.4% trans interactions in pachytene) (Table S3.3), agreeing with cytological data showing the bouquet is disassembled in pachytene (Harper, 2004). Taken together, these data suggest we can use Hi-C to visualize unique chromatin structures like the bouquet, and detect the dynamic reorganization of meiotic chromosomes as they progress through prophase.

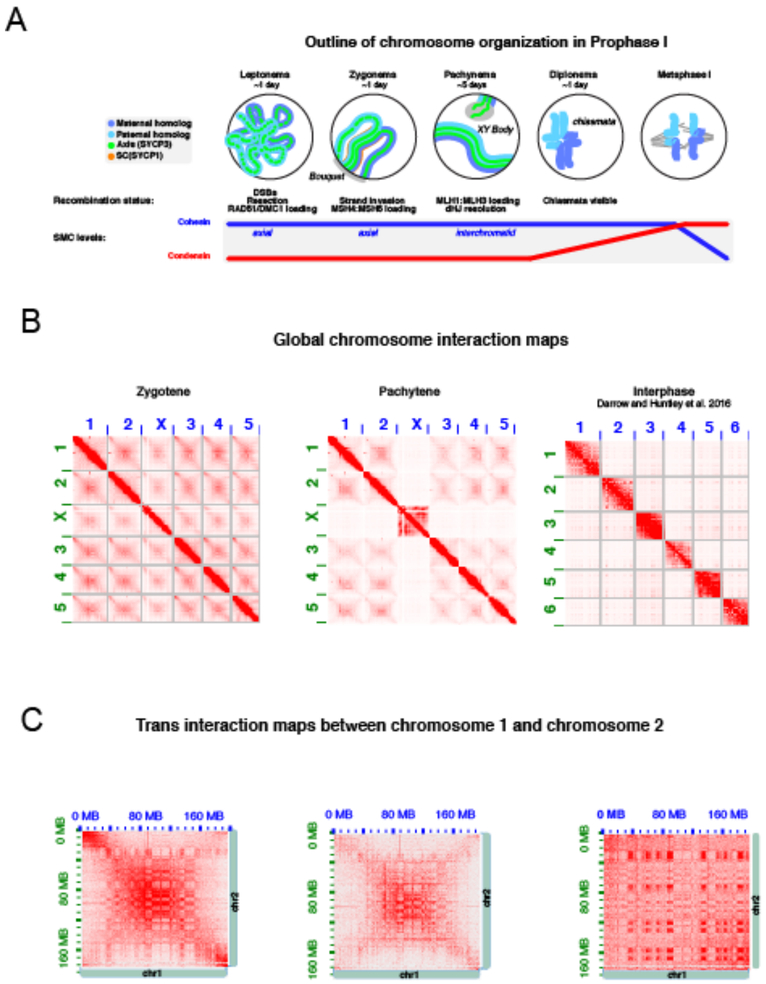

**Figure 3.2 Hi-C contact maps reveal hallmark structural features of meiosis**

(A) Schematic showing progression of meiotic prophase through four sub-stages. (B) Global contact maps of zygotene and pachytene stage samples, with interphase sample (Darrow and Huntley et al. 2016) present for comparison. (C) Inter-chromosomal or trans-interaction map of chromosome 1 and 2.

### 3.3.3 XY body formation

A defining feature in the transition between zygotene and pachytene is the formation of the XY body or sex body (Solari, 1974). Unlike the autosomes, the X and Y chromosomes only undergo pairing in a small homologous region, called the pseudoautosomal region (PAR) (Perry et al., 2001). The X and Y chromosomes become segregated away from the other chromosomes into a condensed structure at the end of zygotene, and by mid-pachytene have formed a discrete microscopically-visible structure at the nuclear periphery (Solari, 1974). XY body formation results in sex chromosomes become transcriptionally silenced by unique histone modifications and heterochromatin-specific proteins through a process called meiotic sex-chromosome inactivation (MSCI) (Burgoyne et al., 2009; Handel, 2004; Turner et al., 2005).

X-chromosome contact maps show strong evidence of isolation and compaction of the sex chromosomes in the zygotene-pachytene transition. X chromosome trans-interactions decrease from 36.9% in zygotene to 12.3% in pachytene (Figure 3.2B). The pachytene contact maps for the X chromosome also show a dramatic increase in very long-range cis interactions, supporting the idea that unlike the other autosomes, the sex chromosomes are not constrained to a linear loop array configuration, and have become highly compacted and isolated. Another interesting feature is the loss of TAD structures from the X chromosome in pachytene (Figure 3.3B), reminiscent of inactivated X-chromosomes from interphase cells (Giorgetti et al., 2016). This could be explained by the cohesin and CTCF-based machinery responsible for generating loop structures being removed during sex body formation.

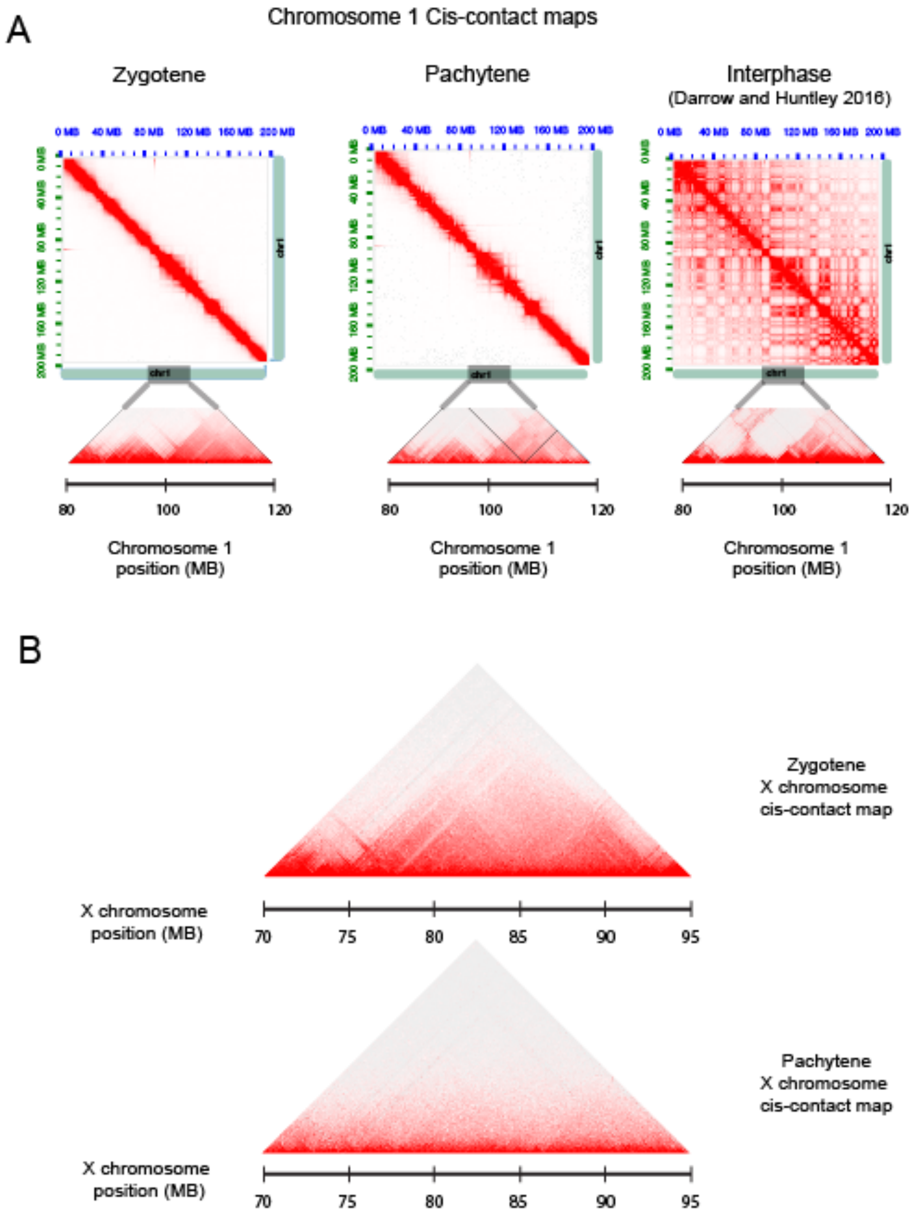

**Figure 3.3 TAD/domain architecture in meiotic chromosomes**

(A) Chromosome 1 intra-chromosomal or cis-interaction maps. TADs can be seen along the diagonal, mirroring the architecture seen in interphase chromosomes, although long-range interactions are lost. (B) TAD structure of the X chromosome in zygotene and pachytene. TADs disappear in the transition from zygotene to pachytene, likely as a result of sex body formation

### 3.3.4 Meiotic prophase chromosomes contain interphase-like structures with a loss of long-range interactions

A striking feature of the meiotic Hi-C contact maps is the presence of TAD or domain-like structures present along the diagonal in our cis-interaction maps (Figure 3.3A). The location of these domains and their boundaries closely mirrors what is seen in interphase cells (Darrow et al., 2016) (Dixon et al., 2012), supporting the idea that these boundaries are retained in meiotic prophase. While the local architecture of the meiotic chromosomes appears to closely resemble their interphase counterparts, long-range cis-interactions (>2 MB) are dramatically reduced (Figure 3.3A), consistent with the idea that meiotic chromosomes become linearly arranged around the chromosome axis. Interestingly, the A/B compartment signal is retained, and can be clearly observed in trans-interaction maps (Figure 3.2C). This indicates that while the chromosomes become linearly arranged along the chromosome axis in meiotic prophase, the architectural constraints giving rise to the compartment signal are retained. Since we know cohesin complexes are maintained throughout early-mid prophase on meiotic chromosomes, the presence of TADs and compartments in zygotene and pachytene-stage spermatocytes may not be surprising. The complete loss of long range interactions is also easily explained by the presence of the chromosome axis, which would be expected to prevent the higher-order folding of chromosomes necessary to generate these interactions. How TAD structures are compatible with the linear loop array organization imposed by the chromosome axis remains an important question.

## 3.4 Discussion

Assembly of a linear loop array by the chromosome axis is a critical aspect of meiotic prophase, as it is thought to be required for accurate pairing and segregation of homologs. The molecular basis of genome organization by the chromosome axis and the underlying architecture of chromosomes remain major questions. Analysis of meiotic genome organization on the DNA and protein level has thus far been widely limited to the resolution of fluorescence light microscopy and electron microscopy. Here we present preliminary Hi-C analysis on highly synchronized meiotic zygotene and pachytene stage cells, demonstrating the ability to outline the local and global architecture of meiotic chromosomes.

We observe unique structural features of meiotic chromosomes when comparing our zygotene and pachytene stage samples. The zygotene samples demonstrate telomere clustering and the chromosomal bouquet arrangement, visualized as X-shaped patterns with increased interaction frequencies at the telomeric regions in our inter-chromosomal contact maps. In agreement with previous data showing the chromosomal bouquet is disassembled by pachytene (Harper, 2004), we see almost a two-fold decrease in inter-chromosomal interactions in pachytene compared to zygotene, and telomere clustering almost disappear. We also observe significant isolation and compaction of the X chromosome between zygotene and pachytene, indicative of XY/sex body formation. The ability to visualize these hallmark features of meiosis, and their dynamic rearrangements strongly supports the use of next generation sequencing techniques in the examination of meiotic genome organization.

The observation that interphase TAD structures are highly conserved in meiotic prophase cells is an interesting, but not surprising finding. This implies organization of the DNA into a linear array of loops by the chromosome axis is still compatible with underlying interphase chromosome architecture (model figure). If cohesin and loop extruding machinery coordinated by CTCF boundary sites are all that is necessary for the generation of TADs, then we might expect these structures to be present until late prophase, when condensins replace cohesin and further compact the chromosomes before metaphase. One important thing to note is that TADs do not exist in individual cells. The TAD signal arises in Hi-C datasets from large populations of cells, which each contain different, but systematically regulated loop structures. Thus, it is possible that the TAD signal in our dataset arises similarly, from each cell's chromosomes being constrained as a linear loop array, but with loop locations differing stochastically between cells (Figure 3.4). The ability to visualize TADs indicates Hi-C is capable of observing chromosome architecture at the global and local levels. An important next step in this analysis will be investigating the DNA loop structures present in meiosis, and determining the sequencing depth necessary to observe these structures.

Moving forward with this project, our first priority is to establish a reliable allele-specific mapping step in our Hi-C pipeline. Recently, mapping software called WASP was introduced, demonstrating the ability to significantly reduce mapping bias and the generation of false positives (van de Geijn et al., 2015). Another downside of the HiC-Pro pipeline is its lack of compatibility with other software that can generate TAD calls and genome-wide plots of contact probability versus sequence distance. The next step in advancing our analysis of meiotic chromosome structure will be to implement the WASP allele-specific read aligner in conjunction with a more versatile Hi-C pipeline. Another important missing element is a control cell line. For this, we will analyze purified pre-meiotic cells from spermatogonia of wild-type C57Bl/6 mice, which will reveal the

TAD/compartment structure in cells that are developmentally just prior to the cells in our meiotic samples.

It will also be important to outline the roles of the chromosome axis protein machinery involved in regulating meiotic prophase genome organization. Cohesins are well established as the underlying element of the chromosome axis, and are essential for formation of loops and TADs (Winters et al., 2014) (Schwarzer et al., 2017) (Rao et al., 2017). The lateral element proteins SYCP2 and SYCP3 have also been shown to play essential structural roles in organizing meiotic chromosomes and regulating homologous recombination (Yuan, 2002; Yuan et al., 2000). Mutations to SYCP3 have been shown to negatively affect chromosome compaction and the size of DNA loops (Kolas et al., 2004) (Novak et al., 2008). We can use Hi-C analysis to look at how the architecture of meiotic chromosomes is altered in cohesin and SYCP2/SYCP3 mutant mice, which will provide further insight into the roles of the chromosome axis in meiotic prophase genome organization.

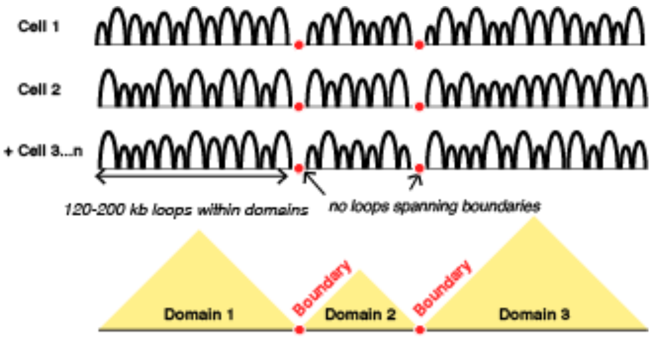

**Figure 3.4 Model for chromatin organization in meiosis**

Model demonstrating how a linear array of loops could give rise to TADs in meiotic prophase chromosomes. Although different cells will contain slightly different loops, the boundary elements will always give rise to the same TAD structures.

## 3.5 Experimental Procedures

### 3.5.1 Hi-C Library Preparation

#### Cell crosslinking

B6 x CAST F1 hybrid mouse spermatocytes synchronized in pachytene or zygotene stage of prophase were crosslinked by adding 1% Formaldehyde and incubating for 10 minutes at Room temperature. The reaction was stopped by adding 150 mM glycine. The cell suspension was incubated for 5 mintues at room temperature, followed by 15 minutes on ice. The crosslinked suspension was pelleted at 1500 rpm for 10 minutes, the supernatant discarded, and the cell ppellets frozen at -80C.

#### Cell lysis and restriction enzyme digestion

300 uL Lysis buffer (10 mM Tris-HCl pH8.0, 10 mM NaCl, 0.2% Igepal CA630 (Sigma), 50 uL Protease Inhibitor (Sigma, P8340)) was added to crosslinked pellets, and pellets were resuspended. Pellets were incubated on ice for 15-30 minutes and mixed by inversion. Suspension was centrifuged at 2500G for 5 minutes at 4C, and supernatant was discarded. Pelleted nuclei washed by adding 500 uL of cold lysis buffer and spund down at 2500G for 5 min at 4C. Pellet was resuspended in 0.5% SDS and incubated for 5-10 minutes at 62C. After heating, 145 uL of H20 and 25uL of 10% TritonX-100 were added, and incubated at 37C for 15 min. 25 uL of 10X NEB2 an 100U of MboI were added to digest chromatin for 2 hours or O/N at 37C at 700 rpm rotation.

#### Biotinylation, ligation, crosslink reversal

Digestion completeness was checked by agarose gel. Mbo1 was inactivated by incubating sample at 62C for 20 minutes, then cooled to RT for 10 min. 37.5 uL of 0.4 nM Biotin dATP (Life Tech, 19524-016) and 1.5 uL of 10 mM (dCTP, dTTP, dGTP), and 8 uL of 5U/uL Klenow (NEB, MO210) was added to the sample (total volume 337.5 uL) and incubated for 90 min at 37C with 500 rpm rotation. Samples were ligated by adding 663 uL H20, 120 uL 10X T4 DNA ligase buffer (NEB, B0202) 100 uL of 10% Triton X-100, 12 uL of 10mg/mL BSA, and 5 uL of 400U/uL T4 DNA Ligase (NEB, M0202). Samples were mixed by inversion and incubated at RT for 4 hr with 300 rpm rotation. Crosslinks were reversed by adding 50 uL 20 mg/mL Proteinase K (NEB P8102) and 120 uL of 10% SDS, and incubated at 55C for 30 min. 130 uL of 5M NaCl was added and incubated for 90 min at 65C.

**DNA purification, sonication, size selection**

DNA was precipitated using 1.6X volume of 100% ethanol and 0.1X volume of 3M Sodium Acetate pH 5.2. Pellet was spun down and washed with 70% ethanol twice, and resuspended with 100uL of 1x Tris Buffer (10 mM Tris-HCl pH8.0) and incubated for 15 min at 37C. DNA was sonicated in covaris tubes and sonicator at (Duty Cycle:10, Intensity: 4, Cycles/Burst:200, Duration: 55 seconds, Cycles: 1). DNA was size selected using SPRI beads. 115 uL of beads was added and incubated for 5 min at RT. Beads were collected on magnet and the solution was transferred to a fresh tube (fragments >500 bp will remain bead-bound). Do a second SPRI size selection using 85 uL of AMPure beads. The beads were saved and washed twice with 700 uL of 70% ethanol and eluted in 300 uL of 1x Tris buffer. The size selected should range between 200-600 bp.

**Biotin pulldown and library prep**

100 uL of 10mg/mL Dynabeads My One T1 Streptavidin beads (T1 beads) were washed by 1x Tween Wash Buffer (5 mM Tris-HCl pH 7.5, 0.5 mM EDTA, 1M NaCl, 0.05% Tween). The beads were resuspended in 300 uL of 2X BB (10 mM Tris-HCl pH7.5, 1mM EDTA, 2M NaCl). Beads were transferred to the sample tube and incubated for 15 min at RT. Supernatant was separated on a magnet and discarded, and the beads were washed with 1X wash buffer and heated for 2 min at 55C mixing at 350 rpm. Beads were bound to magnet and supernatant removed, and wash was repeated. Beads were resuspended in 100uL 1X NEB T4 DNA ligase buffer (NEB, B0202). Buffer was removed on the magnet and beads were resuspended in (88 uL 1x NEB T4 DNA ligase buffer, 2 uL of 25 mM dNTP mix, 5 uL of 10U/uL NEB T4 PNK (NEB, M0201), and 4 uL of 3U/uL NEB T4 DNA polymerase (NEB, M0203) 1uL of 5U/uL Klenow (NEB, M0210)). Suspensions were incubated for 30 min at 37C, separated on a magnet and the supernatant discarded. Beads were washed in 100 uL 1X NEB Quick Ligation Reaction Buffer (NEB, B2200S), and resuspended in 50 uL of 1X NEB Quick Ligation Reaction Buffer. Adapters were ligated by adating 2 uL of NEB DNA quick Ligase (NEB, M2200) and 3 uL of Illumina Indexed adapter, and incubated for 15 min at RT. Reactions were washed and resuspended in 50 uL of 1X Tris buffer. qPCR was performed to estimate the cycle and concentration needed for the final amplification PCR step.

### 3.5.2 Hi-C mapping and contact map visualization

Hi-C libraries were sequenced using 100 base pair read paired-end sequencing on an Illumina HiSeq4000. The raw sequencing reads were processed using the HiC-

Pro pipeline. First, each end of the 100 bp reads were aligned separately to the Mouse mm10 reference genome using the bowtie2 end-to-end algorithm. HiC-Pro then assigns each aligned read to one Mbo1 restriction fragment according to the reference genome, generating a list of valid interaction pairs from different restriction fragments. Valid interaction lists were used to generate .hic files using the hic2pro2juicebox script provided by HiC-Pro, and used to visualize the contact maps generated by juicebox.

## 3.6 Supplemental Data

### Table S3.1 Cell preparations for Hi-C

| Sample | Days post-RA injection | Pre-sort purity (SYCP3-positive cells) | Post-sort purity | Total sorted cells |
|---|---|---|---|---|
| **Zygonema #1** | 25 | 33% zygonema / 67% diplonema | 94% zygo / 1% round spermatids / 5% DAPI[1] | 600,000 |
| **Zygonema #2** | 33 | 0.6% leptonema / 42% zygonema / 58% diplonema | 5% leptonema / 91% zygonema / 1% Diplonema, 3% DAPI | 743,750 |
| **Pachynema** | 30 | 99% pachynema / 1% diplonema | 77% pachynema / 23% Diplonema[2] / 1% round spermatids | 807, 250 |

[1] DAPI refers to DAPI-positive, SYCP-3 negative cells that are likely somatic cells from surrounding tissue.

[2] Cells were scored as diplonema if even a single chromosome pair showed evidence of desynapsis.

## Table S3.2 Bowtie2 Mapping

| | **Zygonema 1** | **Zygonema 2** | **Pachynema** |
|---|---|---|---|
| Total pairs processed | 328591151 | 357547423 | 280186679 |
| Unmapped pairs | 8786717 | 9972963 | 7976652 |
| Unique paired alignments | 198191105 | 221887603 | 176097175 |
| Multiple pairs alignments | 54129397 | 55918188 | 45459594 |
| Pairs with singleton | 67483932 | 69768669 | 50653258 |
| Report pairs | 198191105 | 221887603 | 176097175 |
| %Mappable | 60.3% | 62.1% | 62.8% |

## Table S3.3 Intrachromosomal vs. Interchromosomal read counts

| | **Zygonema combined** | **Pachynema** |
|---|---|---|
| Total mapped read pairs | 420078708 | 176097175 |
| Autosome intra (%) | 82.82705137 | 89.56500568 |
| Autosome inter (%) | 17.17294863 | 10.43499432 |
| X intra (%) | 63.04327035 | 87.70807561 |
| X inter (%) | 36.95672965 | 12.29192439 |

## 3.7 References

Baudat, F., Imai, Y., de Massy, B., 2013. Meiotic recombination in mammals: localization and regulation. Nat Rev Genet 14, 794–806. doi:10.1038/nrg3573

Burgoyne, P.S., Mahadevaiah, S.K., Turner, J.M.A., 2009. The consequences of asynapsis for mammalian meiosis. Nat Rev Genet 10, 207–216. doi:10.1038/nrg2505

Carvalho, C., Pereira, H.M., Ferreira, J., Pina, C., Mendonca, D., Rosa, A.C., Carmo-Fonseca, M., 2001. Chromosomal G-dark Bands Determine the Spatial Organization of Centromeric Heterochromatin in the Nucleus. Mol. Biol. Cell 12, 3563–3572. doi:10.1091/mbc.12.11.3563

Cole, F., Baudat, F., Grey, C., Keeney, S., de Massy, B., Jasin, M., 2014. Mouse tetrad analysis provides insights into recombination mechanisms and hotspot evolutionary dynamics. Nat Genet 46, 1072–1080. doi:10.1038/ng.3068

Cremer, M., Grasser, F., Lanctôt, C., Müller, S., Neusser, M., Zinner, R., Solovei, I., Cremer, T., 2008. Multicolor 3D Fluorescence In Situ Hybridization for Imaging Interphase Chromosomes, in: The Nucleus, Methods in Molecular Biology. Humana Press, Totowa, NJ, pp. 205–239. doi:10.1007/978-1-59745-406-3_15

Cutter, A.R., Hayes, J.J., 2015. A brief review of nucleosome structure. FEBS Lett. 589, 2914–2922. doi:10.1016/j.febslet.2015.05.016

Darrow, E.M., Huntley, M.H., Dudchenko, O., Stamenova, E.K., Durand, N.C., Sun, Z., Huang, S.-C., Sanborn, A.L., Machol, I., Shamim, M., Seberg, A.P., Lander, E.S., Chadwick, B.P., Aiden, E.L., 2016. Deletion of DXZ4on the human inactive X chromosome alters higher-order genome architecture. Proceedings of the National Academy of Sciences 113, E4504–E4512. doi:10.1073/pnas.1609643113

Dekker, J., 2002. Capturing Chromosome Conformation. Science 295, 1306–1311. doi:10.1126/science.1067799

Dixon, J.R., Selvaraj, S., Yue, F., Kim, A., Li, Y., Shen, Y., Hu, M., Liu, J.S., Ren, B., 2012. Topological domains in mammalian genomes identified by analysis of chromatin interactions. Nature 485, 376–380. doi:10.1038/nature11082

Eagen, K.P., Aiden, E.L., Kornberg, R.D., 2017. Polycomb-mediated chromatin loops revealed by a subkilobase-resolution chromatin interaction map. Proceedings of the National Academy of Sciences 114, 8764–8769. doi:10.1073/pnas.1701291114

Flyamer, I.M., Gassler, J., Imakaev, M., Brandão, H.B., Ulianov, S.V., Abdennur, N., Razin, S.V., Mirny, L.A., Tachibana-Konwalski, K., 2017. Single-nucleus Hi-C reveals unique chromatin reorganization at oocyte-to-zygote transition. Nature 544, 110–114. doi:10.1038/nature21711

Fudenberg, G., Imakaev, M., Lu, C., Goloborodko, A., Abdennur, N., Mirny, L.A., 2016. Formation of Chromosomal Domains by Loop Extrusion. Cell Reports 15, 2038–2049. doi:10.1016/j.celrep.2016.04.085

Giorgetti, L., Lajoie, B.R., Carter, A.C., Attia, M., Zhan, Y., Xu, J., Chen, C.-J., Kaplan, N., Chang, H.Y., Heard, E., Dekker, J., 2016. Structural organization of the inactive X chromosome in the mouse. Nature 535, 575–579. doi:10.1038/nature18589

Handel, M., 2004. The XY body: a specialized meiotic chromatin domain. Exp. Cell Res. 296, 57–63. doi:10.1016/j.yexcr.2004.03.008

Hansen, A.S., Pustova, I., Cattoglio, C., Tjian, R., Darzacq, X., 2017. CTCF and cohesin regulate chromatin loop stability with distinct dynamics. Elife 6, 2848. doi:10.7554/eLife.25776

Harper, L., 2004. A bouquet of chromosomes. J. Cell. Sci. 117, 4025–4032. doi:10.1242/jcs.01363

Hofmann, A., Heermann, D.W., 2015. The role of loops on the order of eukaryotes and prokaryotes. FEBS Lett. 589, 2958–2965. doi:10.1016/j.febslet.2015.04.021

Hogarth, C.A., Griswold, M.D., 2013. Retinoic acid regulation of male meiosis. Current Opinion in Endocrinology & Diabetes and Obesity 20, 217–223. doi:10.1097/MED.0b013e32836067cf

Keane, T.M., Goodstadt, L., Danecek, P., White, M.A., Wong, K., Yalcin, B., Heger, A., Agam, A., Slater, G., Goodson, M., Furlotte, N.A., Eskin, E., Nellåker, C., Whitley, H., Cleak, J., Janowitz, D., Hernandez-Pliego, P., Edwards, A., Belgard, T.G., Oliver, P.L., McIntyre, R.E., Bhomra, A., Nicod, J., Gan, X., Yuan, W., van der Weyden, L., Steward, C.A., Bala, S., Stalker, J., Mott, R., Durbin, R., Jackson, I.J., Czechanski, A., Guerra-Assunção, J.A., Donahue, L.R., Reinholdt, L.G., Payseur, B.A., Ponting, C.P., Birney, E., Flint, J., Adams, D.J., 2011. Mouse genomic variation and its effect on phenotypes and gene regulation. Nature 477, 289–294. doi:10.1038/nature10413

Kolas, N.K., Yuan, L., Höög, C., Heng, H.H.Q., Marcon, E., Moens, P.B., 2004. Male mouse meiotic chromosome cores deficient in structural proteins SYCP3 and SYCP2 align by homology but fail to synapse and have possible impaired specificity of chromatin loop attachment. Cytogenet Genome Res 105, 182–188. doi:10.1159/000078188

Koszul, R., Kim, K.P., Prentiss, M., Kleckner, N., Kameoka, S., 2008. Meiotic Chromosomes Move by Linkage to Dynamic Actin Cables with Transduction of Force through the Nuclear Envelope. Cell 133, 1188–1201. doi:10.1016/j.cell.2008.04.050

Koszul, R., Kleckner, N., 2009. Dynamic chromosome movements during meiosis: a way to eliminate unwanted connections? Trends Cell Biol. 19, 716–724. doi:10.1016/j.tcb.2009.09.007

Langmead, B., Salzberg, S.L., 2012. Fast gapped-read alignment with Bowtie 2. Nat Meth 9, 357–359. doi:10.1038/nmeth.1923

Lieberman-Aiden, E., van Berkum, N.L., Williams, L., Imakaev, M., Ragoczy, T., Telling, A., Amit, I., Lajoie, B.R., Sabo, P.J., Dorschner, M.O., Sandstrom, R., Bernstein, B., Bender, M.A., Groudine, M., Gnirke, A., Stamatoyannopoulos, J., Mirny, L.A., Lander, E.S., Dekker, J., 2009. Comprehensive mapping of long-range interactions reveals folding principles of the human genome. Science 326, 289–293. doi:10.1126/science.1181369

Losada, A., Yokochi, T., Kobayashi, R., Hirano, T., 2000. Identification and Characterization of Sa/Scc3p Subunits in the Xenopusand Human Cohesin Complexes. J. Cell Biol. 150, 405–416. doi:10.1083/jcb.150.3.405

Manuelidis, L., 1985. Individual interphase chromosome domains revealed by in situ hybridization. Hum. Genet. 71, 288–293.

Naumova, N., Imakaev, M., Fudenberg, G., Zhan, Y., Lajoie, B.R., Mirny, L.A., Dekker, J., 2013. Organization of the Mitotic Chromosome. Science 342, 948–953. doi:10.1126/science.1236083

Nora, E.P., Lajoie, B.R., Schulz, E.G., Giorgetti, L., Okamoto, I., Servant, N., Piolot, T., van Berkum, N.L., Meisig, J., Sedat, J., Gribnau, J., Barillot, E., Blüthgen, N., Dekker, J., Heard, E., 2012. Spatial partitioning of the regulatory landscape of the X-inactivation centre. Nature 485, 381–385. doi:10.1038/nature11049

Novak, I., Wang, H., Revenkova, E., Jessberger, R., Scherthan, H., Höög, C., 2008. Cohesin Smc1beta determines meiotic chromatin axis loop organization. J. Cell Biol. 180, 83–90. doi:10.1083/jcb.200706136

Padmore, R., Cao, L., Kleckner, N., 1991. Temporal comparison of recombination and synaptonemal complex formation during meiosis in S. cerevisiae. Cell 66, 1239–1256. doi:10.1016/0092-8674(91)90046-2

Page, S.L., Hawley, R.S., 2004. THE GENETICS AND MOLECULAR BIOLOGY OF THE SYNAPTONEMAL COMPLEX. Annu. Rev. Cell Dev. Biol. 20, 525–558. doi:10.1146/annurev.cellbio.19.111301.155141

Perry, J., Palmer, S., Gabriel, A., Ashworth, A., 2001. A short pseudoautosomal region in laboratory mice. Genome Research 11, 1826–1832. doi:10.1101/gr.203001

Phanstiel, D.H., Van Bortle, K., Spacek, D., Hess, G.T., Shamim, M.S., Machol, I., Love, M.I., Aiden, E.L., Bassik, M.C., Snyder, M.P., 2017. Static and Dynamic DNA Loops form AP-1-Bound Activation Hubs during Macrophage Development. Mol. Cell 67, 1037–1048.e6. doi:10.1016/j.molcel.2017.08.006

Quinlan, A.R., Clark, R.A., Sokolova, S., Leibowitz, M.L., Zhang, Y., Hurles, M.E., Mell, J.C., Hall, I.M., 2010. Genome-wide mapping and assembly of structural variant breakpoints in the mouse genome. Genome Research 20, 623–635. doi:10.1101/gr.102970.109

Quinodoz, S.A., Ollikainen, N., Tabak, B., Palla, A., Schmidt, J.M., Detmar, E., Lai, M., Shishkin, A., Bhat, P., Trinh, V., Aznauryan, E., Russell, P., Cheng, C., Jovanovic, M., Chow, A., McDonel, P., Garber, M., Guttman, M., 2017. Higher-order inter-chromosomal hubs shape 3-dimensional genome organization in the nucleus. bioRxiv 219683. doi:10.1101/219683

Rao, S.S.P., Huang, S.-C., Glenn St Hilaire, B., Engreitz, J.M., Perez, E.M., Kieffer-Kwon, K.-R., Sanborn, A.L., Johnstone, S.E., Bascom, G.D., Bochkov, I.D., Huang, X., Shamim, M.S., Shin, J., Turner, D., Ye, Z., Omer, A.D., Robinson, J.T., Schlick, T., Bernstein, B.E., Casellas, R., Lander, E.S., Aiden, E.L., 2017. Cohesin Loss Eliminates All Loop Domains. Cell 171, 305–320.e24. doi:10.1016/j.cell.2017.09.026.

Rao, S.S.P., Huntley, M.H., Durand, N.C., Stamenova, E.K., Bochkov, I.D., Robinson, J.T., Sanborn, A.L., Machol, I., Omer, A.D., Lander, E.S., Aiden, E.L., 2014. A 3D Map of the Human Genome at Kilobase Resolution Reveals Principles of Chromatin Looping. Cell 159, 1665–1680. doi:10.1016/j.cell.2014.11.021

Schardin, M., Cremer, T., Hager, H.D., Lang, M., 1985. Specific staining of human chromosomes in Chinese. Hum. Genet. 71, 281–287.

Schwarzer, W., Abdennur, N., Goloborodko, A., Pekowska, A., Fudenberg, G., Loe-Mie, Y., Fonseca, N.A., Huber, W., H Haering, C., Mirny, L., Spitz, F., 2017. Two independent modes of chromatin organization revealed by cohesin removal. Nature 551, 51–56. doi:doi:10.1038/nature24281

Servant, N., Varoquaux, N., Lajoie, B.R., Viara, E., Chen, C.-J., Vert, J.-P., Heard, E., Dekker, J., Barillot, E., 2015. HiC-Pro: an optimized and flexible pipeline for Hi-C data processing. Genome Biol. 16, 11. doi:10.1186/s13059-015-0831-x

Shibuya, H., Morimoto, A., Watanabe, Y., 2014. The Dissection of Meiotic Chromosome Movement in Mice Using an In Vivo Electroporation Technique. PLoS Genet. 10, e1004821. doi:10.1371/journal.pgen.1004821

Solari, A.J., 1974. The Behavior of the XY Pair in Mammals, in: International Review of Cytology Volume 38, International Review of Cytology. Elsevier, pp. 273–317. doi:10.1016/S0074-7696(08)60928-6

Starr, D.A., 2009. A nuclear-envelope bridge positions nuclei and moves chromosomes. J. Cell. Sci. 122, 577–586. doi:10.1242/jcs.037622

Starr, D.A., Fischer, J.A., 2005. KASH 'n Karry: The KASH domain family of cargospecific cytoskeletal adaptor proteins. Bioessays 27, 1136–1146. doi:10.1002/bies.20312

Stevens, T.J., Lando, D., Basu, S., Atkinson, L.P., Cao, Y., Lee, S.F., Leeb, M., Wohlfahrt, K.J., Boucher, W., O'Shaughnessy-Kirwan, A., Cramard, J., Faure, A.J., Ralser, M., Blanco, E., Morey, L., Sansó, M., Palayret, M.G.S., Lehner, B., Di Croce, L., Wutz, A., Hendrich, B., Klenerman, D., Laue, E.D., 2017. 3D structures of individual mammalian genomes studied by single-cell Hi-C. Nature 544, 59–64. doi:10.1038/nature21429

Sumara, I., Vorlaufer, E., Gieffers, C., Peters, B.H., Peters, J.M., 2000. Characterization of vertebrate cohesin complexes and their regulation in prophase. J. Cell Biol. 151, 749–762.

Terakawa, T., Bisht, S., Eeftens, J.M., Dekker, C., Haering, C.H., Greene, E.C., 2017. The condensin complex is a mechanochemical motor that translocates along DNA. Science 358, 672–676. doi:10.1126/science.aan6516

Turner, J.M.A., Mahadevaiah, S.K., Fernandez-Capetillo, O., Nussenzweig, A., Xu, X., Deng, C.-X., Burgoyne, P.S., 2005. Silencing of unsynapsed meiotic chromosomes in the mouse. Nat Genet 37, 41–47. doi:10.1038/ng1484

Tzur, Y.B., Wilson, K.L., Gruenbaum, Y., 2006. SUN-domain proteins: “Velcro” that links the nucleoskeleton to the cytoskeleton. Nat. Rev. Mol. Cell Biol. 7, 782–788. doi:10.1038/nrm2003

van Berkum, N.L., Lieberman-Aiden, E., Williams, L., Imakaev, M., Gnirke, A., Mirny, L.A., Dekker, J., Lander, E.S., 2010. Hi-C: a method to study the three-dimensional architecture of genomes. J Vis Exp e1869–e1869. doi:10.3791/1869

van de Geijn, B., McVicker, G., Gilad, Y., Pritchard, J.K., 2015. WASP: allele-specific software for robust molecular quantitative trait locus discovery. Nat Meth 12, 1061–1063. doi:10.1038/nmeth.3582

Varoquaux, N., Ay, F., Noble, W.S., Vert, J.P., 2014. A statistical approach for inferring the 3D structure of the genome. Bioinformatics 30, i26–i33. doi:10.1093/bioinformatics/btu268

Waizenegger, I.C., Hauf, S., Meinke, A., Peters, J.M., 2000. Two distinct pathways remove mammalian cohesin from chromosome arms in prophase and from centromeres in anaphase. Cell 103, 399–410.

Wanat, J.J., Kim, K.P., Koszul, R., Zanders, S., Weiner, B., Kleckner, N., Alani, E., 2008. Csm4, in Collaboration with Ndj1, Mediates Telomere-Led Chromosome Dynamics and Recombination during Yeast Meiosis. PLoS Genet. 4, e1000188. doi:10.1371/journal.pgen.1000188

Winters, T., McNicoll, F., Jessberger, R., 2014. Meiotic cohesin STAG3 is required for chromosome axis formation and sister chromatid cohesion. EMBO J. 33, 1256–1270. doi:10.1002/embj.201387330

Yuan, L., 2002. Female Germ Cell Aneuploidy and Embryo Death in Mice Lacking the Meiosis-Specific Protein SCP3. Science 296, 1115–1118. doi:10.1126/science.1070594

Yuan, L., Liu, J.-G., Zhao, J., Brundell, E., Daneholt, B., Höög, C., 2000. The Murine SCP3 Gene Is Required for Synaptonemal Complex Assembly, Chromosome Synapsis, and Male Fertility. Mol. Cell 5, 73–83. doi:10.1016/S1097-2765(00)80404-9

Zickler, D., Kleckner, N., 1998. The leptotene-zygotene transition of meiosis
. Annu. Rev. Genet. 32, 619–697. doi:10.1146/annurev.genet.32.1.619

# Chapter 4: Discussion

## 4.1 Conclusions and future directions

The studies presented in this dissertation outline conserved mechanisms underlying the assembly and organization of meiotic chromosomes at the protein and DNA level. These findings further our understanding of the architecture and function of the chromosome axis, and highlight the potential for next generation sequencing techniques in examining meiotic genome organization in future studies.

In Chapter 1 we present in vitro and in vivo studies outlining the organization and function of the meiotic HORMA domain proteins in *C. elegans*. We find that the four proteins HIM-3, HTP-1, HTP-2, and HTP-3 assemble into a hierarchical complex at chromosomes, and play distinct roles in regulating events during meiotic prophase. HTP-3 is capable of recruiting HIM-3, HTP-1, and HTP-2 through 6 “closure-motifs” present in its C-terminus, and is also involved in the loading of meiosis-specific cohesin complexes and DSB formation. We find that recruitment of HIM-3 to chromosomes occurs through four motifs present in the HTP-3 disordered tail, and that this recruitment mechanism is essential for synapsis and successful meiosis. Finally, we demonstrate HTP-1 and HTP-2 can be recruited by closure motifs in both HTP-3 or HIM-3, and that either of these mechanisms is dispensable for synapsis and embryonic viability. Since there is no identifiable homolog of the axis foundation component Red1/SYCP2/PAIR3 in *C. elegans*, addressing how HTP-3 is recruited to chromosomes remains an important question. Given the proposed role for HTP-3 in cohesin loading, cohesin complexes containing the meiosis-specific subunits REC-8, COH-3, and COH-4 make appealing targets to test for direct binding to HTP-3. Outlining the regulatory roles of HIM-3, HTP-1, and HTP-2 in synapsis and recombination will also be important in understanding chromosome axis function.

Chapter 2 outlines a structural and biochemical characterization of the mammalian chromosome axis proteins SYCP2 and SYCP3. We find that the coiled-coil domains of SYCP2 and SYCP3 physically associate to form high-molecular weight filaments. We demonstrate that these filaments are assembled through end-to-end oligomerization of a 2:2 tetrameric complex formed by SYCP2:SYCP3. This assembly mechanism provides an explanation for how SYCP2 and SYCP3 act as the structural foundation of the chromosome axis, compacting chromosomes and generating a continuous axial element between sister chromosomes. We also identify a 20-residue motif in SYCP2 that acts as a HORMAD-binding closure motif, revealing strong structural and functional parallels between SYCP2 and the fungal Red1 protein. How SYCP2 and SYCP3 localize to chromosomes remains an important question. SYCP2 has been shown to localize to chromosomes independently of SYCP3 and its own C-terminal coiled-coil domain, suggesting a role for its N-terminal domain in chromosome localization. Cohesin complex subunits make attractive candidates to test for direct binding to the SYCP2 N-terminal domain based on their colocalization and interdependence with SYCP2 and SYCP3 for axis assembly.

The results from Chapter 3 provide a preliminary examination of meiotic genome organization using a genomics based approach. Our Hi-C analysis identifies the presence of TADs/domains in the local architecture of meiotic prophase chromosomes. We are also able to visualize hallmark structural features of zygotene and pachytene stage chromosomes, such as the chromosomal bouquet and XY body. This analysis supports further examination of the meiotic nucleus using chromosome capture techniques. Using the high-resolution data obtained from Hi-C experiments could improve our limited understanding of exactly how DNA is organized as a linear loop array during the first meiotic prophase. Looking at how the chromatin architecture changes in different mutants of chromosome axis components is also an interesting approach in outlining the organizational and structural roles of the different axis components.

Although the chromosome axis is established as being essential to chromosome segregation and cell division during meiosis, its roles in genome organization and the regulation of homologous recombination remain mysterious. Outlining the architecture and organization of the core axis components will be an important first step in understanding how the AE recruits and regulates the vast amount of protein machinery during the first meiotic prophase.